

## TABLE OF CONTENTS

<b>I</b>	<b>Introduction and Motivation</b>	<b>6</b>
<b>1</b>	<b>Introduction</b>	<b>7</b>
1.1	The Basics of Nuclear Fusion and Tritium Breeding	8
1.2	Pebble Bed Solid Breeder Blanket Concepts	11
<b>2</b>	<b>Motivation</b>	<b>15</b>
2.1	Pebble Bed Integrity, Thermophysics, and the Role of Modeling	15
2.2	Scope of the Work	16
<b>3</b>	<b>Dissertation Outline</b>	<b>24</b>
<b>II</b>	<b>Literature Review</b>	<b>25</b>
<b>4</b>	<b>Status of Ceramic Breeder Modeling and Analysis</b>	<b>26</b>
4.1	DEM for Tritium Breeders	29
4.2	Experimental Pebble Bed thermo-mechanics Studies	34
4.2.1	Out-of-pile experiments	34
4.2.2	Pebble Bed Assemblies Experiment	38
4.2.3	More thermo-mechanics Characterization Experiments	40
4.3	Pebble Bed Thermo-mechanics Summary & Framework	42
<b>5</b>	<b>Hertzian Contact</b>	<b>44</b>
<b>6</b>	<b>Momentum and Energy Transfer in Packed Beds</b>	<b>50</b>

6.1	Pressure Drop Across Packed Beds . . . . .	50
6.1.1	Kozeny-Carman Correlation for Pressure Drop . . . . .	50
6.1.2	Ergun Correlation for Pressure Drop . . . . .	52
6.1.3	Koch-Hill-Lad Correlation for Pressure Drop . . . . .	53
6.1.4	Correlation Comparisons . . . . .	54
6.2	Heat TranSpot in Packed Beds . . . . .	56
6.2.1	Inter-particle Heat Conduction . . . . .	57
6.2.2	Nusselt Number for Spheres in Packed Beds . . . . .	60
6.2.3	Radiative Transfer with Neighboring Particles . . . . .	62
<b>III</b>	<b>Development of Modeling Tools for Pebble Bed Morphological Evolution Study</b>	<b>63</b>
<b>7</b>	<b>Development of DEM Modeling Tools for Ceramic Solid Breeders . . . . .</b>	<b>64</b>
7.1	Background . . . . .	64
7.2	Particle Dynamics . . . . .	65
7.2.1	Particle Kinematics . . . . .	65
7.2.2	Linear Spring-Dashpot Model . . . . .	66
7.2.3	Hertzian Non-Linear Spring Dashpot Model . . . . .	68
7.2.4	Time Integration . . . . .	69
7.3	Granular Heat Transfer . . . . .	70
7.3.1	Thermal Expansion . . . . .	71
7.4	DEM solver . . . . .	72
7.4.1	Numerical Implementation Overview . . . . .	72

<b>8 Development of CFD-DEM Modeling Tools for Ceramic Solid Breeders</b>	<b>74</b>
8.1 Numerical Methodology . . . . .	74
8.1.1 DEM . . . . .	75
8.1.2 Volume-averaged CFD Helium . . . . .	77
8.1.3 Modeling Setup and Procedure . . . . .	78
<b>9 Development of lattice-Boltzmann Modeling Tools for Ceramic Solid Breeders</b>	<b>80</b>
<b>10 Background Experimental Studies</b>	<b>81</b>
10.1 Elasticity Reduction Factor . . . . .	81
10.2 Translating Experimental Results to Pebble Bed Interactions . . . . .	90
10.2.1 Experimental Measurements of Strain Energy . . . . .	90
10.2.2 Calculating Critical Strain Energy . . . . .	92
<b>11 Background Numerical Studies</b>	<b>96</b>
11.1 Proper Selection of Young's Modulus for DEM Simulations . . . . .	96
11.1.1 Numerical Setup . . . . .	97
11.1.2 Results from Uni-axial Compression . . . . .	98
11.1.3 Conclusions for Modified Young's Modulus . . . . .	100
11.2 Jeffreson Correction to Lumped Capacitance Method . . . . .	101
11.2.1 Lumped Capacitance Solution for Sphere . . . . .	103
11.2.2 Exact Solution for Sphere . . . . .	105
11.2.3 Jeffreson Correction for Sphere . . . . .	109
11.3 Pebble Damage Modeling . . . . .	113
11.3.1 Modeling a Crushed Pebble . . . . .	115

11.4 Stability study . . . . .	122
11.4.1 Critical Dynamic Timestep . . . . .	123
11.4.2 Critical Thermal Timestep . . . . .	125
11.4.3 Simulation Acceleration with Scaled Material Properties . . . . .	126
<b>IV Studies of Pebble Bed Thermophysics, Mechanics, &amp; Morphological Changes</b>	<b>127</b>
<b>12 DEM Study on the Evolution of Effective Thermal Conductivity of a Pebble Bed Experiencing Pebble Crushing . . . . .</b>	<b>128</b>
12.1 DEM Study: Effective Conductivity with Pebble Damage . . . . .	128
12.1.1 Model Setup & Methodology . . . . .	129
12.1.2 Effective Thermal Conductivity from Analytic Analogy . . . . .	132
12.1.3 Results . . . . .	134
12.2 Conclusions . . . . .	142
<b>13 Coupled CFD-DEM Models Revealing the Influence of Helium Purge Gas on Effective Thermal Conductivity of a Pebble Bed Experiencing Pebble Crushing . . . . .</b>	<b>144</b>
13.1 Pressure Drop . . . . .	144
13.2 Effective Thermal Conductivity from CFD-DEM . . . . .	146
13.2.1 Stagnant interstitial fluid . . . . .	146
13.2.2 Purge Gas . . . . .	146
<b>14 3D Lattice-Boltzmann Models of the Complete Conjugate Heat Transfer of Helium Purge Gas and Ceramic Pebble Beds . . . . .</b>	<b>150</b>

<b>15 Applications to Real Solid Breeder Blanket Designs . . . . .</b>	<b>151</b>
--	------------

<b>V Future Work</b>	<b>153</b>
----------------------	------------

<b>VI Appendices</b>	<b>154</b>
----------------------	------------

<b>A Sphere with heat generation . . . . .</b>	<b>155</b>
--	------------

A.1 Transformations . . . . .	156
-------------------------------	-----

A.2 Solution . . . . .	157
------------------------	-----

A.3 Energy . . . . .	161
----------------------	-----

<b>B History of solid breeder design . . . . .</b>	<b>163</b>
--	------------

<b>References . . . . .</b>	<b>165</b>
-----------------------------	------------

**Part I**

# **Introduction and Motivation**

# CHAPTER 1

## Introduction

The controlled, sustained thermonuclear fusion of light elements is the ultimate energy source for humanity. Fusion is an energy source that is inexhaustible (on our planetary scales), produces none of the greenhouse gases that are altering the climate, and avoids many of the dangers of nuclear fission. But overcoming the engineering obstacles to tame the fusion reaction is the greatest technological challenge of our generation.

The solid breeder blanket is a pivotal piece of engineering technology upon which the success of a fusion power plant rests. From the inception of the solid breeder concept in 1975, designs have evolved significantly to meet the requirements of operation in the harsh fusion environment. The successful operation of a solid breeder will see the device capture ejected neutrons to generate tritium fuel, allow recovery of the bred tritium, act as shield to other sensitive equipment, and convert energy into extractable heat for electricity production.

The breeding blanket will experience high neutron flux and temperatures up to 900 °C, and continue operating despite the environment without being replaced or actively maintained. Its important that the solid breeder not simply survive the thermal and mechanical demands of the reactor environment but continue to release predictable and acceptable amounts of tritium. Increasingly reliable and accurate models are crucial in the design of operational solid breeder blanket technologies. In this dissertation, we advance the field of solid breeder modeling with the introduction of new techniques and tools.

In this chapter we will present more detail on the basics of thermonuclear fusion of hydrogen, the need to artificially breed tritium, and their relation to solid breeder blanket design. We then identify the overall design needs of a ceramic pebble bed functioning as

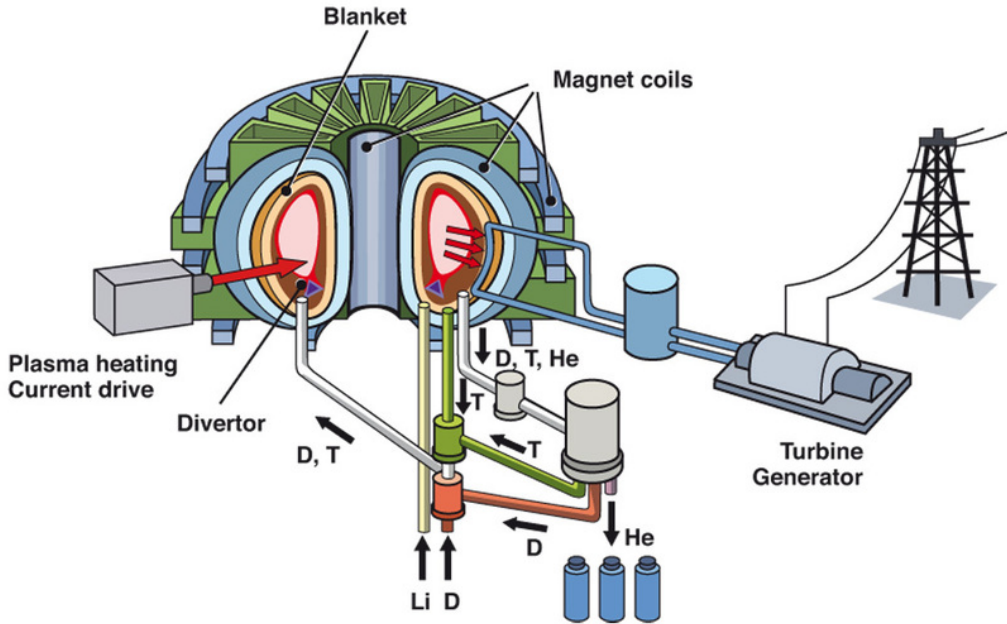


Figure 1.1: Schematic of a tokamak power plant showing the role of the blanket in both energy production and tritium breeding. (reproduced from the Max-Planck-Institut für Plasmaphysik)

solid breeder and, moreover, how the efforts of this dissertation fit into larger research efforts. The chapter concludes with laying out the objectives and scope of this dissertation.

## 1.1 The Basics of Nuclear Fusion and Tritium Breeding

In Fig. 1.1, we see the blanket surrounding the toroidally-shaped plasma and how the tritium generated in the blanket is recycled on-site to be fed back into the burning plasma. Also apparent in the sketch is the role of the breeding blanket as power generator.

The most favorable fusion reaction for first generation tokamak-style fusion reactors involves the two hydrogen isotopes of deuterium and tritium. The deuterium-tritium (DT) reaction has a high reaction probability at the lowest ion temperature and a high energy yield.

Alternative fusion reactions of two deuterium atoms or a deuterium atom with helium-3 are advantageous in other regards, such as no radioactive byproducts or fuel availability, but their relatively-higher ion temperature preclude them from current consideration.<sup>1</sup> The DT reaction proceeds as



Of the two isotopes fused, deuterium ( $D$ , or  ${}^2H$ ) is a stable isotope and is naturally occurring in an average abundance of 0.015 mole percent in water on Earth. To demonstrate just how plentiful deuterium is as a fuel source, there is approximately 100 million billion kilograms of deuterium in the Earth's oceans. If all energy on Earth were produced from DT fusion power plants, there would be enough deuterium to outlast the lifetime of our sun. We will not run out of deuterium.

Tritium ( $T$ , or  ${}^3H$ ), however, is radioactive with a half-life of only about 12.32 years; any naturally occurring tritium decays at such a rapid pace it will never accumulate to an appreciable amount on Earth. If tritium is to be used as a fuel in a fusion power plant, it must be generated artificially – thus the need for the so-called tritium breeding blankets. In-situ generation of tritium in a fusion reactor is possible with the assistance of lithium. Natural lithium will interact with neutrons as



where we have used the common short-hand of  $\alpha$  in place of the helium nucleus. The cross-sections of the lithium reactions are given in Fig. 1.2. Note the exothermic lithium-6 reaction (a neutron of any energy will incite the transmutation) and the threshold energy required of the incident neutron in the endothermic lithium-7 reaction.

Lithium, like deuterium, is quite abundant on Earth. To make the point clear, Francis Chen notes that there is enough lithium available on land to generate tritium for 30 million years of DT reactions providing all of humanity's electricity.<sup>18</sup> At the moment there are

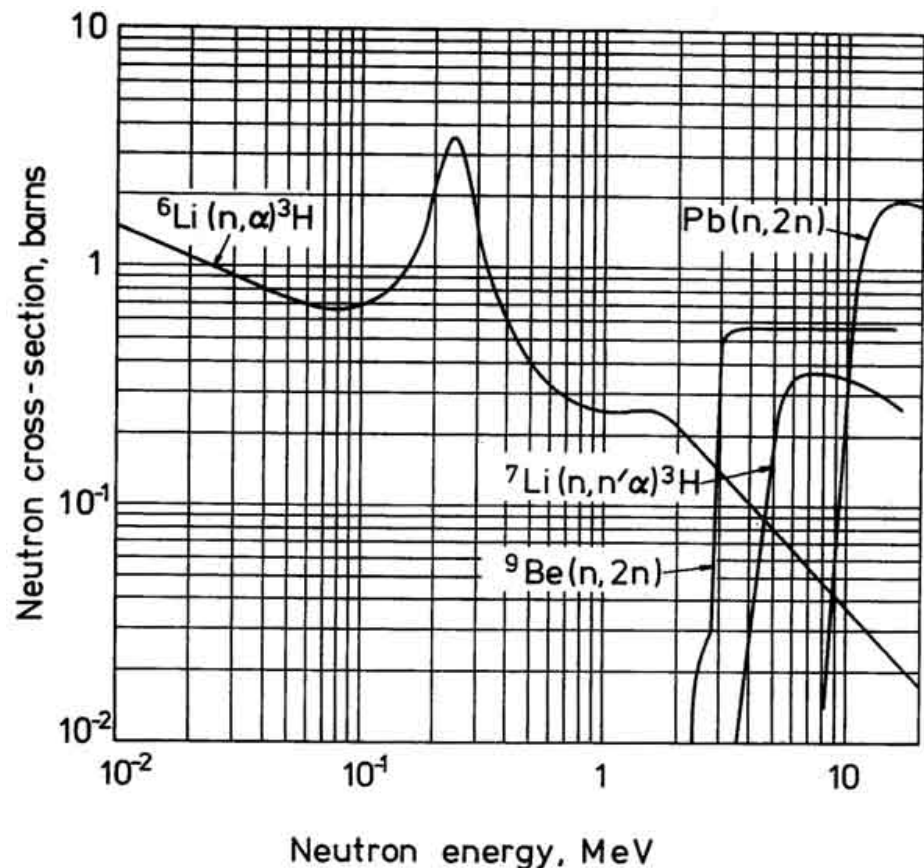


Figure 1.2: Cross-sections of various blanket materials. Note the threshold for the  ${}^7\text{Li}$  and neutron multiplying reactions.

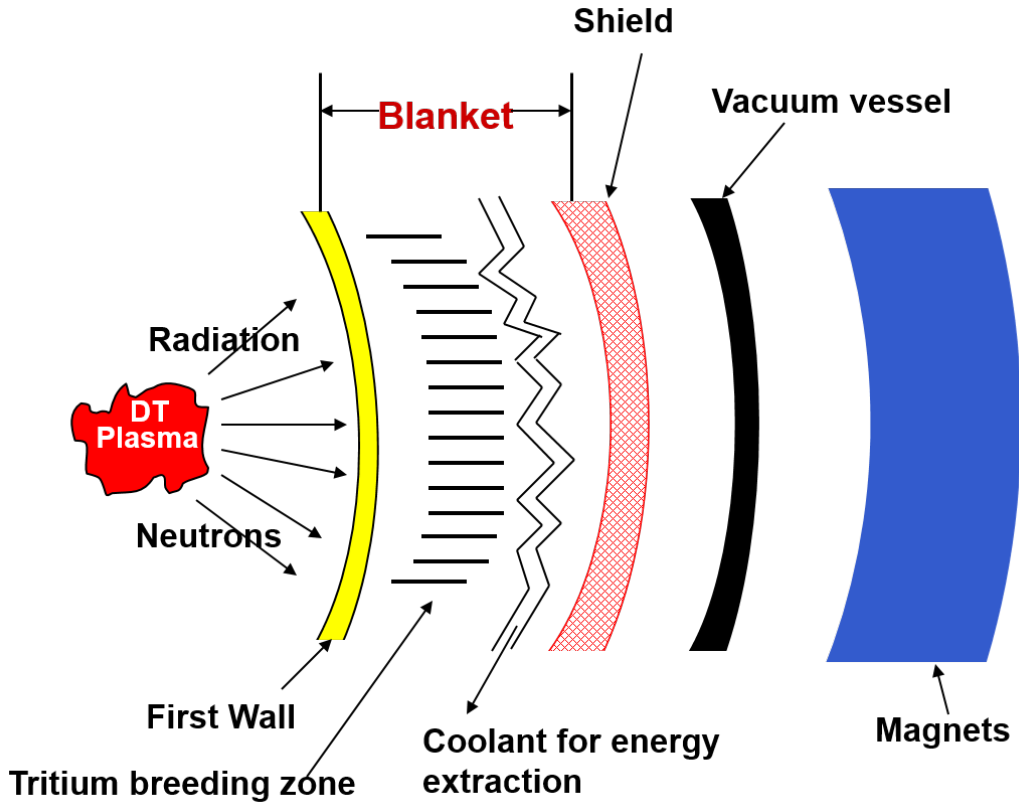


Figure 1.3: Among the reactor components, the blanket and first wall are responsible for heat production and tritium generation.

two main avenues of research for tritium breeder designs: liquid or solid lithium. While much research has been – and continues to be – performed on the liquid breeder design (for examples, see Refs. [cite many liquid breeder papers]), the work of this dissertation focuses solely on the ceramic pebble beds populating solid breeder designs. Sketched in Fig. 1.3 is the location of the breeding blanket and its relative location with other main components of a fusion reactor.

## 1.2 Pebble Bed Solid Breeder Blanket Concepts

Figure 1.4 is a sketch showing many of the important physical features of lithium ceramic pebble bed in a solid breeder. In typical solid breeder modules, a high pressure helium coolant runs through the containing structure of ferritic or austenitic steel surrounding the

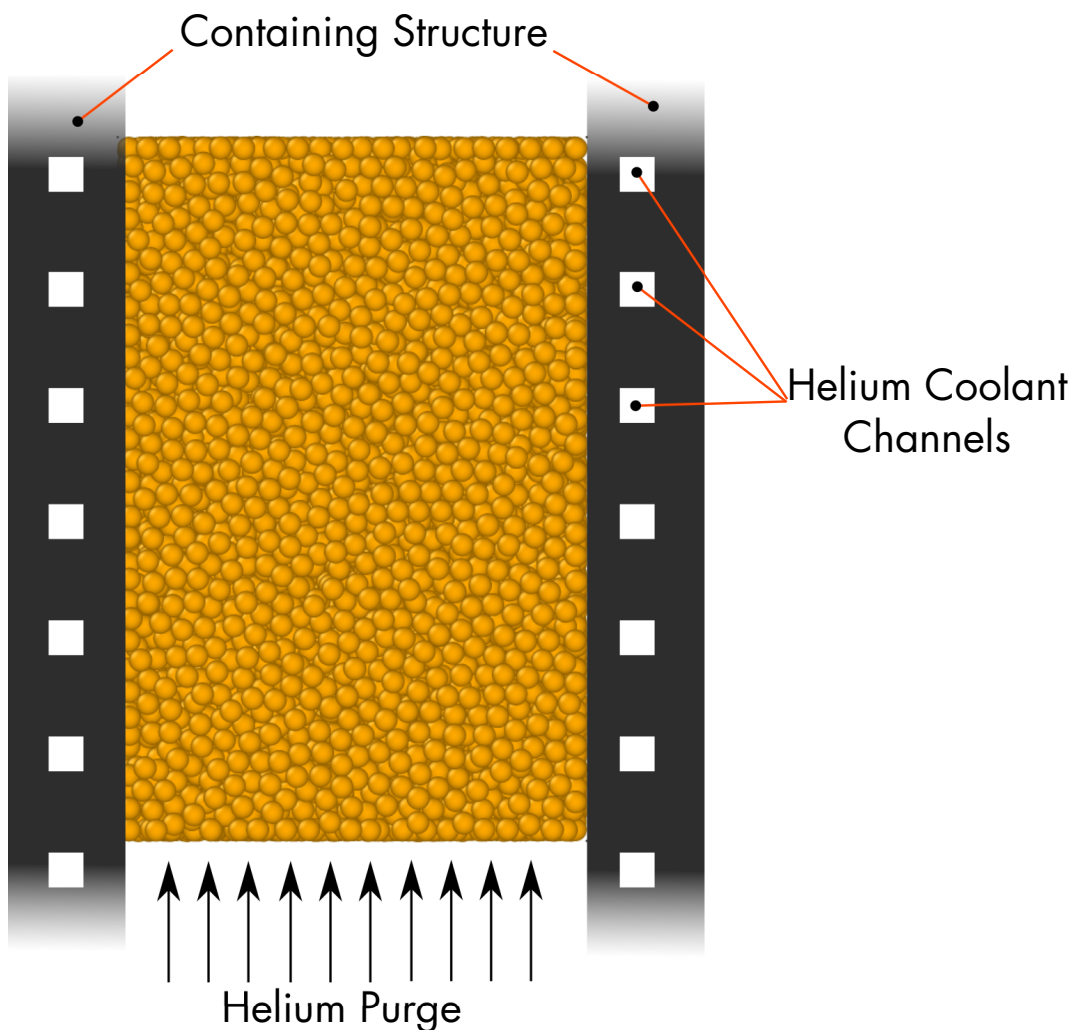


Figure 1.4: Sketch of a typical unit of a pebble bed tritium breeding zone. The pebble bed is cooled with contact to the containing structure.

pebble bed; the coolant will heat to approximately 500 °C before exiting the blanket. A low-pressure, low-speed purge gas is pumped through the pebble bed to extract the tritium generated and transport it out of the blanket for processing.

In addition to breeding tritium, the blanket will be responsible for power extraction in the fusion reactor. The blanket must function to capture the kinetic energy of neutrons (80% of the fusion energy is carried by the neutron), secondary  $\gamma$  rays, and the surface radiation on the plasma-facing first wall (an integral component with the blanket). The blanket must also be able to convert the fusion's energy into high quality heat that can be extracted into the power cycle connected to the fusion reactor.

The dual role of the breeding blanket to generate heat and tritium forces a specific operational temperature window for the ceramic pebble beds. The low end of the temperature window is governed by a minimum temperature for acceptable release rates of tritium from the ceramic to the purge gas; the value is generally set around 300 °C. The upper limit of the temperature window is chosen to avoid sintering of the lithiated ceramic. Tritium that transmutes from the lithium inside the pebble must diffuse slowly through the bulk until reaching a grain boundary. Tritium moves relatively quickly along the grain boundary until reaching a surface of open porosity where it may desorb into the passing purge gas.<sup>33</sup> Based on this understanding of tritium release from the pebble, sintering of the ceramics, as grains in individual pebbles merge, is predicted to reduce the rate of tritium release. The upper end of the temperature window is therefore generally set around 900 °C.

The size of breeder region is limited by the operational temperature window that must be held in spite of the the poor effective conductivity of packed beds of ceramic pebbles. The conductivity is experimentally shown to be a weak function of external pressure but can generally no greater than about 1W/mK – for well-packed beds. Because the effective conductivity and packed bed-wall interface conductance is predominately a contact conduction, disruptions to the packing structure will have considerable impact on the heat transfer of the packed bed.

Moreover, as nuclear energy is deposited into the poorly-conductive ceramic breeder

material and the temperature climbs well above the containing structure, it will confine the thermal expansion of the lithium ceramic and lead to mechanical stresses at the points of contact of the individual pebbles in the packed bed. Engineering design issues surrounding this thermally-induced stress is of great concern to researchers and will be the focus of much of this report.

# CHAPTER 2

## Motivation

### 2.1 Pebble Bed Integrity, Thermophysics, and the Role of Modeling

The pebble bed will experience a constrained thermal expansion as the hot ceramic pebbles press against the relatively cooler container. The restricted thermal expansion of the pebble bed causes an external pressure on the pebble bed. The external pressure may lead to a number of phenomena that disrupt the initial packing – and by extension the initial predictions of thermal and mechanical properties – of the pebble bed. For one, in experiments of even well-packed ensembles of pebbles, the beds show an apparent plastic strain of rearranged packing that increases with maximum historical stress on the bed.[cite Chunbo and Reimanns experimental papers] Without careful engineering and packing of the virgin pebble beds, plastic strain in the pebble bed will directly lead to the formation of gaps between the pebble bed and containing structure. Depending on the configuration of the solid breeder design, the gap could cause a tremendous loss of heat transport from the pebble bed to the coolant. Furthermore, any gaps formed in the blanket could lead to more neutron leakage and decreased tritium breeding ratios and detriment to the blanket’s shielding function.

Additionally, assuming that the plastic strain is removed from the pebble bed, the thermally-induced pressure on the pebble bed will be balanced by the individual pebbles pressing into each other at small points of contact. The small area over which the contact forces are applied leads to stresses which may crush individual pebbles in the ensemble. With the potential accumulation of many cracked/crushed individual pebbles, the overall

packing structure is again altered. Depending on the extent of crushing, the response of the pebble bed may be as benevolent as a negligible decrease in effective thermal conductivity or malevolent as a loss of physical contact and heat transport from the pebble bed to the coolant.

Finally there are long-term effects expected in the materials experiencing prolonged exposure to cycling irradiation, heat, and stress. Thermal ratcheting, swelling, sintering, or thermally-induced creep can lead to evolutions in thermophysical properties even in the absence of cracked pebbles. As the thermophysical properties evolve, global or local bed temperatures change and ultimately the tritium release characteristics of the bed deviate from any prediction one may have had from the initial packing of the ceramic pebble bed.

In our group we are most focused on maintaining tritium breeding characteristics of the pebble bed at desirable levels and thus maintaining temperatures in the breeding region. Alleviating any of the issues that may plague the ceramic breeder all boil down to requiring temperature control via an understanding and of the morphological changes of the ceramic packed beds and their interaction with the interstitial purge gas and structural container. [say how temperature control is possible with better models] In this work we introduce enhancements and new elements to build upon the understanding from ceramic breeder models of past research efforts.

## 2.2 Scope of the Work

The objective of this dissertation is to develop numerical models of ceramic pebble beds, based on first principles and experimental observations, to simulate the hysteretic evolution of pebble bed morphology and predict the subsequent changes to heat transport characteristics after thermally-induced damage to pebbles. The numerical tools are constructed in the following progression: 1. Transient DEM code of inter-particle interactions is employed to simulate packed bed restructuring in the wake of crushed pebbles from the ensemble and the effective thermal conductivity following the restructurin, 2. Transient, volume-averaged equations of Navier-Stokes and energy of the helium purge gas are coupled to the DEM

model of pebbles to simulate conjugate heat transfer and the interstitial fluid influence on thermophysical properties after crushing events, 3) Complete simulations of the tortuous path of helium purge gas with lattice-Boltzmann models to expose flattened temperature profiles due to laminar mixing in the pebble bed, 4) Single pebble experiments to both deduce proper material properties to employ in the DEM framework as well as develop crush-prediction models, 5) To apply the modeling tools to a thermal evaluation of coolant designs of pebble beds in solid breeder blankets in ITER.

A thorough understanding of the evolution of pebble bed morphology and the impact on thermophysical properties is critical for solid breeder designers. The understanding allows for temperature control of breeder pebble beds over the entire lifetime of the blanket which is crucial to the function of the solid breeder for tritium and energy generation. Thus we aim to provide designers of packed beds with tools to understand how packing states may evolve from time-dependent phenomena (e.g. sintering, creep, pebble cracking, etc.). These phenomena may, for instance: decrease the effective thermal conductivity which will raise bed temperatures beyond initial predictions, produce isolated pebbles which will sinter and potentially decrease tritium release rates, or even form gaps between pebble beds and containing structures leading to divergence from properties of the initial packing of the bed.

The objective of this work fits into the broader mission of our research group in the UCLA Fusion Science and Technology Center to develop and apply complete numerical models of ceramic pebble bed solid breeder modules. Any complete numerical model for a pebble bed would require the interaction of many sub-models or sub-functions operating at disparate scales. To demonstrate, a possible top-level algorithm could proceed in the following way: To begin, one must have knowledge of the interaction of the pebble bed with the containing structure as they exist in a fusion environment. The interactions are generally analyzed via the finite element method to find internal stresses and temperature fields of the entirety of the pebble bed and surrounding container. After the internal fields are mapped into the bed, one would use the discrete element method (DEM) to interpret the macroscopic stress fields into the inter-particle forces. With the inter-particle forces and total absorbed thermal

energy calculated, a prediction of the initiation and evolution of morphological changes (i.e. crushed pebbles, sintering, creep, etc.) to each computational volume. Following this, DEM would calculate new effective properties as a result of the morphological changes to the pebble bed region. Finally, the updated bed properties would feed back into the FEM formulation to update calculations in the macroscopic stress fields. While a suite of integrated numerical tools that follows this example algorithm is the ultimate goal of our group, the work of this dissertation is focused entirely on the development of pebble-scale simulations that are predominately in the realm of the discrete element method.

In the following subs-sections, we briefly outline the studies fitting into the scope of this dissertation.

### **Discrete Element Method Study on the Evolution of thermo-mechanics of a Pebble Bed Experiencing Pebble Damage**

In the first study of § 12, we analyze the effective thermal conductivity of a pebble bed assuming different fractions of pebbles in the ensemble are completely crushed. The focus of this study is to determine the extent of change in aggregate ensemble properties due to individual pebble crushing, relate the changes in effective conductivity to quantifiable pebble-scale properties (e.g. contact force, coordination number, etc.), as well as help designers anticipate acceptable limits of pebble loss from a thermal management point of view. For the DEM tools used in this study, the only mode of heat transfer is conduction between the solid particles.

### **Coupling DEM Models of Ceramic Breeder Pebble Beds to Thermofluid Models of Helium Purge Gas Using Volume-averaged CFD**

In a fusion breeder, the helium purge gas winding through the interstitial gaps of the pebbles has a substantial contribution to overall heat transfer.<sup>3,78</sup> The model of § 12 is improved to include the flowing interstitial gas. In § 13, we continue to employ our DEM tools to provide

particle-scale information such as contact force, but couple the pebbles to a volume-averaged computational fluid dynamics (CFD) code. The coupled CFD-DEM model is again used to simulate the heat transfer in packed beds of ceramic spheres that experience pebble crushing – but now investigate the impact of a flowing interstitial helium purge gas when pebbles are crushed.

### **Lattice-Boltzmann Method Integrating DEM Packing Structures to Study Lam-inar Mixing**

The models to account for helium purge gas employed in the studies of §§ 13 and 15 assume effective drag or heat transfer coefficients for pebbles in a computational volume and then include the pebble influence through effective source/sink terms in the momentum and energy equations. The volume-averaged approach allows for simpler meshing of the fluid volume while still retaining much of the physical realism of the system. Complete models of the conjugate heat transfer of both the fluid moving through the tortuous interstitial gaps pebble beds pressing each other with small contact areas are intractable with current computational hardware and finite-element modeling techniques. To overcome deficiencies in computational power, in § 9, we apply the lattice-Boltzmann algorithm to our pebble bed with helium. The lattice-Boltzmann method (LBM) is a non-traditional fluid simulation technique that allows us to resolve pebble-scale interactions with bed-scale conjugate heat transfer with flowing gas on realistic simulation time scales. The LBM approach is applied to the same pebble beds analyzed in § 13 to provide comparison between the two modeling techniques. Furthermore the LBM model, accounting for the complex helium purge gas pathways, provides more insight to the influence of helium on the heat transfer in the heat transfer of packed beds.

## Modeling Tools to Study Coolant Designs of ITER Solid Breeder Module Volumes

In the study of § 15, we apply our coupled CFD-DEM computational tools to the analysis of ITER-relevant solid breeder geometries. In this study we consider the combined effects of pebble crushing, packing restructuring due to both gravity and the unbalanced force network in the pebble bed, and convection from helium purge gas on temperature profiles in solid breeders for different breeding configurations. In typical solid breeder modules, coolant fluid runs through the containing structure surrounding the pebble bed. Heat is removed from the pebble bed predominately through inter-particle conduction and contact conductance of many pebbles pressed against the containing surface. As such, heat transfer out of the pebble bed relies on maintaining good pebble-pebble and pebble-wall contact. However, physical contact is interrupted to different degrees when a pebble bed responds to various amounts of individual crushed pebbles. Furthermore, the restructuring of the pebble bed after a pebble crushing event is, in part, dependent on gravity forces acting upon each pebble in the ensemble. We investigate two representative pebble bed configurations where heat is removed from the bed via inter-particle conduction, convection of purge gas, and contact between the pebble bed and its container. In the first, the coolant containing structural walls (heat transfer walls) are oriented parallel to the gravity vector. In the second configuration, the heat transfer walls are perpendicular to the direction of gravity. To simulate a crushed pebble, we replace the pebble with many smaller, non-cohesive elements while maintaining mass-conservation between the original solid pebble and crushed fragments. The fragments are then free to resettle into interstitial gaps and the rest of the bed resettles as determined by forces from gravity, contact of neighboring particles, and even the small influence of the moving purge gas. The thermo-fluid interaction with the helium purge gas will be included with volume-averaged Navier-Stokes and energy equations. The representative solid breeder volumes will be compared with respect to their temperature peaks and profiles and how those temperatures vary as a function of the percentage of crushed pebbles in the ensemble. The results can be used to optimize solid breeder pebble bed designs through the choice of

breeding zone orientation relative to the gravity vector.

## Experiments on Individual Ceramic Pebbles

In § 10.1, Experiments to crush individual ceramic pebbles have lead to a new predictions on when a pebble will be damaged in a loaded ensemble. § 10.2 – experiments on pebble crushing, using strain energy to convert lab data to ensemble forces.

## Implementation of Enhancements to Standard DEM and CFD-DEM Modeling Tools

The discrete element method, as currently employed by members of the fusion community, begins with the assumption that each pebble is a perfectly elastic material that obeys Hertz's theory for normal interaction. This assumption impacts the magnitude of inter-particle forces predicted by the models. We scrutinize the Hertzian assumption with single-pebble crush experiments with carefully recorded force-displacement responses and compare them to the non-linear forces predicted by a Hertzian pebble with bulk properties reported in literature. We found each pebble generally has a non-linear force response but with varying levels of stiffness that qualitatively matched the curves from Hertz theory. Assuming Hertzian interaction, we then backed-out an elastic modulus for each pebble. We define a stiffness reduction factor,  $k$ , as the ratio of the pebble's elastic modulus to the sintered bulk value from literature. After determining the  $k$  value for every pebble in our batch, we discovered a probability distribution for different batches. The distribution is attributed to the varying micro-structure of each pebble. We incorporate the results into our DEM algorithms, distributing  $k$  values at random to pebbles satisfying the probability curves of experiments. DEM simulations of pebble beds in oedometric compression are carried out to determine macroscopic responses of stress-strain, contact force distributions at maximum stress, and a prediction of pebbles crushing at that point. In all cases studied in § 11.1, the pebble beds with modified Young's modulus had smaller overall contact forces and fewer predicted

crushed pebbles.

We employ the theory based on experimental results of individual pebble crushing to create modules to attach to DEM tools for predicting pebble crushing in ensembles in § 11.3. On a small ensemble of pebbles, we simulate a uniaxial compression test with the pebble crushing module activated in the DEM code. Our group has also experimented on pebble beds to measure the percent of damaged pebbles under certain loads and load cycles. The results of our uniaxial compression test in DEM can be scaled up to compare to the experimental results on pebble beds.

In § 11.2, we introduce a correction to the heat transfer coefficient used in the CFD-DEM framework to account for low conductivity and high heat generation inside of particles. In the discrete element method (DEM), an innate assumption in the computational framework is of isothermal DEM particles. When DEM models are coupled to volume-averaged Navier-Stokes models of purge gas flow, the accuracy of the lumped capacitance method is quantified with the Biot number. For moderately sized Biot numbers ( $\text{Bi} > 0.5$ ), the lumped capacitance method is inaccurate for both steady-state and transient temperatures for a particle with heat generation. We introduce a correction to the heat transfer coefficient which allows the lumped capacitance assumption of the DEM to be accurate in both transient and steady-state regions. The correction is first compared with an analytic solution of a sphere in a heat transfer flow, then the correction is implemented in codes of coupled computational fluid dynamics with the discrete element method (CFD-DEM). We begin with a test case of a single pebble with heat generation being cooled by a passing gas. The result is compared to both the idealized analytic solution as well as a complete model of the conjugate heat transfer as calculated by the lattice-Boltzmann method (LBM). Once shown to be effective for a single sphere, the correction is used in a study of a sample packed bed and again compared to the more exact result of an LBM computation. The results show the simple correction to be effective at capturing the thermal physics of moderate-to-large Biot numbers while still using the simplified equations of the lumped capacitance method.

In § 11.4 we show that proper modification of material properties, we can dramatically

increase the timestep and thus decrease the total time of simulation. In our thermal DEM simulations, the time to reach steady state can often take hundreds of real-time seconds owing to the poor thermal transport in the ceramic pebble bed.

## CHAPTER 3

### Dissertation Outline

In Part II (§§ 4 to 6) we survey the state of the art in analysis of ceramic pebble beds, contact mechanics, and modeling thermal and mechanical interactions of particles in packed beds and fluids moving interstitially. In Part III (§§ 7 to 11) we outline the numerical methodology and development of modeling tools we shall use in the study and analysis of pebble beds and their evolving morphology due to external loads. We compartmentalize the numerical tools into three parts, namely: the discrete element method (DEM), coupled computational fluid dynamics and the discrete element method (CFD-DEM), and a lattice-Boltzmann method (LBM) we integrate with DEM. The tools are then used to cover a range of studies in Part IV (§§ 12 to 15). Finally, in Part V, we discuss the next steps to be take that are necessary but beyond the scope of this dissertation as well as other research avenues that have been opened by the tools introduced here.

## **Part II**

# **Literature Review**

## CHAPTER 4

### Status of Ceramic Breeder Modeling and Analysis

A common problem plaguing the study of packed beds is the disconnect between the scale of physics influencing the behavior of the packed bed and the scale of quantifiable and measurable physics in experiments. In the laboratory we are limited to measurements such as the stress and strain of the entire packed bed and then are left to infer how the internal packing of the ensemble leads to the measurable values. Unfortunately, the stress-strain response of a packed bed is often not unique to a specific ‘state’ such as one might use to describe an ideal gas. Nevertheless, considerable work has been done by experimenters at characterizing properties of a wide range of pebbles types and materials.

In § 1.2, we described how thermally-induced stress arises in the ceramic breeder volume. Research efforts have therefore been aimed at developing a thorough understanding and characterization of the thermo-mechanics of ceramic breeder pebble beds. Such an understanding is essential to providing confidence in the performance and lifetime of a ceramic breeder blanket design. In particular, a significant effort of the pebble bed thermo-mechanics study is on the development of modeling simulation tools. We will describe, in brief, some of the major experimental findings as they relate to the modeling efforts for ceramic pebble beds.

Reimann *et al.* have conducted an extensive experimental study of the stress-strain relations of the ceramic breeder pebble beds using an oedometric test apparatus.<sup>69,75,76,78,79</sup> The most significant macroscopic experimental phenomena witnessed in the pebble bed are an irreversible plastic strain when the load is removed, a non-linear elasticity, a pressure-dependent plasticity, and a volumetric creep. A particularly noticeable feature, clearly

demonstrated in Fig. 4.1, is the reduced amount of irreversible strain when subjected to additional loading cycles after the first unloading. This may suggest the existence of a semi-equilibrium packing state in the pebble bed which can be reached after applying a pre-load to account for the large strain in the first cycle of a pebble bed. This semi-equilibrium packing state is a feature which may be advantageous for use in a fusion reactor.

Zhang *et al.* ran similar cyclic pressure experiments to illuminate the existence of more steady stress-strain responses of packed beds under different pressures.

To study the temperature effect in Reimann's studies, the bed is freely heated to the desired working temperature before the pressure load is applied. Under the same loading condition, the bed behaves much softer at higher temperatures. The bed stiffens as the pressure increases. An illustration of this phenomenon is presented in Fig. 4.2 for a lithium orthosilicate pebble bed between 50 – 850°C. At higher temperatures (such as > 650°C), a creep-like behavior becomes apparent. The creep behavior allows the pebble bed to relax and sustain higher stresses, however one needs to avoid sintering. The data was used to correlate creep rate as a function of temperature, stress, and time for both lithium orthosilicate, lithium metatitanate, and beryllium pebble beds.<sup>12,77,79</sup>

When we consider the pebble bed from the standpoint of engineering continuum mechanics, packed beds cannot be adequately described by traditional models of either solids or liquids alone. Under compression, a packed bed responds like a solid with non-linear elasticity and a plasticity that is history-dependent. At the same time, the packed bed can obviously not support any tensile pressure and will often behave as an extremely viscous liquid as it may fill in voids under just the force of gravity. Nevertheless, phenomenological models, derived from the volumes of collected data, have been developed, using effective material properties for the ceramic pebble bed, that describe the pebble beds in an Eulerian manner that provide reliable information on the initial states of breeder volumes in the fusion reactor environment and allow reasonable design predictions of the thermo-mechanics of the breeding blanket.

In spite of the shortcomings of a continuum approach, it is the only option which currently

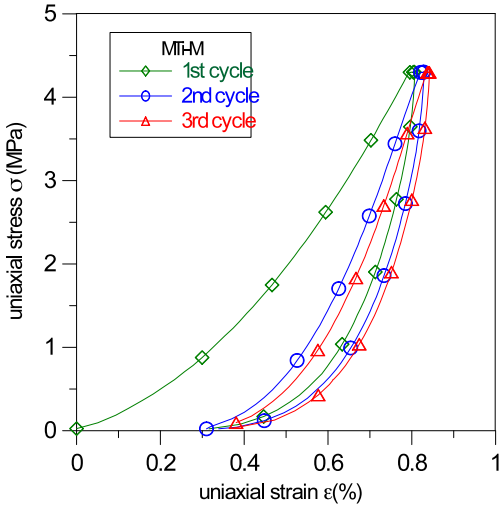


Figure 4.1: Example of uniaxial compression testing results for lithium metatitanate pebble bed.<sup>91</sup>

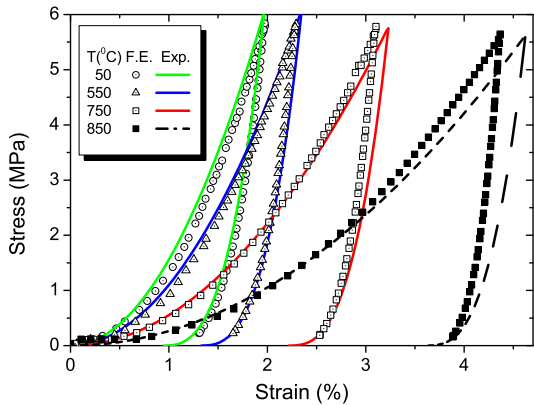


Figure 4.2: Example of uniaxial compression testing results compared with predictions from material constitutive equations for lithium orthosilicate pebble beds at different temperatures.<sup>38</sup>

allows treatment of the pebble beds with standard finite element modeling (FEM) that can be scaled up to the breeder system. To employ FEM, mathematical models written in terms of average quantities and containing effective parameters are used. These models deduce a

set of constitutive equations to be implemented in the framework of a finite element code. There are two major variants of phenomenological modeling approaches developed among institutions, including: (1) A non-linear elastic model and a modified Drucker-Prager-Cap theory for plastic strain;<sup>35,37</sup> and (2) A hyper-porous non-linear elastic model and a Gurson model for the plastic model.<sup>25–27</sup> Another approach was taken by Ref. <sup>35</sup> wherein the authors employed two different elasticity laws for the loading and unloading branches. Alongside the development of the modeling techniques, several large scale pebble bed thermo-mechanics experiments were conducted. These experiments were intended to reveal the underlined thermo-mechanical characteristics of ceramic breeder pebble beds, and provide data for benchmarking the developed models. The vast amount of work done on modeling the pebble beds in the FEM framework can be found in literature.<sup>25,25,26,26,26,28,28,28,37,37,37,39,41,42</sup> A study was also published in 2012 that summarized, compared, and highlighted features of the models under development at the time.<sup>101</sup>

We will devote the rest of this chapter to the discussion of advances of an alternative modeling approach for solid breeder analysis. In this modeling strategy, we consider the pebble bed as a system of distinct interacting bodies that are subject to fundamental forces which result in independent motions. This modeling approach, called the discrete element method (DEM), is the framework upon which the work of this dissertation is laid, as such we will go into more detail on the history of DEM’s use in fusion science and technology research.

## 4.1 DEM for Tritium Breeders

A thorough review of the physics behind DEM will be given in § 12. For now, we will simply discuss some major results of the implementation of DEM in solid breeder research.

The Discrete Element Method (DEM) introduced by<sup>23</sup> has been shown to be a promising tool to study the behavior of granular systems through the interaction between the individual particles. DEM was first applied to study the micro-mechanical aspects of cyclic thermal loads on the relaxation of stress in pebble beds for fusion reactors.<sup>60,102</sup> An iterative relax-

ation strategy of DEM was used to study the internal contact forces in a pebble bed under an external load by An *et al.*<sup>36</sup> The same DEM tools, and the insight provided by which, were also used to initiate DEM-based investigations of creep between pebbles under thermal and mechanical loads.<sup>4</sup> While An *et al.* studied the pebble assemblies in rectangular and cylindrical containers bounded by elastic walls, computational requirements prevented more than a few thousand particles in the ensemble with rigid walls.<sup>36</sup> Following An's work, the DEM torch was passed across the pond to researchers at KIT where they began to improve upon the initial studies begun at UCLA.

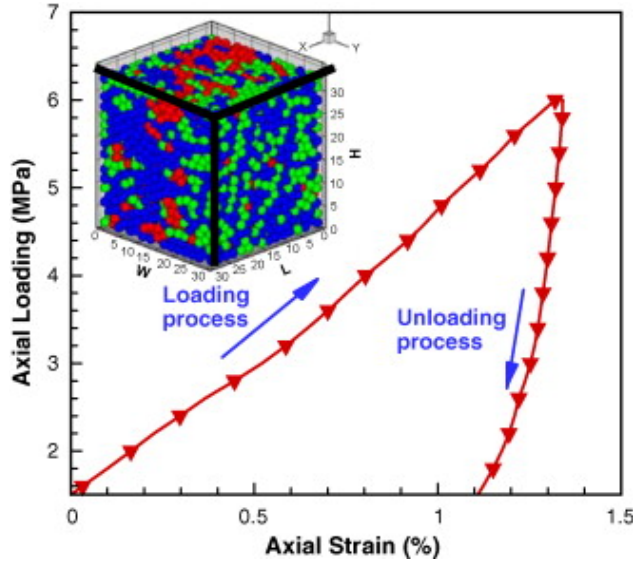


Figure 4.3: Stress–strain behaviors of granular materials in a rectangular box under uni-axial compaction from DEM are qualitatively matched to behaviors seen experimentally.

The effect of packing factor, geometry of the assembly on the overall stress-strain response under uni-axial compression tests (UCT) has been thoroughly investigated.<sup>40</sup> Gan *et al.* pebble assemblies in a cubic box with periodic boundary conditions to prevent the influence of boundaries dominating the ensemble response to loads.<sup>44</sup> In the DEM uni-axial compression studies (see Fig. 4.3), a non-linear stress-strain response and a characteristic residual strain after unloading (analogous to plastic strain in continuum systems) is observed akin to the experimental results.<sup>74</sup> It was shown that the average coordination number, average normal contact force and the maximum normal contact force in the assembly has a

unique functional relation (nonlinear, linear and linear, respectively) with the hydrostatic pressure or the applied pressure independent of the packing factor.<sup>4,40</sup> These functional relations may be used as master curves for the micro-macro correspondence in the pebble bed thermo-mechanics studies.

Recently, the effect of the pebble size distribution on the overall thermo-mechanical behavior of the pebble assembly is studied by Annabattula *et al.*<sup>5</sup> They consider the pebble size distribution of ceramic breeder pebbles ( $\text{Li}_4\text{SiO}_4$ ) with a diameter range of 0.25 mm–0.65 mm. Figure 4.4 shows a binary pebble assembly in a periodic box. The colors indicate stored elastic strain energy of the pebble (red: maximum and blue: zero). The assembly has a maximum pebble radius  $r_g = 0.25$  mm with the pebble size ratio  $r^* = r_s/r_g = 0.6$ , relative volume fraction  $V^* = V_g/V = 0.7$  and a packing factor  $\eta = 0.643$ . The average stress in a granular assembly can be deduced from the contact forces between individual grains.

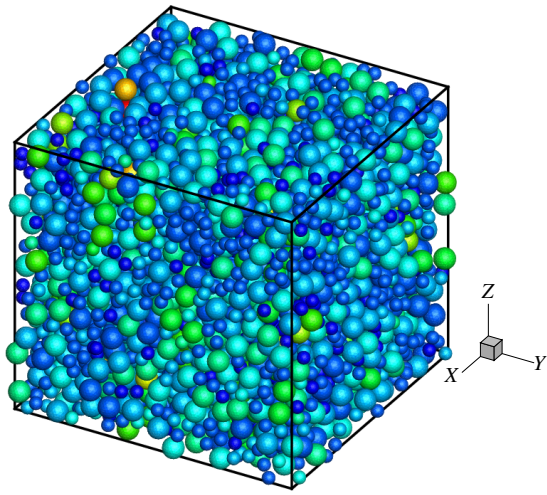


Figure 4.4: A binary pebble assembly with  $r^* = 0.6$  and  $V^* = 0.7$  showing the stored elastic energy of the pebbles at  $\epsilon_{33} = 1.5\%$ ; pebbles of radius  $r_s$  (small) and  $r_g$  (large).

Another aspect of interest in the study of mechanics of pebble beds is the crush behavior of individual pebbles and their impact on the over all pebble bed response. DEM was used to study the behavior of a crushable pebble assembly with the crush load data for  $\text{Li}_4\text{SiO}_4$  pebbles (for individual pebbles) measured at KIT for pebbles of diameter 0.5 mm.

A probabilistic method for analyzing the crush events of individual pebbles and a procedure with the combination of DEM and experimental data to obtain crush load probability has been reported by.<sup>42</sup> Figure 4.5 shows the cumulative distribution function as a function of the hydrostatic pressure placed on the bed. The probability analysis, derived from DEM calculations, provides quantitative report of pebble crushing as a function of a specific hydrostatic pressure. The results of this analysis exemplify the growing strength of DEM techniques for analyses connecting global pebble bed loads to individual pebbles.

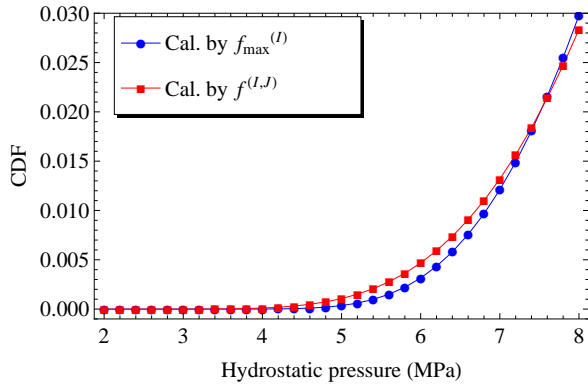


Figure 4.5: Cumulative distribution functions for crushing of individual pebbles inside the bed for as-fabricated pebbles, calculated by (1) maximum contact forces and (2) all inter-particle contact forces.<sup>42</sup>

However, it has been shown<sup>105,108</sup> that a criterion based on critical stored elastic energy is the most suitable criterion for describing the  $\text{Li}_4\text{SiO}_4$  pebble failure. Hence, the crush load data (provided by fusion materials laboratory at KIT) has been transformed into equivalent elastic strain energy showing a Weibull distribution.<sup>105</sup> This critical energy (randomly generated distribution) is used as the criterion for failure of pebbles in the DEM simulations. First, the assembly is loaded up to 3% strain in uniaxial compression and then unloaded to a stress-free state. The elastic modulus of the pebble is reduced (from initial value to a small value of 1 kPa) with increase in elastic strain energy of the pebble according to a phenomenological damage accumulation law citeAnnabattula2011b. The damage state is frozen at the end of loading step and hence there will be no further damage accumulation in

the unloading step.

Figure. 4.6 shows the results for two types of damage law each with three different realizations. Each realization corresponds to a different random distribution of critical energies assigned to the pebbles in the assembly. The results do not show appreciable sensitivity to random distribution of energies. In the case of gradual damage law, the reduction of the elastic modulus of the pebble starts when the stored elastic energy reaches 50% of the critical energy for that pebble and the elastic modulus reaches exponentially to its minimum value when the stored elastic energy reaches the critical energy prescribed. In the case of sudden damage this reduction starts at a much later stage when the stored elastic energy reaches 95% of the critical energy of the pebble. Clearly, the assembly with a sudden damage accumulation shows a higher maximum strength compared to the gradual damage. In the case of the gradual damage, the pebbles start to degrade much earlier (at small strain) than in the case of sudden damage. Hence the critical number of pebbles to fail for the onset of maximum strength is reached earlier (at small strain) in gradual damage. It turns out that a mere 0.2% pebbles is the critical number for the onset of maximum strength (stress plateau) observed.

The nature of damage evolution influences the maximum strength and strain at which the maximum strength is attained while the critical number of failed pebbles for this saturation is independent of the damage evolution law (also see<sup>105</sup>). Also note that the high frequency oscillations during loading in the stress-plateau region represent the failure of new pebbles. The current analysis also shows a creep-like behavior of the stress-strain response and hence the stress-plateaus observed in the experiments<sup>74</sup> may indicate the presence of pebble crushing in addition to the thermal creep mechanism. Furthermore, the residual strain after unloading is large for the system with sudden damage than the system with gradual damage. It should be noted that the assembly with gradual damage has more number of damaged pebbles at the end of loading (at 3% strain) making the assembly more compliant than in the case of sudden damage.

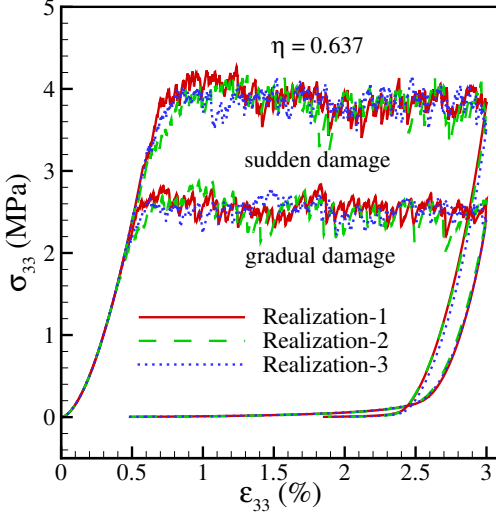


Figure 4.6: Stress-Strain response of a granular assembly under uni-axial compression for two different damage evolution laws (gradual and sudden). Each damage evolution criterion is simulated with three different realizations of randomly prescribed critical failure energy for individual pebbles following Weibull distribution.

## 4.2 Experimental Pebble Bed thermo-mechanics Studies

### 4.2.1 Out-of-pile experiments

The constitutive equations developed for finite element models were derived from the uniaxial compression experiments, which are not fully representative of fusion operating conditions. A more prototypical experiment should subject a pebble bed to isostatic loading. This could be generated by either an in-pile pebble bed experiment or by making use of differential thermal expansion between a pebble bed and its containing structure. The latter has been attempted with several out-of-pile experiments launched by the HE-FUS 3 facility at ENEA Brasimone. The experiments investigated the thermo-mechanical behavior of pebble beds within geometry much more representative of current breeder designs. These include the medium-scale mock-up exercises of HELICA (HE-FUS3 Lithium Cassette) and HEXCAL-

IBER (HE-FUS3 Experimental Cassette of Lithium Beryllium Pebble Beds).<sup>24,27</sup> For those experiments, the pebble layers are heated by electric heaters, and temperature and displacement were measured.

#### 4.2.1.1 FZK Benchmarking

FZK has performed validation of their FEM code against the data collected from the HELICA experiment.<sup>38</sup> They have also reported the results of simulations of HEXCALIBER but have, as yet, not directly validated against the collected experimental data.<sup>39</sup>

In the HELICA experiment, the pebble beds experienced six thermal ramps, each applied for an hour, and then the pebble beds were actively cooled with a helium flow. After cooling, the pebble beds were subjected to the another thermal ramp and the process was repeated. DIN reports<sup>24</sup> that the pebble bed temperatures exhibited cyclical behavior. FZK simulated two cycles of the HELICA test and an example of the calculated results and experimental data are shown in Fig. 4.7 and Fig. 4.8. In Fig. 4.7 we see temperature histories at a particular location (100 mm from the first wall) during a loading-unloading cycle. The simulation results follow the temperature increase during the thermal ramps up until the seventh hour, then again follow the experimental data as the test rig is cooled with the helium coolant. Even with the two-dimensional simplification of the model, there is excellent agreement between calculations and measurements. In Fig. 4.8 the displacement calculated by FZK is also in strong agreement with the average of measured displacements for the entire duration of the heating-cooling cycle. Because of the overwhelming amount of computer time necessary for the FZK model to complete a fully three-dimensional and transient simulation, the FZK computations of HELICA and HEXCALIBER are carried out in two dimensions; the helium temperature is chosen at an average value of measured inlet and outlet temperatures.

From FZK's numeric simulation arise several important observations: (i) a three-dimensional analysis would provide more detail, spatial temperature variation of e.g. coolants would likely explain much of the deviation between temperature profiles predicted by the simulation and

measured in the HELICA experiment; (ii) gap formations, with sizes on the order of a pebble diameter, were detected at the interface of the first wall in ceramic beds; (iii) the maximum hydrostatic pressures seen in the ceramic bed are anticipated to be above the fracturing limit of the lithium ceramic. The consequences of some of these observations, if true and real, are severe enough that they merit careful attention. Gap formation and pebble failure (crush or fracturing) are important topics that must be considered in validation with future experiments.

#### 4.2.1.2 DIN Benchmarking

Because of the characteristics of the DIN model, full three-dimensional simulations were capable of being relatively easily performed. In the framework of benchmarking efforts, DIN has performed validation of their model against experimental results of HELICA, shown in Fig. 4.9 as well as HEXCALIBER, shown in Fig. 4.10.

The results of the DIN model show also strong agreement to the experimental results of HELICA as demonstrated in one example of temperature histories shown in Fig. 4.9. In this profile, the same location as that modeled by FZK (100 mm from the first wall) is simulated by DIN. The FEM simulations from DIN (Fig. 4.9) are reported over the six-hour heating portion of a single heating ramp cycle of HELICA. When comparing the results from DIN with those of FZK (in Fig. 4.7 and Fig. 4.8) we see the DIN model has slightly better predictive capabilities for the temperature histories. This may be due attributed to the three-dimensional variations in coolant temperature being captured by the DIN model.

Unfortunately, the ambitions of HEXCALIBER were limited due to the crippling of several heaters. Nevertheless, the limited data was still used in efforts to validate the constitutive relationships of the DIN model. The temperature variations with time were the only major result reported by the ENEA Brasimone team, such as that shown in Fig. 4.10; mechanical results are still forthcoming from the research group. From the comparisons to experimental measurements in HELICA and HEXCALIBER it is encouraging to notice that

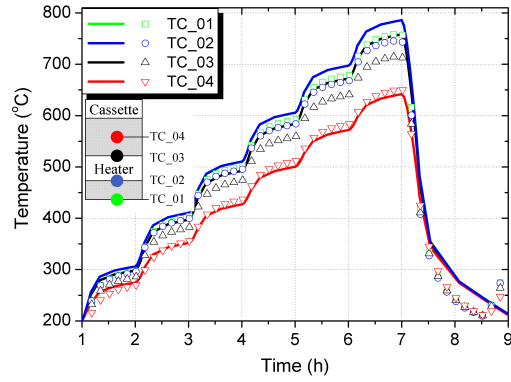


Figure 4.7: Results of the FZK benchmarking with HELICA<sup>39</sup> showing temperature variations with time during a loading cycle ( $T$  in  $^{\circ}\text{C}$ ) at 100 mm from FW.

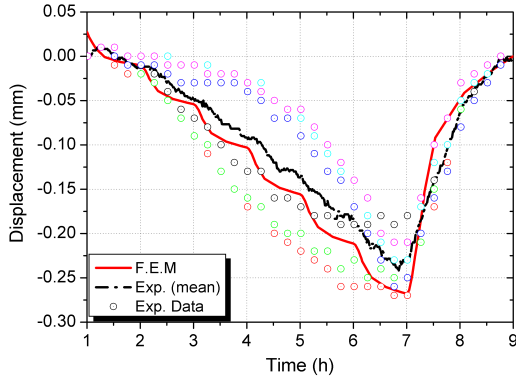


Figure 4.8: Results of the FZK benchmarking with HELICA<sup>39</sup> showing a comparison of displacements (in mm) in HELICA between calculated and measured LVDT values.

even in the absence of a creep model, satisfactorily close agreement were seen between computation and measurement. So far, no detailed displacement comparisons have been made to experimental data.

Several important observations are also made from the results of the DIN simulation: (i) three-dimensional effects were important to calculations of the convective energy transport of the helium coolant; future models should continue to be analyzed in three-dimensions; (ii) DIN reports that in HELICA all ceramic beds experience a compressive force everywhere

and no gap formation is ever detected.

In summary, the benchmarking efforts have only recently begun in Europe. A typical pebble bed thermo-mechanics simulation involves first calculating overall temperature fields of the blanket unit as it undergoes volumetric nuclear heating as well as cooling at the boundaries. The non-linear mechanical analysis is then performed for stress and strain estimations. However, since the effective thermal conductivity of the ceramic breeder pebble bed is, to some degree, dependent on strain, a coupled thermal and mechanical analysis is needed. Additional details on modeling steps can be found in Refs.<sup>24,25,27,28,39,41</sup> The two most developed models, from FZK and DIN, have had their results compared to experimental data and have thus far shown great promise.

However, it must be noted that the benchmarking efforts are incomplete and inconsistencies between the two models must be explained as they move forward. For example, the model of FZK concluded that a gap appeared between the pebble bed and structural wall, however the model from DIN reported no gap formation. The existence of a gap between pebble bed and structural wall will negatively affect the ability to cool the pebble bed and thereby impact structural and tritium release properties of the bed. That such a discrepancy exists between calculated results of the models on such a critical feature warrants either more benchmarking efforts or a careful deconstruction of the constitutive equations to discover the source of the inconsistency. Future experiments aimed at benchmarking ought to focus on creating apparatus capable of expressing, among other things, when gap formation or pebble failure occurs.

#### 4.2.2 Pebble Bed Assemblies Experiment

The pebble bed assemblies (PBA) experiment is designed to study the effect of neutron irradiation on the thermo-mechanical behavior of a ceramic breeder pebble-bed under DEMO representative thermo-mechanical loads.<sup>62</sup> This was accomplished via analysis of changes of the in-pile temperature profiles during irradiation as well as from the post irradiation

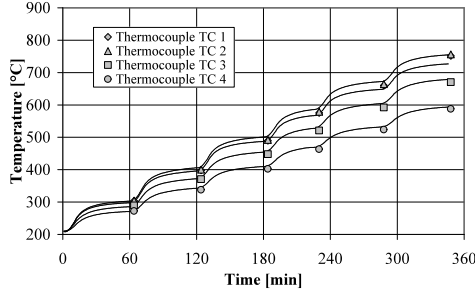


Figure 4.9: Exemplary results of the DIN benchmarking with HELICA: Temperature variations with time during a loading cycle at 100 mm from FW.<sup>26</sup>

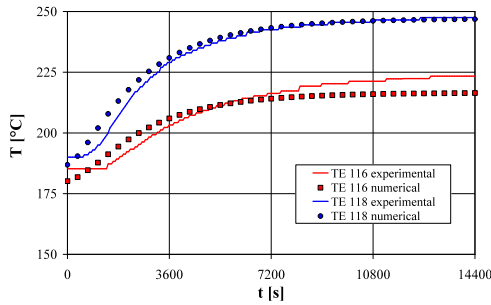


Figure 4.10: Exemplary results of the DIN benchmarking with HEXCALIBER : Temperature variations with time during a loading cycle within the first lithium-orthosilicate cell.<sup>25</sup>

examination of the pebble bed in the Hot Cells. Within the assemblies, there are four test elements; each resembling a small-scale mock-up of a HCPB TBM with a ceramic breeder pebble bed sandwiched between two beryllium pebble beds. Before irradiation, the beds are pre-compacted with a compressive load of 3 MPa to ensure good settling and contact.

FEM analysis was performed to study pre-compaction procedures. During progressive irradiation, temperatures are recorded at several locations in the ceramic breeder bed as well as other critical positions. Reviewing the recorded temperature data, when comparing the temperature in the center of the ceramic breeder pebble bed during later cycles and earlier cycles there appears to be a decrease in temperature for the exact same environmental

conditions. Changes in the pebble beds and their characteristics are examined both in-pile by neutron radiography and out-of-pile by e.g. SEM during post-irradiation examination (PIE). The estimated bed height reduction from neutron radiographies over the course of the irradiation has shown 3% of creep compaction.

A pebble bed experiencing creep compaction is both becoming more dense as well seeing more-developed inter-pebble conduction paths. The effective thermal conductivity for a creep-compacted ceramic pebble bed is thus expected to be higher than a standard ceramic pebble bed. This phenomenon results in lower temperature gradients and a lower overall temperature magnitude, which is precisely what was observed in the experiment over the course of the cycling.

During PIE, various microscopy preparation techniques are used to study the deformation state of the pebble beds (signs of creep compaction and sintering), formation of gas gaps between the pebble beds and structural materials, and the interaction layers between eurofer-ceramic and eurofer-beryllium.

Figure 4.11 shows the cross-section of  $\text{Li}_2\text{TiO}_3$  pebbles (left) and  $\text{Li}_4\text{SiO}_4$  pebbles (right) post irradiation. Evident in the images is sintering of the lithium titanite and significant fracturing of the lithium orthosilicate pebbles. Importantly, however, it must be noted that the pebble beds performed reliably in spite of the changes displayed in these images citemaglielsen2011.

#### 4.2.3 More thermo-mechanics Characterization Experiments

Coming from the standpoint that strain in a pebble bed is induced by thermal expansion, an experiment was conducted to characterize the pebble bed thermal expansion coefficient.<sup>85</sup> The thermal expansion coefficient of a packed  $\text{Li}_2\text{TiO}_3$  pebble bed is measured under a compressive load of 0.1MPa. The study concludes that for beds with packing factors of 65.3 to 68.5%, the average thermal expansion coefficient was  $(1.4 \pm 0.2) \times 10^{-5} K^{-1}$ . This thermal expansion coefficient of the pebble bed was equal to 78% of that for the bulk material under

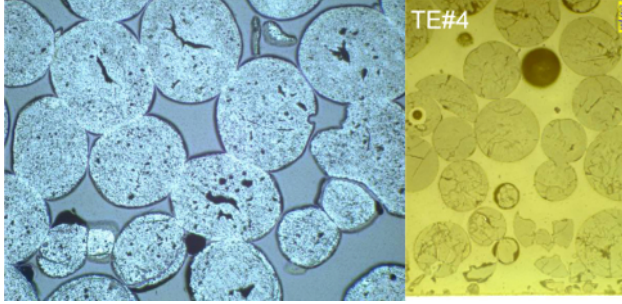


Figure 4.11: Notable features of irradiated  $\text{Li}_2\text{TiO}_3$  and  $\text{Li}_4\text{SiO}_4$  pebble beds from PBACitemagelsen2011. (Left) Demonstration of significant sintering of  $\text{Li}_2\text{TiO}_3$  pebbles with no fracturing; the visible cracks originated from production and handling. (Right) Demonstration of cracking of  $\text{Li}_4\text{SiO}_4$  pebbles.

the conditions used in the study. The reduction in thermal expansion coefficient is less significant than that of the effective modulus, which is more than 2 orders of magnitude smaller than the bulk value.

The effect of thermal cycling on the packing state is of interest; in particular, it is foreseen that the ITER TBM will be subjected to such conditions. The question that arises is whether a void region will be created under thermal-cyclic loading due to the differential rates of expansion and contraction of the pebble bed and structural containing wall. This uncertainty was first addressed in an experimental set-up involving  $\text{Li}_2\text{TiO}_3$  pebbles enclosed by two Kovar flanges while sandwiched between two commercial-grade CVD silicon carbide discs.<sup>13</sup> The set-up allows for generating a high stress through large differential in thermal expansion coefficients. The experimental results indicate that high thermal stresses and deformations are present during the initial thermal cycle of the assembled test article, but are successively alleviated due to a combination of pebble re-arrangement within the bed and creep induced deformation. This suggests that a few thermal cycles under a controlled atmosphere and a compressive load before final assembly of blanket sections would mitigate the severity of the thermal stresses during start-up. This is also shown in a later experiment, in which the increment of compression decreased with each heating cycle and became negligible after 30 cycles.<sup>86</sup> Extrapolating the finding to a prototypical blanket breeder pebble bed design,

the study concludes that for a height of 1 m long pebble bed, a 51 mm high cavity may be generated at the top of the bed with an initial packing of 65% under thermal cyclic operations.

## 4.3 Pebble Bed Thermo-mechanics Summary & Framework

A good deal of progress has been made in the field of ceramic pebble bed analysis. Owing to the multi-scale nature of pebble beds, it is unavoidable that multi-scale models are necessary. A framework has been envisioned by our group, shown in Fig. 4.12, the following of which will contribute substantially to the success of the ceramic breeder blanket development. In this framework, the continuum modeling approach using FEM and empirically derived material constitutive equations is capable of correctly characterizing the stress load to which a breeder pebble bed unit may be subject during reactor operation. The DEM approach analyzes this load and determines the possibility of pebble bed morphological changes; i.e. pebble damage based on the crush load data of pebbles, the degree of sintering depending on the local contact stress and temperature fields, and creep relaxation of contacts. It is only with the combined analysis of particle-scale information from DEM and system-scale information from FEM that warrants a high confidence of success to the assembly and design of breeder units in a blanket. Experiments should also be conducted to assess the manner of pebble relocations and packing rearrangement when morphological evolution of the pebble bed occurs. It is important to learn if the breeder unit will continue to function in accord with the original design goals under all complex operating conditions. The ultimate objectives of the pebble bed thermo-mechanics are: to delineate a near-equilibrium packing state as the initial state, quantify breeder unit thermo-mechanics parameters during operations, understand how these properties evolve as topographical changes happen in the packing, and ensure breeder functions as it is intended to in the fusion operational phase spaces.

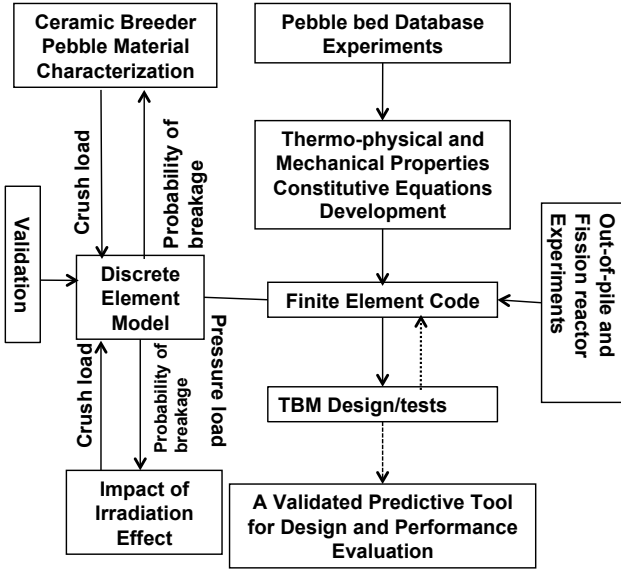


Figure 4.12: Example Pebble Bed Thermo-mechanics Research Framework.

Lastly, no predictive tool is possible without solid validation attempts. The benchmark experiments performed up to now were either too limited in scope or practice. New experiments must be performed that can provide reliable data with which to compare numerical results. Fortunately, a new experimental effort out of KIT has been initiated.<sup>47</sup> The experiment shows great promise at reproducing volumetric heating profiles with substantial data collection efforts. The preliminary results are very promising.

# CHAPTER 5

## Hertzian Contact

In § 7.2, we will lay out the contact interaction mechanics implemented in the discrete element method which include normal and tangential forces and damping. While all the mechanics are important for the fidelity and stability of the DEM simulation, we will focus here purely on the normal elastic contact of two interacting bodies, the analysis which was first performed by Heinrich Hertz in 1882. The results of the so-called Hertzian contact law is vital to many other sections of this work so it is instructive to have the analysis laid out.

We consider two non-conforming solids approaching and then contacting under load. Picture a line connecting the center points of the two bodies and an  $x - y$  plane existing at the midpoint between the bodies and oriented normal to their connecting line. On that surface, there is a radius,  $r$  extending from the connecting line that is related to the  $x - y$  coordinates as  $r^2 = x^2 + y^2$ .

Because we are restricting ourselves to two spheres, the surface of curvature of the two bodies may be written as

$$z_1 = \frac{1}{2R_1}r^2 \quad (5.1a)$$

$$z_2 = \frac{1}{2R_2}r^2 \quad (5.1b)$$

respectively. As the two bodies approach, just before the surfaces are in contact, points on the two surfaces are separated by a distance  $h(r)$ ,

$$h = z_1 - z_2$$

$$h = \left( \frac{1}{R_1} + \frac{1}{R_2} \right) \frac{r^2}{2} \quad (5.2)$$

Noticing this term in the separation, we define the relative radius of curvature as

$$\frac{1}{R^*} = \frac{1}{R_1} + \frac{1}{R_2} \quad (5.3)$$

and then the separation is simply  $h = (1/2R^*)r^2$ .

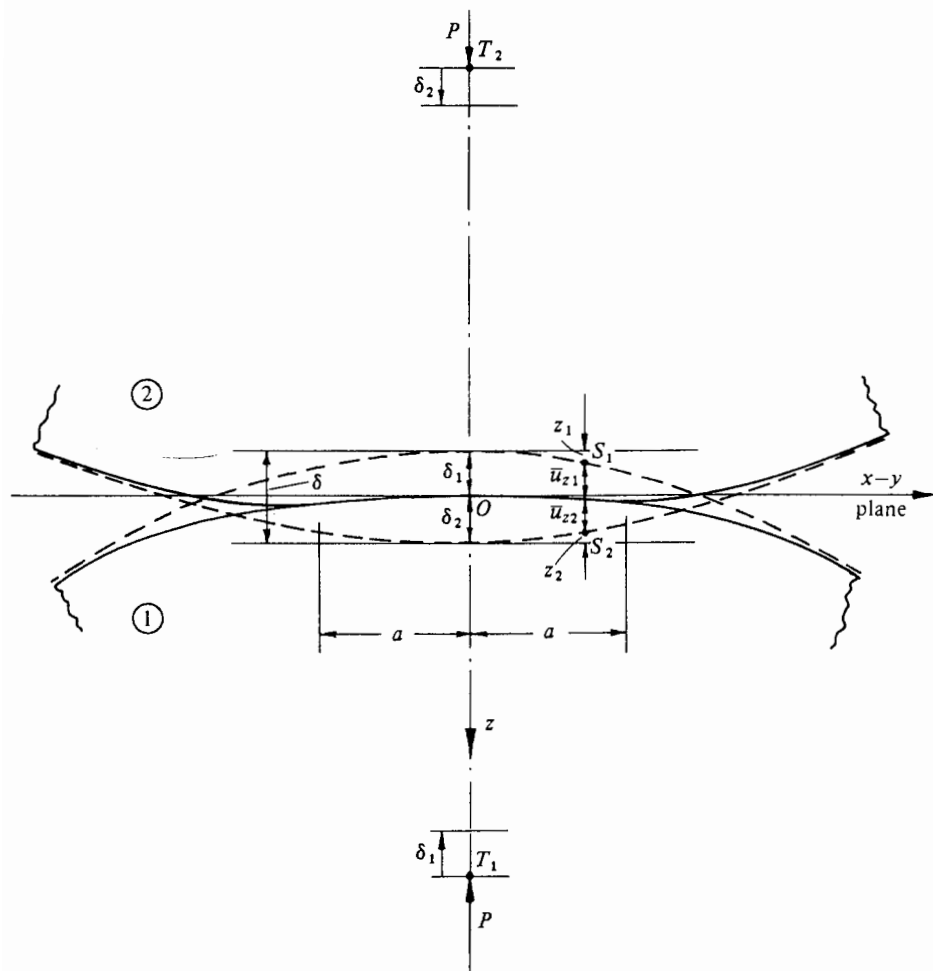


Figure 5.1: default

The two bodies continue their approach towards each other until finally, under an external load  $F$ , come into contact. The cross-section of these bodies after contact are shown in Fig. 5.1. If we first imagine that the two surfaces do not interact and their surfaces pass through each other unimpeded, their surfaces would be overlapped to a distance  $\delta$ . In such a case, we examine two points deep within the bodies, along the axis of contact, calling them  $T_1$  and  $T_2$ . These points will have moved  $\delta_1$  and  $\delta_2$ , respectively. The total overlap is obviously related to these displacements by  $\delta = \delta_1 + \delta_2$ .

However, under actual interaction, the two surfaces are going to deform as the load  $F$  presses them into contact. So now we consider two points on the surfaces, such as  $S_1$  and  $S_2$ . Before contact, these two points are initially separated by a distance  $h$  (from Eq. 5.2), then displace by  $\bar{u}_{z1}$  and  $\bar{u}_{z2}$  due to contact pressure.

If the points  $S_1$  and  $S_2$  are inside of the contact region under load, these distances are related by

$$\bar{u}_{z1} + \bar{u}_{z2} + h = \delta \quad (5.4)$$

Then using Eq. 5.2, we have an expression for the elastic displacements as

$$\bar{u}_{z1} + \bar{u}_{z2} = \delta - \frac{1}{2R^*} r^2 \quad (5.5)$$

Alternatively, if after deformation the points  $S_1$  and  $S_2$  are outside of the contact region, this is simply

$$\bar{u}_{z1} + \bar{u}_{z2} > \delta - \frac{1}{2R^*} r^2 \quad (5.6)$$

It now is necessary to find a pressure distribution that satisfies these boundary conditions of displacement. Hertz's great contribution was to simplify the solution of expressions Eqs. 5.5 and 5.6 by regarding each body as an elastic half-space upon which the load is applied over a small, elliptical region (the contact area). This simplification allows for treat-

ment of the highly concentrated stresses near the region of contact without consideration of either the general response of stresses in the bulk of the body or the manner in which they are supporting the load. This assumption is justifiable if the dimensions of each body as well as the relative radii of curvature are very large compared to the contact area. These assumptions are sufficient to proceed with the analysis, but the curious are pointed to an excellent discussion and background of Hertz's theory as given in KE Johnson's textbook.<sup>51</sup>

For solids of revolution, a distribution of pressure to satisfy the displacements of Eq. 5.6 is proposed by Hertz as

$$p = p_0 \left[ 1 - \left( \frac{r}{a} \right)^2 \right]^{1/2} \quad (5.7)$$

where  $a$  is the radius of the contact area.

The total load,  $F$  is found from the pressure distribution as

$$\begin{aligned} F &= \int_0^a p(r) 2\pi r \, dr \\ F &= \frac{2}{3} p_0 \pi a^2 \end{aligned} \quad (5.8)$$

From the distributed load over the circular region, stresses and deflections are found from superposition of point loads. The pressure is integrated (see Ref.<sup>51</sup>) to find the normal displacement for either solid body as

$$\bar{u}_z = \frac{1 - \nu^2}{E} \frac{\pi p_0}{4a} (2a^2 - r^2) \quad (5.9)$$

This is applied to both bodies and plugged into Eq. 5.5 to yield

$$\frac{\pi p_0}{4a E^*} (2a^2 - r^2) = \delta - \left( \frac{1}{2R^*} \right) r^2 \quad (5.10)$$

where we have introduced the now-common term of pair Young's modulus,

$$\frac{1}{E^*} = \frac{1 - \nu_1^2}{E_1} + \frac{1 - \nu_2^2}{E_2} \quad (5.11)$$

for simplification.

With the solution of Eq. 5.10, if we consider  $r = a$  and  $\delta(a) = 0$ , we find the radius of the contact circle is

$$a = \frac{\pi p_0 R^*}{2E^*} \quad (5.12)$$

and when  $r = 0$ , we find the overlap as

$$\delta = \frac{\pi a p_0}{2E^*} \quad (5.13)$$

and alternatively we find the pressure as a function of overlap

$$p_0 = \frac{2E^* \delta}{\pi a} \quad (5.14)$$

The radius, overlap, and pressure relations are inserted into Eq. 5.8 to find the force (from now on referred to as the Hertz force) as a function of overlap, relative radius, and pair Young's modulus,

$$F = \frac{4}{3} E^* \sqrt{R^*} \delta^{3/2} \quad (5.15)$$

as a last step, to differentiate the force from other terms to be derived later, we specify it as the normal force between sphere  $i$  and sphere  $j$  as

$$F_{n,ij} = \frac{4}{3} E_{ij}^* \sqrt{R_{ij}^*} \delta_{n,ij}^{3/2} \quad (5.16)$$

Equation 5.16 defines the normal contact forces between any two contacting, elastic spheres. This extremely important result acts as the basis of all discrete element method

codes since the concept was first introduced for granular materials by Cundall & Strack in 1979.<sup>23</sup>

It is very appealing to use the Hertz force in a numerical model such as DEM because there are very few assumptions built in to the theory; the material must be elastic and satisfy

$$\frac{a}{R^*} \ll 1 \quad (5.17)$$

In which case the force of Eq. 5.16 is calculated from material and geometric properties alone and no phenomenological, empirical fits are necessary.

# CHAPTER 6

## Momentum and Energy Transfer in Packed Beds

We review the momentum and exchange between a fluid moving through a porous medium and the drag force correlations that are used in engineering practice. Then we walk through the many modes of energy exchange between contacting particles and particles with an interstitial gas.

### 6.1 Pressure Drop Across Packed Beds

#### 6.1.1 Kozeny-Carman Correlation for Pressure Drop

P.C. Carman,<sup>14</sup> using Kozeny's Equation as a starting point, derived a formula for the average velocity of a laminar flow through a randomly packed beds at the close-packed limit,

$$U = \left( \frac{L}{L_e} \right)^2 \frac{\epsilon^3}{k_0 \mu S^2} \frac{\Delta p}{L} \quad (6.1)$$

where  $\mu$  is the viscosity, Carman called the tortuosity ( $L_e/L$ ) the ratio of the actual path of a streamline through the pore space,  $L_e$ , to the length of packing,  $L$ .  $S$  is the particle surface area per unit volume of the bed. For a bed of spheres this is  $S = 6(1 - \epsilon)/d_p$ . The fluid void fraction,  $\epsilon$  is obviously the complement to the packing fraction  $\epsilon = 1 - \phi$  that we have used throughout this work. The constant,  $k$ , varies between materials and packings but for regular spheres is found experimentally to be  $k \approx 5.0$ .  $\Delta p/L$  is the pressure drop per unit length of flow in the packed bed.

We rearrange Eq. 6.1 as

$$\frac{\Delta p}{L} = \frac{180U\mu}{d_p^2} \frac{(1-\epsilon)^2}{\epsilon^3} \quad (6.2)$$

The pressure gradient acting upon the fluid in the packed bed must be balanced by the drag force of all the particles in the bed. If we assume some average force,  $\langle f \rangle$ , as the ensemble average of the particle drag forces, we can write

$$\frac{\Delta p}{L} = n \langle f \rangle \quad (6.3)$$

where  $n$  is the number density of particles in the bed. We relate the number density in terms of the packing fraction as

$$n = \frac{6\phi}{\pi d_p^3} = \frac{6(1-\epsilon)}{\pi d_p^3} \quad (6.4)$$

Thus the average drag per particle in this flow is

$$\langle f \rangle = \frac{\Delta p}{L} \frac{\pi d_p^3}{6(1-\epsilon)} \quad (6.5)$$

We will non-dimensionalize the average drag force based on the classic Stokes force, drag force of a single particle in unbounded fluid,

$$F = \frac{\langle f \rangle}{3\pi\mu d_p U} \quad (6.6)$$

and when we plug in Eq. 6.5 to Eq. 6.6 we have

$$F_{kc} = \frac{\Delta p}{L} \frac{\pi d_p^3}{6(1-\epsilon)} \frac{1}{3\pi\mu d_p U} \quad (6.7)$$

which, with the substitution of the Kozeny-Carman pressure (Eq. 6.2), becomes

$$F_{kc} = \frac{180U\mu}{d_p^2} \frac{(1-\epsilon)^2}{\epsilon^3} \frac{\pi d_p^3}{6(1-\epsilon)} \frac{1}{3\pi\mu d_p U} \quad (6.8)$$

or simply

$$F_{kc} = 10 \frac{1 - \epsilon}{\epsilon^3} \quad (6.9)$$

Carman points out<sup>15</sup> the limitations of the Kozeny-Carman equation. Built into the equation is the assumption that the range of pore size and shape is fairly isotropic and similarly the tortuosity through the packed bed is relatively uniform. In the form we have used with Eq. 6.9, we have also assumed spherical particles in random packing near the close-packed limit ( $\phi \rightarrow 0.64$ ) with laminar flow at low Reynolds numbers. Carman provided modifications to cases of extremely high porosity and non-spherical, non-regular packings in his book from 1956.<sup>15</sup>

### 6.1.2 Ergun Correlation for Pressure Drop

Another correlation that is perhaps more commonly used in general is the Ergun equation.<sup>32</sup> Ergun's correlation is an empirical fit to a vast amount of experimental data. His pressure drop per length is

$$\frac{\Delta p}{L} = \frac{150U\mu}{d_p^2} \frac{(1 - \epsilon)^2}{\epsilon^3} + \frac{1.75\rho U^2}{d_p} \frac{1 - \epsilon}{\epsilon^3} \quad (6.10)$$

We non-dimensionalize the Ergun equation of Eq. 6.10 in the same form as Eq. 6.9 to find

$$F_e = 8.33 \frac{1 - \epsilon}{\epsilon^3} + 0.18 \frac{\text{Re}}{\epsilon^3} \quad (6.11)$$

where we see the Reynolds number dependence in the second term on the right side of Eq. 6.11. Comparing this to the non-dimensionalized drag force of the Kozeny-Carman relation (Eq. 6.9), we see that the first term on the right hand side is essentially the same but Ergun's equation underpredicts Stokes flow by roughly 20% (8.33 to 10.0). This is understandable as Ergun's equation was meant to fit a wide range of flow (finite-to-large

$\text{Re}$ ), including turbulent flow, whereas the Kozeny-Carman was meant specifically to apply to Stokes flow-type laminar packed beds.

### 6.1.3 Koch-Hill-Lad Correlation for Pressure Drop

Koch, Hill, & Ladd studied packed bed flow with high-precision lattice-Boltzmann simulations to develop correlations for drag in a packed bed over a wide range of packing fractions and Reynolds numbers.<sup>48,49,54</sup> They studied ordered arrays of spheres at various flow angles with dilute arrays (interstitial Reynolds number greater than particle Reynolds number), up to dense ordered arrays, and random arrays.

They consider the drag force as a sum of viscous and inertial stresses. Based on scaling arguments, the viscous and inertial contributions to  $F$  are expected to be independent of  $\text{Re}$  and linearly proportional to  $\text{Re}$ , respectively (in much the same form as Ergun's empirical fit of Eq. 6.11). Thus their numerical results were fit to the form

$$F = F_0(\phi) + F_3(\phi)\text{Re} \quad (6.12)$$

where

$$F_0 = \begin{cases} \frac{1+3(\phi/2)^{1/2}+(135/64)\phi \ln \phi + 16.14\phi}{1+0.681\phi - 8.48\phi^2 + 8.16\phi^3} & \text{if } \phi < 0.4 \\ 10.0 \frac{\phi}{(1-\phi)^3} & \text{if } \phi > 0.4 \end{cases} \quad (6.13)$$

and

$$F_3 = 0.0673 + 0.212\phi + 0.0232 \frac{1}{(1-\phi)^5} \quad (6.14)$$

Koch, Hill, & Ladd<sup>48</sup> compare their results with data from experiments. They found that at smaller Reynolds number and larger solid volume fractions, the rate of increase of drag force increases with the Reynolds number in much the same way predicted by Ergun's equation. However, at solid volume fractions smaller than those that can be achieved in

physical experiments, at the largest Reynolds numbers, the rate of drag force increase is significantly smaller than the value predicted by Ergun's equation.

For Stokes-flow (and near-Stokes-flow), the drag force computed from their lattice-Boltzmann simulations were indistinguishable from experimental data over all ranges of packing fractions achievable in controlled experiments. The correlation fit to their data for small Reynolds number and large packing fraction is simply the Kozeny-Carman relationship – which was itself generated with coefficients matching experimental data so it is no surprise their correlation fits that phase space of  $\phi$  – Re.

#### 6.1.4 Correlation Comparisons

We have given three correlations relating a non-dimensional drag force to packing fraction and Reynolds number. The first, the Kozeny-Carman equation, is applicable at small Reynolds number and broad range of packing fraction. The second, the Ergun equation, is applicable at a broad range of Reynolds number but is most accurate at higher packing fractions and also under-predicts drag at low Reynolds numbers. Finally, the third correlation by Koch, Hill, & Ladd (KHL), extended the drag correlations over a much more broad packing fraction and Reynolds numbers than is possible with physical experiments.

Here we simply provide a graphical comparison of the relationships that demonstrates when the classic correlations of Kozeny-Carman and Ergun match the correlation of KHL and when they diverge.

Later, in § 8, we will return to these correlations as we discuss the computational groundwork of the CFD-DEM coupling routine.

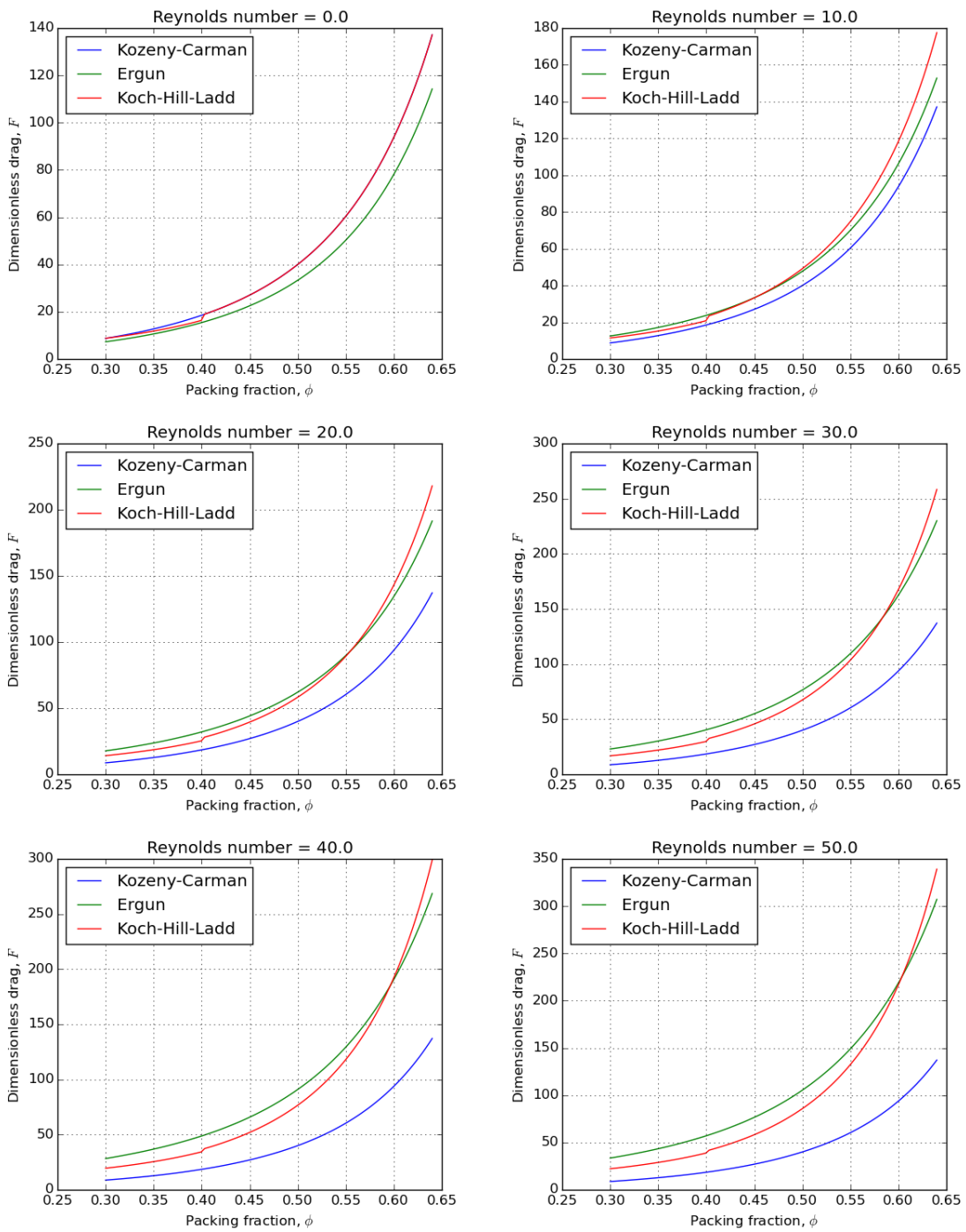


Figure 6.1: Comparison of pressure drop correlations over a range of packing fractions and Reynolds numbers.

## 6.2 Heat TranSpot in Packed Beds

In our analysis of the momentum of packed beds, we focused entirely on the exchange of momentum between a fluid passing through a packed bed. The mechanics of contacting particles will be dealt with entirely within the framework of the discrete element method, to be discussed in § 7. But now as we move to analyze the heat transfer in a packed bed, we will consider both inter-particle modes of heat transfer as well as particle-fluid convection.

Looking at the particle highlighted in Fig. 6.2, we see many pathways for heat to be transferred inside the ensemble. The most significant are:

1. Conduction through the contact area between contacting particles.
2. Conduction through the stagnant fluid between near, non-contacting particles.
3. Conduction through the stagnant fluid between contacting particles.
4. Advection of energy by the fluid to contacting- and downstream particles.
5. Radiation between the surfaces of contacting particles.
6. Radiation between particles of adjacent voids.
7. Heat generation internally in the particle.

We will address the inter-particle conduction in § 6.2.1 wherein we derive a formula for heat conductance between contacting, elastic spheres. The complex interaction of energy in a particle with a fluid (conduction through film regions, convection with passing fluid, etc.) will all be dealt with using correlations for packed beds; this is done in § 6.2.2. We will briefly discuss some literature where researchers have dealt with the radiation between particles in a packed bed but do not include the terms in our current models. Finally, the last mode of heat transfer is trivially accounted for with a heat source term,

$$Q_g = q'''V \quad (6.15)$$

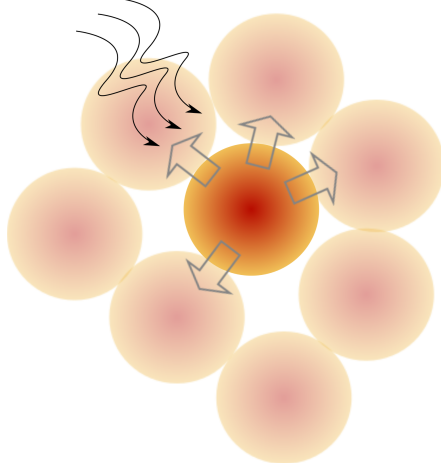


Figure 6.2: An illustration highlighting a single particle transferring energy into a passing fluid and neighboring particles in the ensemble.

where  $q''$  is a known volumetric heating rate and  $V$  is the volume of our particle. In practice, we will know a volumetric heating rate from the location and geometry of the solid breeder volume. The volume of the sphere is  $V = \frac{\pi}{6}d_p^3$ .

In the following sections we will expand upon the details of the modes of heat transfer considered for our packed beds. They forms of equations used will be written in a way as to be easily implemented directly into the DEM computational framework, to be discussed later in § 7.

### 6.2.1 Inter-particle Heat Conduction

When two particles come into contact, energy is transmitted through their region of contact. For this discussion, we assume the particles are spherical, elastic, in vacuum, and we neglect radiation transfer between them. If the two particles are at temperatures  $T_i$  and  $T_j$  we can quantify the amount of energy transferred between them with a commonly used practice of a contact conductance,  $H_c$ :

$$Q_{ij} = H_c(T_i - T_j) \quad (6.16)$$

The subscripts are omitted for clarity, but obviously there is a unique  $H_c$  per pair of

contacting particles. We note that the heat conductance, unlike standard heat transfer coefficients, has units of W/K.

Batchelor and O'Brien<sup>8</sup> developed a formulation of similar form and then made the brilliant observation that the temperature fields in the near-region of contacting spheres are analogous to the velocity potential of an incompressible, irrotational fluid passing from one reservoir to another through a circular hole in a planar wall separating the two reservoirs. With the analogy, they could make use of the fluid flow solution to write the total flux across the circle of contact just as Eq. 6.16 with the heat conductance as

$$H_c = 2k_r a \quad (6.17)$$

where  $k_r$  is the conductivity of the contacting solids and  $a$  is the radius of contact. In § 5, with Hertz theory we found the contact radius in terms of the contact pressure. Here, we give the radius in terms of the compression force acting on the bodies,

$$a = \left( \frac{3}{4} \frac{R^*}{E^*} \right)^{1/3} F_n^{1/3} \quad (6.18)$$

as before,  $\frac{1}{E^*} = \frac{1-\nu_1^2}{E_1} + \frac{1-\nu_2^2}{E_2}$  and  $\frac{1}{R^*} = \frac{1}{R_1} + \frac{1}{R_2}$ .

In the development of Eq. 6.17, Batchelor and O'Brien had assumed the two contacting spheres to be of equal conductivity,  $k_r$ . Cheng *et al.*<sup>20</sup> proposed a slightly modified conductance which allows for contacting materials of different thermal conductivity. They have,

$$H_c = 2k^* a = 2k^* \left( \frac{3}{4} \frac{R^*}{E^*} \right)^{1/3} F_n^{1/3} \quad (6.19)$$

where  $\frac{1}{k^*} = \frac{1}{k_i} + \frac{1}{k_j}$ . As well as being a more general, flexible formulation, the models analyzed by Cheng *et al.*<sup>20</sup> are in good agreement with experiments. In the DEM numerical structure, we use the form given by Eq. 6.19.

Furthermore, Batchelor and O'Brien developed Eq. 6.17 with the assumption of two contacting particles in vacuum but, once developed, showed<sup>8</sup> that this form is still valid when immersed in a fluid providing that the thermal conductivity ratio of solid and fluid is well above unity. The condition is expressed as,

$$\frac{k_r}{k_f} \frac{a}{R^*} \gg 1 \quad (6.20)$$

The term  $\frac{a}{R^*}$ , from § 5, is necessarily much less than 1 for Hertz theory to be applicable. Thus for fluid in vacuum, the condition is identically satisfied but we must consider inaccuracies if we introduce an interstitial fluid with low conductivity ratios; for lithium ceramics in helium, the ratio is approximately  $\frac{k_r}{k_f} \approx 10$ .

As we step back from the contact of a single pair of particles and consider a particle in an ensemble with many contacts, we must again consider the validity of applying Eq. 6.19 at each contact. Vargas and McCarthy,<sup>96</sup> proposed introducing a conduction Biot number to relate resistance to heat transfer internal to the particle with the resistance between particles. We use the following form

$$Bi_c = \frac{H_c}{k^* d_p} = 2 \frac{a}{d_p} \quad (6.21)$$

Then if  $Bi_c \ll 1$ , the individual energy transferred between each point of contact can be decoupled. The Biot number criteria is already satisfied for Hertz theory to be valid; having assumed that  $\frac{a}{d_p} \ll 1$ . Therefore the total heat transferred out of a single particle with  $Z$  contacts is the summed contribution of individual contacts,

$$Q_i = \sum_j^Z Q_{ij} \quad (6.22)$$

The contact conductance we use, Eq. 6.19, which is built upon the solution of Batchelor and O'Brien,<sup>8</sup> has been implemented by others in a variety of studies.<sup>17, 20, 95, 109</sup> However, in many other fields, the researchers are interested in such things as the parallel conduction

through a stagnant interstitial gas<sup>11</sup> or the temporary conduction during impact of fluidized beds.<sup>58,98,104,111</sup> In such cases, the formula for conductance can be quite different but are not appropriate for the physics of our packed beds.

### 6.2.2 Nusselt Number for Spheres in Packed Beds

Historically, in the treatment of packed beds for heat transfer, engineers developed relationships between overall heat transfer coefficients to the log-mean temperature of the bed. The Nusselt number correlation was applicable to the bed overall rather than any discrete particle inside of the bed. The correlations will be useful for validating our models of helium flow through packed beds of lithium ceramics.

Recently, however, experimental and numerical research has focused on the heat transfer at the scale of a particle as a component of dilute or dense packed beds. These correlations will be useful for applying to single discrete elements in our DEM framework.

$$Q_{\text{convection}} = -hA_r(T_r - T_f) \quad (6.23)$$

where  $T_r$  is the temperature of the solid with surface area,  $A_r$ , and  $T_f$  is the local bulk temperature of the passing fluid.

#### 6.2.2.1 Van Lew

In their analysis of solar thermal storage devices, Van Lew *et al.* derived a form of heat transfer coefficient based on the Chilton-Colburn analogy.<sup>92</sup> The form of their solution followed from the form used by Nellis and Klein<sup>68</sup> in heat exchangers. The heat transfer coefficient used by Van Lew *et al.* reads

$$\text{Nu} = 0.191N_v Re_G^{-0.278} Pr_f^{-2/3} \quad (6.24)$$

where the dimensionless grouping  $N_v = \frac{\dot{m}D_h c_f}{\epsilon A_t k_f}$  and they used a modified Reynolds number based on the mass flux and hydraulic diameter of their storage tank,

$$Re_G = \frac{4\dot{m}r_{char}}{\epsilon\pi R_t^2 \mu_f} \quad (6.25)$$

where  $R_t$  is the radius of the storage tank and with  $r_{char}$  a characteristic radius (or hydraulic radius) of their packing,

$$r_{char} = \frac{\epsilon d_p}{4(1-\epsilon)} \quad (6.26)$$

and  $d_p$  is the nominal diameter of filler material.

While the simulations of thermoclines run by Van Lew *et al.* predicted well the results of their experimental data<sup>90,92</sup> their correlation for heat transfer coefficient does not match theory as  $Re \rightarrow 0$ . In a stationary fluid,  $Nu = 2$  but in the correlation of Eq. 6.24, as  $Re \rightarrow 0$ ,  $Nu \rightarrow 0$  and thus is not appropriate for the low-Reynolds flows inside the solid breeder volume.

Wakao provides

$$Nu = 2 + 1.1Re_p^{0.6}\Pr^{1/3} \quad (6.27)$$

Li & Mason provide a correlation

$$Nu = \begin{cases} 2 + 0.6\epsilon^n Re_p^{1/2} \Pr^{1/3} & Re_p < 200 \\ 2 + 0.5\epsilon^n Re_p^{1/2} \Pr^{1/3} + 0.02\epsilon^n Re_p^{0.8} \Pr^{1/3} & 200 < Re_p < 1500 \\ 2 + 0.000045\epsilon^n Re_p^{1/2} & Re_p > 1500 \end{cases} \quad (6.28)$$

where they found from experiments that  $n = 3.5$  was appropriate for 3 mm polymer pellets in dilute flows (small  $\phi$ ). The coefficient needs to be evaluated experimentally for configurations of other particle sizes, packing fractions, or Reynolds numbers.<sup>58</sup>

There are a few other correlations in literature for the Nusselt number. But they are not given as they are either well out of the operation space of our parameters; Bandrowski &

Kaczmarzyk,<sup>7</sup> that is only for extremely dilute flow at high Reynolds number ( $180 < \text{Re}_p < 1800$  and  $0.00025 < \phi < 0.05$ ).

### 6.2.3 Radiative Transfer with Neighboring Particles

The temperatures expected in the solid breeder are high enough that we can not a priori neglect radiation. The radiation exchange between contacting neighbors in a packed bed becomes extremely complex due to the local and semi-local nature of radiation. A standard approach to treat radiation exchange between surfaces is to consider the view factor between them. In a dense, randomly packed bed of spheres the computation of view factors between pebbles can be done via a method such as that proposed Feng and Han.<sup>34</sup> Ideally, we could show this mode of heat transport is negligible compared to the others already discussed.

In ceramic breeder designs, the tritium breeding volume is rarely more than 2cm wide with pebbles that are, generally, 1mm in diameter. The maximum expected temperature in the breeding zone is about 1000K, roughly at the centerline of the 2cm width. The walls of the coolant must be held below the operable steel temperature of roughly 700K. This works out to a 300K differences spanning 10 pebble diameters. From this we can make a first-order approximation of 30K difference between neighboring pebbles. At the elevated temperatures, an estimate for the radiation exchange between two pebbles (allowing them to act as black bodies for this approximation) is

$$\dot{Q}_{\text{radiation}} = \sigma A (T_{\max}^4 - (T_{\max} - 30)^4) \approx 0.022 \text{W} \quad (6.29)$$

which is the highest amount of radiation exchange we might expect between pebbles. Even though we will neglect this mode of heat transfer for now, after reviewing some of the packed bed heat transfer results we may find that this quantity of energy transfer is not negligible and future versions of the model would have to account for it.

**Part III**

**Development of Modeling Tools for  
Pebble Bed Morphological Evolution  
Study**

# CHAPTER 7

## Development of DEM Modeling Tools for Ceramic Solid Breeders

This chapter presents the motivations and background of this study. First, it discusses energy usage in our society and the inevitable production of waste mechanical and thermal energies and their ubiquitous nature. This is followed by a brief discussion of common methods of converting ambient mechanical energy and waste heat into useful electrical energy. This chapter concludes with the objectives of this study and the scope of the document.

### 7.1 Background

The observable, macroscopic behavior of particulate, or granular, systems is a complex function of the multitude of particle-scale interactions. Historically, empirical relationships have been used to describe these systems as if a continuous media. But with the advent of the discrete element method by Cundall and Strack<sup>23</sup> and the acceleration of computing power, it became practical to investigate these particulate systems at the particle scale. With the discrete element method, we track all the particles in the system in a Lagrangian manner. In the ensemble, the kinematics of each particle is tracked and updated based on balances (or imbalances) of forces or energy acting upon the particle.

Experiments on packed beds are generally limited to measurements of statistically averaged, macroscopic responses. Unlike continuous materials, packed beds as yet can not be described by any State. For instance, with an ideal gas if we know two properties such as temperature or pressure, the State of the gas is known and its behavior predicted. Two

packed beds with the same temperature, packing fraction, average particle diameter, and stress state may react wildly different. As researchers we create empirical fits to data on the particular packed bed under investigation but then might have to dubiously apply the relationships to beds of different packing states.

DEM is emerging as a reliable method to remove speculation about the internal state of the packed bed as the simulations provide valuable information on the dynamics of particle interactions and how they relate to the macroscopic responses that are measured experimentally.

In this chapter we will lay out the formulas governing interaction of particles in the DEM framework, the methods of computation, and the code used for implementation. In § 11.4, we will use the derivation of the Hertz contact law described in § 5 to argue for a technique of accelerating the computational time without loss of physics via proper scaling of physical parameters. Lastly, in § 12.1, we use our DEM tools to investigate the thermo physics of representative packed beds for solid breeders in fusion reactors.

## 7.2 Particle Dynamics

The particles in our system are allowed translational and rotational degrees of freedom. In a packed bed, we can restrict our attention to local forces between particles; neglecting, say, non-contact forces such as van der Waals or electrostatic forces. In the first construct, we will treat the particles as if in a vacuum and leave a derivation of fluid interaction forces for § 8.

### 7.2.1 Particle Kinematics

Assuming we know the contact forces acting upon particle  $i$ , Newton's equations of motion describe the motion of the particle. The translational and rotational for the translation degrees of freedom:

$$m_i \frac{d^2 \mathbf{r}_i}{dt^2} = m_i \mathbf{g} + \mathbf{f}_i \quad (7.1a)$$

$$I_i \frac{d\omega_i}{dt} = \mathbf{T}_i \quad (7.1b)$$

where  $m_i$  is the mass of this particle,  $\mathbf{r}_i$  its location in space,  $\mathbf{g}$  is gravity,  $I_i$  is the particle's moment of inertia, and  $\omega_i$  its angular velocity.

The net contact force,  $\mathbf{f}_i$ , represents the sum of the normal and tangential forces from the total number of contacts,  $Z$ , acting on this particle.

$$\mathbf{f}_i = \sum_{j=1}^Z \mathbf{f}_{n,ij} + \mathbf{f}_{t,ij} \quad (7.2)$$

and the net torque,  $\mathbf{T}_i$ , is similarly,

$$\mathbf{T}_i = -\frac{1}{2} \sum_{j=1}^Z \mathbf{r}_{ij} \times \mathbf{f}_{t,ij} \quad (7.3)$$

### 7.2.2 Linear Spring-Dashpot Model

When Cundall and Strack first proposed the discrete element method, they used a linear spring-dashpot structure which saw the normal and tangential forces written as,

$$\mathbf{f}_{n,ij} = k_{n,ij} \delta_{n,ij} \mathbf{n}_{ij} - \gamma_{n,ij} \mathbf{u}_{n,ij} \quad (7.4a)$$

$$\mathbf{f}_{t,ij} = k_{t,ij} \delta_{t,ij} \mathbf{t}_{ij} - \gamma_{t,ij} \mathbf{u}_{t,ij} \quad (7.4b)$$

The fictive tangential overlap,  $\delta_{t,ij}$ , is truncated to so the tangential and normal forces obey Coulomb's Law,  $\mathbf{f}_{t,ij} \leq \mu_i \mathbf{f}_{n,ij}$  with  $\mu$  as the coefficient of friction of the particle. In the first model of Cundall and Strack, the stiffness coefficients  $k$  were constants and the local damping coefficients  $\gamma$  were proportional to them,  $\gamma \propto k$  to allow dissipation of energy

and the system to reach an equilibrium. The relative normal and tangential velocities, respectively, are decomposed from the particle velocities,

$$\mathbf{u}_{n,ij} = (-(\mathbf{u}_i - \mathbf{u}_j) \cdot \mathbf{n}_{ij}) \mathbf{n}_{ij} \quad (7.5a)$$

$$\mathbf{u}_{t,ij} = (-(\mathbf{u}_i - \mathbf{u}_j) \cdot \mathbf{t}_{ij}) \mathbf{t}_{ij} \quad (7.5b)$$

with the unit vector  $\mathbf{n}_{ij}$  pointing from particle  $j$  to  $i$

Similarly to the approach of Hertz (see § 5), the surfaces of the two particles are allowed to virtually pass through each other (no deformation) resulting in normal and tangential overlaps of,

$$\delta_{n,ij} = (R_i + R_j) - (\mathbf{r}_i - \mathbf{r}_j) \cdot \mathbf{n}_{ij} \quad (7.6a)$$

$$\delta_{t,ij} = \int_{t_{c,0}}^t \mathbf{u}_{t,ij} d\tau \quad (7.6b)$$

We have a relatively simple approach of calculating the interaction forces between particles with Eq. 7.4 based on the kinematics of velocity and position of the interacting particles from Eq. 7.5 and Eq. 7.6, respectively. As the DEM evolved and drew the attention of more researchers, more complex formulas governing the forces of Eq. 7.4 emerged. But the core approach remained the same and the models all fall into the same family of so-called ‘soft particle’ models of DEM. A well-composed summary of the different DEM force models is given by Zhu *et al.*<sup>110</sup>

The method used in our work is fit into the computational skeleton of Cundall and Strack’s method but with non-linear spring-dashpot coefficients defined by simplified Hertz-Mindlin-Deresiewicz model; the details will be expressed in the next section.

### 7.2.3 Hertzian Non-Linear Spring Dashpot Model

The normal-direction (Hertz) stiffness coefficient of Eq. 7.4a is based on the Hertzian contact laws given in § 5. The tangential-direction (Mindlin) stiffness coefficient follows from Brilliantov,<sup>10, 57, 110</sup>

$$k_{n,ij} = \frac{4}{3} E_{ij}^* \sqrt{R_{ij}^* \delta_{n,ij}} \quad (7.7a)$$

$$k_{t,ij} = 8G_{ij}^* \sqrt{R_{ij}^* \delta_{t,ij}} \quad (7.7b)$$

with  $G_{ij}^*$  as the pair bulk modulus,

$$\frac{1}{G_{ij}^*} = \frac{2(2 + \nu_i)}{E_i} + \frac{2(2 + \nu_j)}{E_j} \quad (7.8)$$

The damping coefficients,  $\gamma$ , arise to account for the energy dissipated from the collision of two particles.<sup>29, 88, 89</sup> Whether the damping coefficient is local or global and the exact form of the coefficient is more important for loosely confined granular systems and dictates the way the system approaches an equilibrium state.<sup>63</sup> For the case of our tightly packed pebble beds, it suffices to use the efficient form of,<sup>10, 63, 81, 103, 110</sup>

$$\gamma_n = \sqrt{5\beta_{\text{diss}} m^* k_{n,ij}} \quad (7.9a)$$

$$\gamma_t = \sqrt{\frac{10}{3}\beta_{\text{damp}} k_{t,ij} m^*} \quad (7.9b)$$

with  $\beta_{\text{damp}}$  as the damping ratio, and the pair mass,  $\frac{1}{m^*} = \frac{1}{m_i} + \frac{1}{m_j}$ . For a stable system with  $\beta_{\text{damp}} < 1$ , the damping ratio is related to the coefficient of restitution,  $e$ ,

$$\beta_{\text{diss}} = -\frac{\ln e}{\sqrt{\ln^2 e + \pi^2}} \quad (7.10)$$

### 7.2.4 Time Integration

Having expressed the contact mechanics of the discrete element method, we now need a means of integrating the kinematics of the particles. The most common means of marching in time with DEM is the velocity-Verlet algorithm.<sup>55</sup> In this algorithm we integrate Eqs. 7.1 with half-steps in velocity, full steps in position, and then finally the complete step in velocity (the two half-steps in velocity are often compressed into a single, full step, as we will do below). Here we will explicitly show the integration for the translational degrees of freedom.

The force field defined by Eq. 7.1a is rewritten in terms of the acceleration of the particle. For clarity in expression, the per-particle subscripts ( $i$ ,  $j$ , etc.) will be temporarily omitted. Instead, time-varying quantities will have a subscript to refer to their temporal location. Quantities measured or evaluated at the current timestep will have subscript  $t$  (note this does not refer to tangential directions!). Eq. 7.1a is rewritten as

$$\mathbf{a}_t = \mathbf{g} + \frac{\mathbf{f}_t}{m} \quad (7.11)$$

The first step in the velocity-Verlet algorithm is to integrate the position of the particle by a full timestep based on the current timestep's velocity and acceleration. Note that the initial condition of the particle must specify both position and velocity for this step to be evaluated at the start, from then on the velocity is explicitly updated.

$$\mathbf{r}_{t+\Delta t} = \mathbf{r}_t + \mathbf{v}_t \Delta t + \frac{1}{2} \mathbf{a}_t \Delta t^2 \quad (7.12)$$

The particles at new positions interact as a function of their overlaps (see Eqs. 7.4). Acceleration at the full timestep is then calculated from the updated forces (of Eq. 7.11). In the last computational step, the velocity at the full timestep is found from an average acceleration,

$$\mathbf{v}_{t+\Delta t} = \mathbf{v}_t + \frac{\mathbf{a}_t + \mathbf{a}_{t+\Delta t}}{2} \Delta t \quad (7.13)$$

The velocity-Verlet algorithm is an efficient means of explicitly integrating the kinematic equations for all the particles in the ensemble. The algorithm is stable with a global error of approximately  $O(\Delta t^2)$  for displacement.<sup>46</sup> But, as an explicit method, the size of the timestep must be carefully chosen to avoid instabilities in the system. Stable, critical timesteps and means of circumventing unreasonably small timesteps will be addressed in § 11.4. Additionally, we have contended with the Lagrangian tracking of the particles momentum but we have still to deal with energy transfer through the packed beds which is just as important for our packed beds of ceramic breeder material. The heat transfer will be tackled in § 7.3.

In our work, we occasionally required a fully quiesced bed. To determine when this occurred, the total kinetic energy of the entire ensemble was monitored and a packed bed was considered to have completely settled once the kinetic energy of the system was less than  $10^{-9}$ ; similar to the process described in Ref.<sup>83</sup>

### 7.3 Granular Heat Transfer

In an analogous way we handled the momentum of every particle in DEM with Newton's laws of motion, the Lagrangian tracking of energy of each particle is obtained via the first law of thermodynamics. We treat each particle as a single distinct object and thus do not consider any internal temperature gradients (a point which we alluded to in § 11.2). The temperature of particle  $i$  is governed by

$$\rho_i V_i C_i \frac{dT_i}{dt} = Q_{s,i} + Q_i \quad (7.14)$$

where  $\rho$ ,  $V$ , and  $C$  are the density, volume, and the specific heat of the solid, respectively. Heat generation inside the particle is input with  $Q_s$  and the total heat transferred to/from particle  $i$  via conduction to all,  $Z$ , neighboring particles,

$$Q_i = \sum_{j=1}^Z Q_{ij} \quad (7.15)$$

The conductive heat transfer to neighboring particles comes from the inter-particle conduction formulas we derived in § 6.2.1, given in Eq. 6.16 with conductance of Eq. 6.19. They are repeated here for reference,

$$Q_{ij} = H_c(T_i - T_j)$$

and

$$H_c = 2k^* \left[ \frac{3F_{n,ij}R^*}{4E^*} \right]^{1/3} \quad (7.16)$$

### 7.3.1 Thermal Expansion

The stresses predicted to act upon the solid breeder volume during operation of the fusion reactor arise from the differential rate of thermal expansion from the highly heated ceramic volume and the relatively cool structural container. Moreover, thermal creep motion is observed in pebble beds<sup>19,30,86,97</sup> and is behavior we must capture in our model. Both of those phenomena can be traced to the thermal expansion of individual particles in the ensemble. Therefore, we introduce a thermal expansion formula that updates the diameter of each particle after a chosen amount of timesteps,

$$d_i = d_{0,i} [1 + \beta_i (T_i - T_{\text{ref}})] \quad (7.17)$$

where  $\beta_i$  is the thermal expansion coefficient (in units of 1/K),  $T_i$  is the temperature of the pebble at the current step, and  $d_{0,i}$  is the diameter of the pebble at temperature  $T_{\text{ref}}$ .

## 7.4 DEM solver

### 7.4.1 Numerical Implementation Overview

The primary computational tools used in this study is LAMMPS (Large-scale Atomic/Molecular Massively Parallel Simulator);<sup>71</sup> a classical molecular dynamics code. The package of code, maintained by Sandia National Labs (<http://lammps.sandia.gov>), has many features making it particularly attractive for our use on the simulation of pebble beds. LAMMPS is open-source and written in highly-portable C++ allowing customization of any feature used in modeling. LAMMPS runs with distributed-memory message-passing parallelism (MPI) and provides simple control (manual or automatic) of the spatial-decomposition of simulation domains for parallelizing. Perhaps most importantly, LAMMPS provides an efficient method for detecting and calculating pair-wise interaction forces; the largest consumer of run-time in the DEM algorithm.<sup>71</sup> We build the code as a library so that LAMMPS can be coupled to other numerical tools; we use the scripting language of Python (Python 2.7) as an umbrella code to call LAMMPS routines with the full availability of Python libraries.

LAMMPS by default provides a rudimentary method of modeling of granular particles (the term ‘granular’ here differentiates the ‘discrete element’ of molecules or atoms from larger-scale granular particles of powders or pebbles); LAMMPS has been used for studying granular material since at least 2001 when Silbert *et al.*<sup>84</sup> studied granular flow on inclined planes. However, the usefulness of LAMMPS for studying granular systems was greatly enhanced by LIGGGHTS (LAMMPS Improved for General Granular and Granular Heat Transfer Simulations), a suite of modules included on top of LAMMPS. LIGGGHTS has many academic and industrial contributors from around the world, with the code maintained as open-source by DCS Computing, GmbH.

Briefly, some notable features the LIGGGHTS code brings to the LAMMPS environment include: Hertz/Hooke pair styles with shear history, mesh import for handling wall geometry, moving meshes, stress analysis of imported meshes, a macroscopic cohesion model, a heat transfer model, and improved dynamic load balancing of particles on processors.<sup>52,53</sup> Both

LIGGGHTS and LAMMPS are distributed under the open-source codes under terms of the Gnu General Public License.

We will review some of the important physical models used in LAMMPS/LIGGGHTS as they relate to the important features we wish to investigate for packed beds of pebbles in fusion reactors.

# CHAPTER 8

## Development of CFD-DEM Modeling Tools for Ceramic Solid Breeders

[talk about how lacking the DEM result is without the inclusion of helium in analysis. There are some Fusion papers on conductivity in vacuum and with helium]

We now consider the influence of helium on thermal transport of deposited nuclear energy as it is carried away by the cooled structural walls. We begin by considering the fluid in a continuum sense and the pebbles in a discrete one. The interactions of the fluid and solid are characterized by effective relationships in each discretized cell of fluid. We then consider an mesoscopic approach to the fluid-solid interaction with the Lattice-Boltzmann method.

The chapter begins with introduction of the coupled fluid dynamics - discrete element method (CFD-DEM) approach: governing equations, discretization techniques, and algorithms.

We then do LBM. And stuff.

### 8.1 Numerical Methodology

Models based on the discrete element method (DEM) are currently the only tools available that can extract information on individual pebble interactions. The DEM formulation provides information such as inter-particle forces and individual particle temperatures, which are necessary for predicting and simulating morphological changes in the bed (e.g. pebble cracking, sintering, etc.) However DEM alone is not able to capture the effects, neither on momentum nor energy, of an interstitial fluid. Therefore we present two fluid modeling

techniques to supplement the DEM computations. We will first discuss the fully dynamic coupling of the DEM model with a volume-averaged thermofluid model of helium. Then we will introduce the integration of our DEM packing structure into lattice-Boltzmann simulations of the entire bed-fluid system.

### 8.1.1 DEM

The discrete element framework introduced in § 7.2 is augmented with a drag force term to capture interaction with surrounding fluid velocity fields. To accomplish this, we simply include a drag force to the Newtonian balance of forces given in Eq. 7.1. The momentum balance now reads:

$$m_i \frac{d^2 \mathbf{r}_i}{dt^2} = m_i \mathbf{g} + \mathbf{f}_i + \beta_i V_i \Delta u_{if} \quad (8.1)$$

where  $\Delta u_{if} = u_f - u_i$ , is the relative velocity between the fluid and pebble,  $i$ , and the inter-phase momentum exchange coefficient,  $\beta_i$ , acts upon the pebble volume (not to be confused with the damping coefficient introduced in § 7.2). Similarly, the energy equation now includes

$$m_i C_i \frac{d^2 T_i}{dt^2} = Q_{n,i} + \sum_{j=1}^Z Q_{ij} + \beta_{E,I} A_i \Delta T_{if} \quad (8.2)$$

where  $\Delta T_{if} = T_f - T_i$ , is the relative temperature between the fluid and pebble,  $i$ , and the inter-phase energy exchange coefficient,  $\beta_{E,i}$ , acts upon the pebble surface area,  $A_i$ .

The trajectory of pebble  $i$  is updated based on the force terms on the right hand side of Eq. 8.1: gravity, contact forces between particles (or particle-wall), and a drag force. Similarly, the temperature of the particle updates with the terms from Eq. 8.2: nuclear heating rate, inter-particle conduction, and now a heat transfer with surrounding fluid.

Drag forces from fluid flows through packed beds are found from volume-averaged, empirical correlations of either numerical or experimental studies. Considering a small region

of a packed bed surrounding our particle of interest,  $i$ , the nondimensional drag force is found only as a function of the local packing fraction of that region. In the zero Reynolds number limit, the nondimensional drag force reduces to a Stokes flow correlation that is only a function of the local packing fraction value,  $\phi$ . For the value of particle Reynolds numbers seen by the helium purge gas, this is the dominant term. However, for a complete discussion of the nondimensional drag terms see Refs. 5, 6. The correlation used in this study comes from the results of numerical studies of packed beds by Koch and Hill.<sup>9,45,54</sup> To arrive at their relationships, they did many lattice-Boltzmann simulations of porous flow.

$$\beta_i = \frac{18\nu_f\rho_f}{d_i^2}(1 - \phi)F \quad (8.3)$$

where

$$F = \epsilon(F_0 + \frac{1}{2}F_3\text{Re}_{p,i}) \quad (8.4)$$

Stokes flow

$$F_0 = \begin{cases} \frac{1+3\sqrt{\phi/2}+(135/64)\phi\ln(\phi)+17.14\phi}{1+0.681\phi-8.48\phi^2+8.16\phi^3} & \text{if } \phi < 0.4 \\ 10\frac{\phi}{(1-\phi)^3} & \phi > 0.4 \end{cases} \quad (8.5)$$

and high Reynolds contribution

$$F_3 = 0.0673 + 0.212\phi + \frac{0.0232}{(1 - \phi)^5} \quad (8.6)$$

The packing fraction and void fraction in any fluid cell is calculated by summing through all the volumes of  $k$  particles located in that cell (or the complement thereof)

$$\phi = \sum_{i=1}^k \frac{V_{p,i}}{\Delta V_f} \quad (8.7)$$

Other forces, such as Magnus forces, are inconsequential on predominantly stationary packed beds and are not considered.

The inter-phase energy transfer coefficient is of the same form as a traditional heat transfer coefficient and is calculated from the Nusselt number for the helium flow (with conductivity  $k_f$ ) through a packed bed.

$$\beta_{E,i} = \frac{\text{Nu}_i k_f}{d_i} \quad (8.8)$$

Li and Mason<sup>58</sup> summarize correlations for Nusselt number as a function of Reynolds number for packed beds with the following equations

$$\text{Nu} = \begin{cases} 2 + 0.6(1 - \phi)^n \text{Re}_p^{1/2} \text{Pr}^{1/3} & \text{Re}_p < 200 \\ 2 + 0.5(1 - \phi)^n \text{Re}_p^{1/2} \text{Pr}^{1/3} + 0.2(1 - \phi)^n \text{Re}_p^{4/5} \text{Pr}^{1/3} & 200 < \text{Re}_p \leq 1500 \\ 2 + 0.000045(1 - \phi)^n \text{Re}_p^{9/5} & \text{Re}_p > 1500 \end{cases}$$

where  $n = 3.5$  was found to fit best for small particles in dilute flows. [we should find a new value for high packing fraction]

Thus we have a formulation whereby a known fluid flow field and temperature throughout the domain, we can calculate the influence of that fluid on every particle's position and temperature. Next we will cover how we can calculate the flow field based on a volume-averaged influence of particles on the fluid.

### 8.1.2 Volume-averaged CFD Helium

The technique of coupling CFD to DEM was first proposed by Tsuji *et al.*. In this formulation of the helium flow, a fluid cell is much larger than the individual particles (in application, this meant approx. 5-6 particles per cell) and as such, the particles themselves are not resolved in the fluid space but are simply introduced via volume-averaged terms. Therefore momentum and energy of a fluid flow through a solid phase is governed by volume-averaged Navier-Stokes and energy equations<sup>10</sup>. These equations are applied to a discretized volume

of fluid space. For fluid cell, k, these are5:

$$\frac{\partial \epsilon_k \rho_f}{\partial t} + \nabla \cdot (\epsilon_k u_f \rho_f) = 0 \quad (8.9a)$$

$$\frac{\partial \epsilon_k u_f}{\partial t} + \nabla \cdot (\epsilon_k u_f u_f) = -\frac{\epsilon_k}{\rho_f} \nabla P_f + \nabla \cdot (\nu_f \epsilon_k \nabla u_f) - \frac{S_k}{\rho_f} \quad (8.9b)$$

$$\frac{\partial \epsilon_k T_f}{\partial t} + \nabla \cdot (\epsilon_k u_f T_f) = \nabla (\epsilon_k \epsilon \nabla T_f) - \frac{E_k}{\rho_f C_f} \quad (8.9c)$$

where the fluid void fraction is the complement of the solid packing fraction,  $\epsilon = 1 - \phi$ . The momentum and energy exchanges with the solid phase are represented in the source terms. They are volume-weighted sums of the drag forces and energy exchanges, respectively, for all particles in the discretized fluid cell:

$$S_k = \frac{1}{V_k} \sum_{\forall i \in k} \beta_i V_i \Delta u_{if} \quad (8.10a)$$

$$E_k = \frac{1}{V_k} \sum_{\forall i \in k} \beta_{E,i} A_i \Delta T_{if} \quad (8.10b)$$

The inter-phase momentum and energy exchange coefficients act as the communicators between the particle information from the DEM solver and the fluid fields from CFD. Thus the motion and energy of the fluid field are intimately coupled with the particle positions and energy, but computational time is preserved by only considering volume-averaged values in the fluid domain. The cross-communication between fluid and solid is accomplished with a coupling routine that is explained in detail in Refs. 11, 12.

### 8.1.3 Modeling Setup and Procedure

The pebble bed has dimensions in the x-y directions of  $20d \times 15d$ , respectively. There are structural walls, providing cooling, at the x-limits and periodic walls in the y-limits. 10 000 pebbles were loaded into the system which went to a height of approximately  $24d$  after the bed was vibration packed. The pebble bed had a roof loaded at the upper limit of the

*z*-direction that was lowered by force-control up to 6 MPa. This bed is referred to as the ‘well-packed’ bed. This was meant to simulate a fresh, densely-packed bed that is under compressive load during fusion operation. As such, this would be when pebbles would be likely to crack during operation. Therefore, based on the well-packed bed, a second bed was generated by simulating crushed pebbles; crudely the extensive crushing is simulated by simply removing 10% of the pebbles at random from the ensemble and then allowing the bed to resettle, from the now-imbalanced gravity and inter-particle forces, to a new stable packing structure. This bed is then referred to as the ‘resettled’ bed for the rest of the analysis. The intent is to deduce changes in thermo-mechanical properties from an ideally packed bed to one where significant cracking has altered the ideal morphology of the bed.

## **CHAPTER 9**

### **Development of lattice-Boltzmann Modeling Tools for Ceramic Solid Breeders**

# CHAPTER 10

## Background Experimental Studies

Many experiments were carried out on individual ceramic pebbles. While there are some measures from experiments that are immediately useful for qualitative comparisons, such as the crush strength between different batches of ceramics, most values are not obviously connected to analysis of the pebbles nor the pebble bed assemblies they make up. In this section we will show how careful examination of single pebble experiments can lead to predictions of not only strength in ensembles but also modifications of the fundamental properties of the ceramic pebbles.

In section § 10.1, we use single pebble experiments to validate the use of Hertz theory for contacting ceramic pebbles, but also determine the proper Young's modulus to use for the ceramics. In section § 10.2 we use the theory along with experimental data to begin to make predictions for survivability of pebbles in ensembles.

### 10.1 Elasticity Reduction Factor

We introduced Hertz theory in § 5, and in § 7 showed how we apply the Hertzian contact rules into the discrete element computational framework. We will revisit the Hertzian equations as we analyze the force-displacement measurements of single pebbles in the anvils of our uniaxial compression test stand.

The derivation to the Hertz force can be found on page 48 but the result is given again here for reference:

$$F_{n,ij} = \frac{4}{3} E_{ij}^* \sqrt{R_{ij}^*} \delta_{n,ij}^{3/2}$$

and, again, the pair Young's modulus and radius are

$$\frac{1}{E^*} = \frac{1 - \nu_i^2}{E_i} + \frac{1 - \nu_j^2}{E_j}$$

$$\frac{1}{R^*} = \frac{1}{R_i} + \frac{1}{R_j}$$

In experiments where we press a ceramic pebble between two platens, we measure the travel,  $s$ , rather than the pebble overlap, so we modify Eq. 5.16 to be represented in terms of travel ( $s = 2\delta$ ). Furthermore, for a pebble ( $R_i = R_p$ ) in contact with a smooth plane ( $R_j \rightarrow \infty$ ), the relative radius is simply  $R^* = R_p = d_p/2$ . We write the Young's modulus of the pebble as  $E_p$  and for the test stand's anvil as  $E_s$ ; similarly for the Poisson ratios of the two materials. The Hertz force for a pebble between anvils is then

$$F = \left[ \frac{1}{3} \frac{\sqrt{d_p}}{\frac{1-\nu_p^2}{E_p} + \frac{1-\nu_s^2}{E_s}} \right] s^{3/2} \quad (10.1)$$

The Young's modulus and Poisson ratio of the test stand are known values that do not vary between pebble experiments. Similarly, in the application of Hertz theory, we also assume the Young's modulus and Poisson ratio of the ceramic is also a known, constant value. In that case, for any given pebble diameter, the term inside [] is composed of entirely of constants for any given pebble; there is therefore a single force-travel response possible based on  $s$ . Using the material properties given in Ref.<sup>43</sup> for  $\text{Li}_2\text{TiO}_3$ , we plot a set of parametric curves based on diameter over a range of travel. The properties we have used for the nickel-alloy anvil of our test stand and  $\text{Li}_2\text{TiO}_3$  are given in Table 10.1. The curves are given in Fig. 10.1.

Table 10.1: Material properties used for  $\text{Li}_2\text{TiO}_3$  and nickel-alloy platen

$E_{\text{peb}}$	$\nu_{\text{peb}}$	$E_{\text{stand}}$	$\nu_{\text{stand}}$
(GPa)		(GPa)	
126	0.24	220	0.27

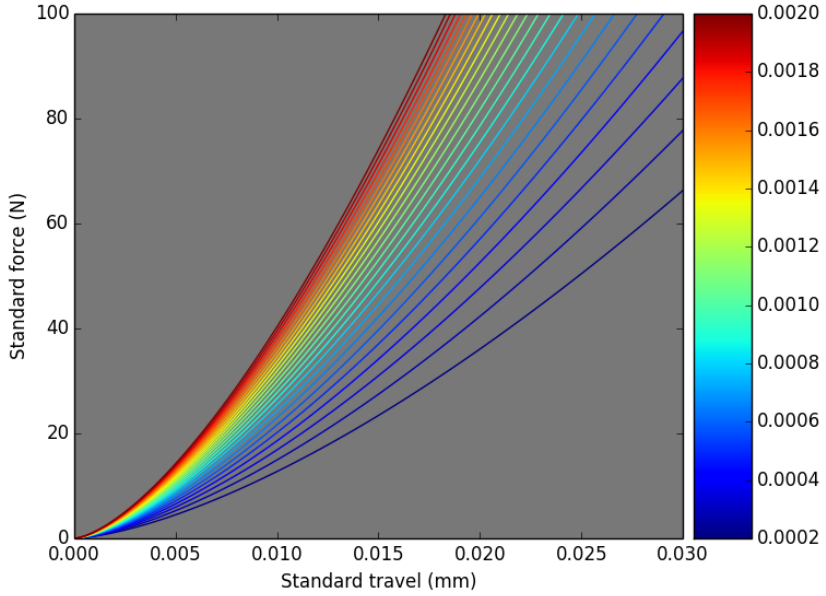


Figure 10.1: Hertzian responses of  $\text{Li}_2\text{TiO}_3$  pebbles compressed between platens. The colormap shows pebble diameters in m. The diameters span an order of magnitude from  $d_p = 0.2\text{mm}$  to  $d_p = 2\text{mm}$ .

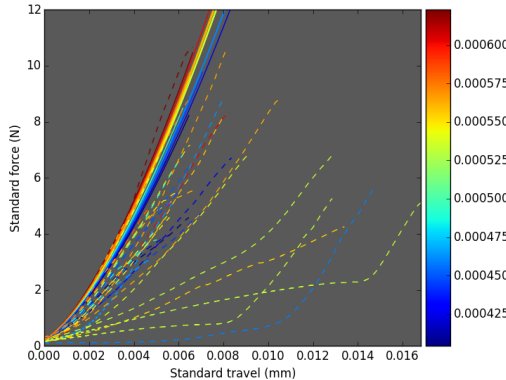


Figure 10.2: Dashed lines are  $\text{Li}_4\text{SiO}_4$  pebbles of approximately 0.5mm diameter. Solid lines are the Hertzian (Eq.10.1) responses based on each pebble's measured diameter.

Figure 10.1 shows that, for a given pebble diameter, there is a single curve strictly obeying Hertz theory, there is only a single force-displacement curve it can follow. However, when experiments are performed on single pebbles of  $\text{Li}_4\text{SiO}_4$  we see responses in the dashed lines of

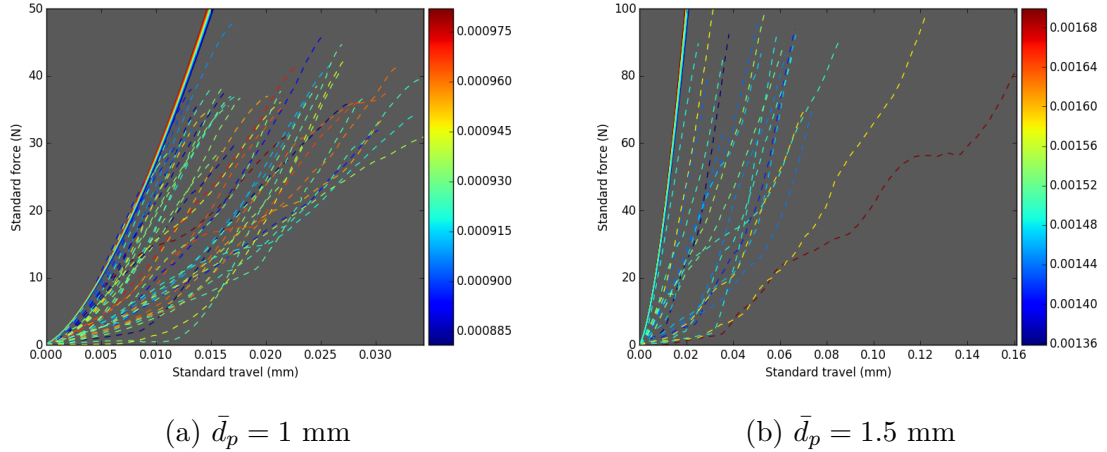


Figure 10.3: Dashed lines are  $\text{Li}_2\text{TiO}_3$  pebbles. Solid lines are the Hertzian (Eq.10.1) responses based on each pebble's measured diameter.

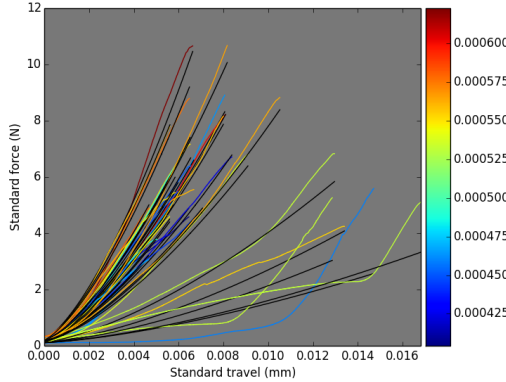


Figure 10.4: Force-displacement curves for  $\text{Li}_4\text{SiO}_4$  pebbles (in color) along with their Hertzian fits (in black) calculated with each pebble having a unique Young's modulus.

Fig. 10.2. Similarly for the dashed lines of  $\text{Li}_2\text{TiO}_3$  in Fig. 10.3.

Contrary to the diameter dependence seen in Fig. 10.1, the curves of Figs. 10.2, 10.3 do not demonstrate any relationship between diameter and force. For comparison, the solid lines on the figures for each ceramic show the predicted Hertzian response as calculated by Eq. 10.1 based on the measured diameter of each pebble. For both the  $\text{Li}_4\text{SiO}_4$  and  $\text{Li}_2\text{TiO}_3$  pebbles, there are very few pebbles that show a measured force-travel response that

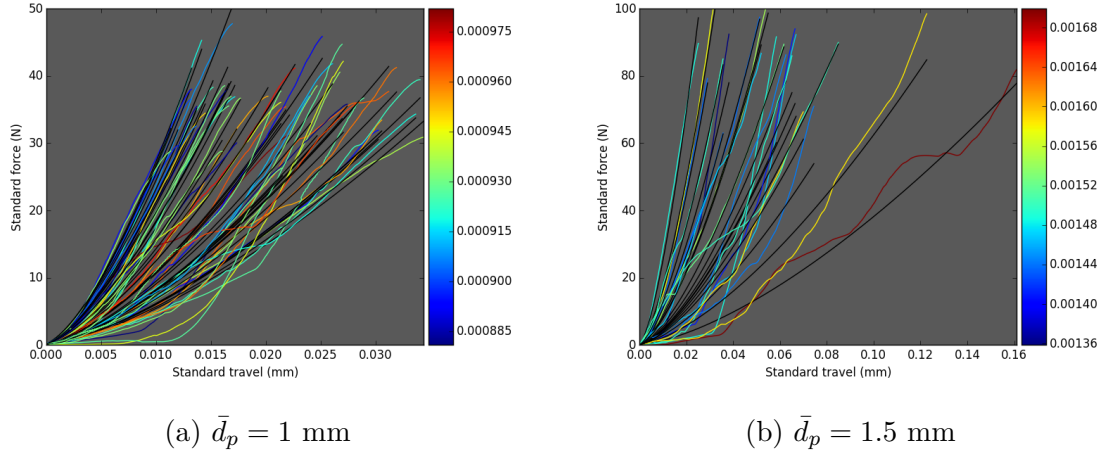


Figure 10.5: Force-displacement curves for  $\text{Li}_2\text{TiO}_3$  pebbles (in color) along with their Hertzian fits (in black) calculated with each pebble having a unique Young's modulus.

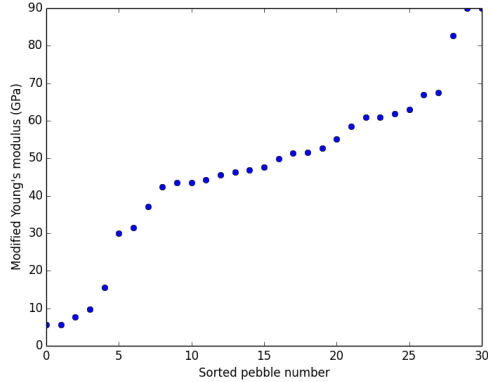
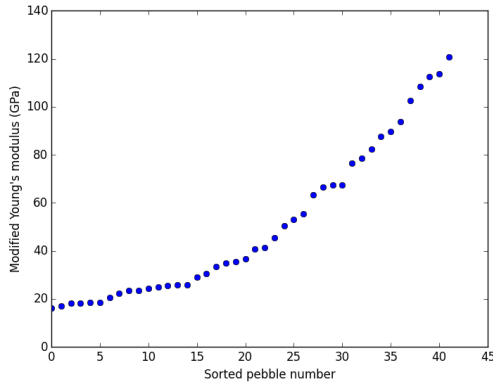


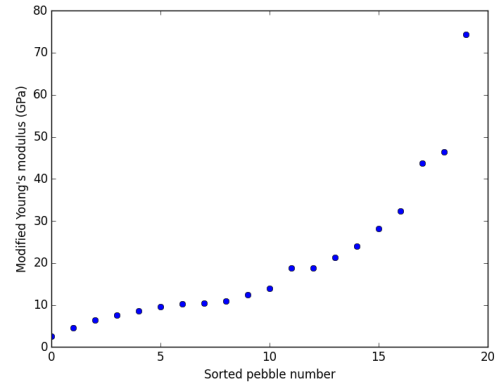
Figure 10.6: Distribution of modified Young's modulus for a batch of  $\text{Li}_4\text{SiO}_4$  pebbles. Most pebbles responded to compression with a Young's modulus well below the sintered pellet value of 90GPa.

is similar to the Hertzian prediction based on the material properties reported in literature. We conclude that variations in pebble diameter can not alone account for the variations in the force curves measured for the pebbles in our experiments.

We hypothesize that variation in measured curves is due to each pebble having Young's moduli that diverge from the values measured from sintered blocks as reported in literature.



(a)  $\bar{d}_p = 1 \text{ mm}$



(b)  $\bar{d}_p = 1.5 \text{ mm}$

Figure 10.7: Distribution of modified Young's modulus for a batch of  $\text{Li}_2\text{TiO}_3$  pebbles. All pebbles responded to compression with a Young's modulus well below the sintered pellet value of 126GPa.

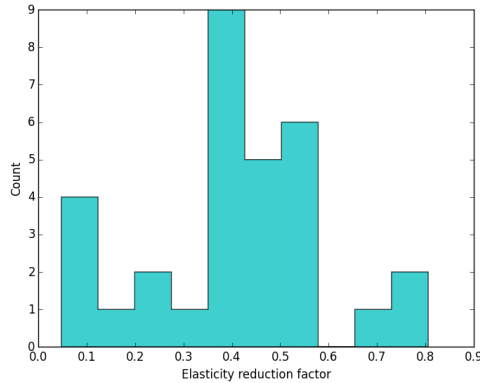


Figure 10.8: Histogram of  $\kappa$  for a batch of  $\text{Li}_4\text{SiO}_4$  pebbles. Most pebbles responded to compression with a Young's modulus well below the sintered pellet value of 90GPa.

Therefore each pebble displays a different apparent Young's modulus in the single pebble experiments. The apparent Young's modulus of each pebble is rooted in the manufacture of the pebbles which yields pebbles with slightly different internal structures. The differences in internal structure then cause the pebble to behave with different stiffnesses than the value expected from measurements of sintered pellets of lithium ceramics. In fact, the solid lines in Figs. 10.2, 10.3, as calculated from the measurements of sintered pellets, appear to be an

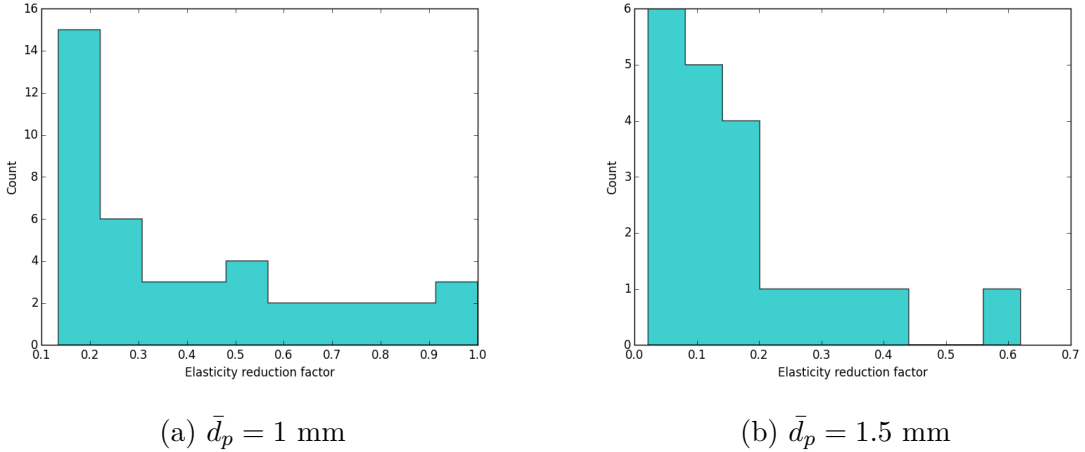


Figure 10.9: Histogram of  $\kappa$  for two batches of  $\text{Li}_2\text{TiO}_3$  pebbles. All pebbles responded to compression with a Young's modulus well below the sintered pellet value of 126GPa.

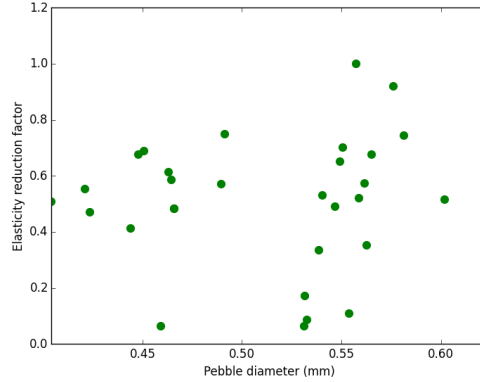


Figure 10.10: Scatter of  $\kappa$  against pebble diameter for a batch of  $\text{Li}_4\text{SiO}_4$  pebbles showing almost no relationship between apparent stiffness and diameter.

upper limit to the pebbles. Therefore we consider pebbles will emerge with values less than the value from literature,  $E_{\text{lit}}$  by some factor. To quantify the deviation of each pebble's  $E_{\text{peb}}$  from the sintered pellet, we introduce a  $\kappa$  factor, which we define as the elasticity reduction factor:

$$\kappa = \frac{E_{\text{peb}}}{E_{\text{lit}}} \quad (10.2)$$

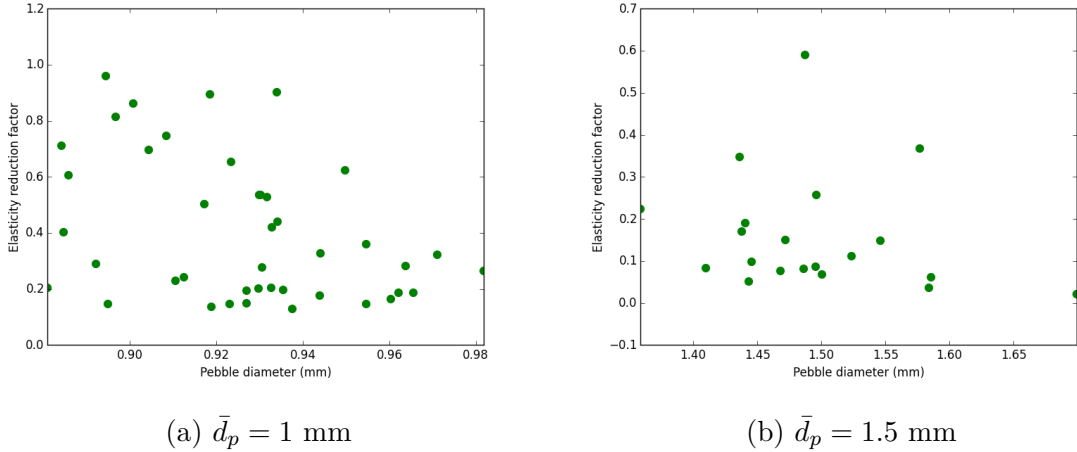


Figure 10.11: Scatter of  $\kappa$  against pebble diameter for two batches of  $\text{Li}_2\text{TiO}_3$  pebbles showing almost no relationship between apparent stiffness and diameter.

where

$$\kappa \in [0, 1]$$

If each pebble has a unique  $\kappa$  value, it would quantify the spread in elastic responses seen in the experiments. We find the value by assuming that the pebbles are, in fact, behaving in a Hertzian manner and we can fit the Hertzian to our experimental measurements. This allows us to back-out a  $\kappa$  value, or in other words the unique  $E_{\text{peb}}$  of that pebble. We take the sintered pebble value of Young's modulus for  $\text{Li}_4\text{SiO}_4$  to be  $E_{\text{lit}} = 90\text{GPa}$  and the value for  $\text{Li}_2\text{TiO}_3$  to be  $E_{\text{lit}} = 124\text{GPa}$ . Then we iterate over all values of  $k \in [0, 1]$  and compare the Hertzian response to that pebbles force-displacement curve. At each iteration, the L2-norm of the difference between Hertzian and experimental curves is used as the 'error'. The L2 norm,  $A$  for a given array,  $a$  is

$$||A||_F = \left[ \sum_{i,j} \text{abs}(a_{i,j})^2 \right]^{1/2} \quad (10.3)$$

This is a convenient way to compare the error at every point along the force-displacement curves. When the error is minimized, the elasticity reduction value corresponding the minimum is recorded for that pebble. In The Hertzian curves (in black) for each pebble are

plotted in green against the experimental curves in Figs. 10.4, 10.5.

Many of the curves for  $\text{Li}_4\text{SiO}_4$  in Fig. 10.4 seem to be fit well with a Hertzian curve with modified Young's modulus. The value of Young's modulus found for each pebble is plotted in Fig. 10.6. The Young's modulus of pebble numbers 0 to 4 are the very soft pebbles seen with very low forces on Fig. 10.4. The majority of pebbles, however, behave with a Young's modulus between 30 and 70 GPa. On the upper end, a few pebbles acted very similar to their sintered pellet counterpart with approximate value of 90GPa.

The two batches of  $\text{Li}_2\text{TiO}_3$  pebbles we analyzed (Fig. 10.5) are similarly fit well to different Hertzian curves. The apparent Young's modulii of the  $\text{Li}_2\text{TiO}_3$  pebbles are given in Fig. 10.7. These  $\text{Li}_2\text{TiO}_3$  pebbles have a large distribution of stiffness, from between 20 to 120 GPa for the 1 mm pebbles and roughly 2 to 80 GPa for the 1.5 mm pebbles.

A histogram of the  $\kappa$  factor for this batch of  $\text{Li}_4\text{SiO}_4$  pebbles is given in Fig. 10.8. For the  $\text{Li}_4\text{SiO}_4$  pebbles, the histogram resembles a normal distribution but for the large spike in pebbles with very small  $\kappa$ . When we look back to the force-travel plots of Fig. 10.2, the four softest pebbles show similar trends of long, relatively flat responses to travel before reaching a point where there is a sharp increase in the  $F-s$  slope. In the experiments, the flat sections of the curve occurred when the pebbles in the anvil were not perfectly spherical and rotated slightly under the application of a load. Once the pebbles rotated into a flat spot that could take a normal load without any angular moment, the force increased quickly under further travel. In light of this, it is unreasonable to consider their  $\kappa$  values as representing their true stiffness. Neglecting the four outliers in the histogram of Fig. 10.8, we are then left with a distribution much more closely resembling a normal probability distribution.

The histograms for the two batches of  $\text{Li}_2\text{TiO}_3$  are given in Fig. 10.9. The distributions for both batches of  $\text{Li}_2\text{TiO}_3$  pebbles more closely resemble Snedecor's F distribution with many pebbles behaving with a very small  $\kappa$ .

In Figs. 10.10 and 10.11 we see scatter plots of the pebble diameters and  $\kappa$  values for the different batches of lithium ceramic pebbles. A Pearson Correlation value was calculated for

each of the batches to find a relationship between diameter and  $\kappa$ . For the  $\text{Li}_4\text{SiO}_4$  pebbles, we find  $R = 0.198$  which is a weak positive correlation. For the  $\text{Li}_2\text{TiO}_3$  pebbles we have  $R = -0.385$  for  $\bar{d}_p = 1$  mm and  $R = -0.201$  for  $\bar{d}_p = 1.5$  mm. Both of these are weakly negatively correlated.

The implications of these results are that the Young's modulus traditionally used in DEM simulations for ceramic pebble beds in solid breeders is incorrect. In § 11.1, we will introduce  $\kappa$ , the elasticity reduction factor, into our DEM simulations. Numerical recreations of the probability distribution curves will be used to apply  $\kappa$  to pebbles in the ensemble. From the weak correlations between diameter and  $\kappa$ , we are free to ignore any diameter dependence when assigning  $\kappa$  values in the DEM framework. In the module where we assign Young's modulus to the particles in the ensemble will apply the distribution in a random fashion.

## 10.2 Translating Experimental Results to Pebble Bed Interactions

It is impractical, if not impossible, to accurately measure the contact forces between all the pebbles in a densely-packed, three-dimensional ensemble. In investigating the probability of pebbles becoming damaged (i.e. crushed or cracked) in a packed bed, we therefore rely on the combined information gained from indirect measurements of the entire pebble bed, crush experiments of individual pebbles, and the predictive capabilities of DEM simulations. In this study we look at the results of individual pebble crush experiments and create a metric to link the data to the contact forces measured in DEM to help predict when pebbles in the ensemble will become damaged.

### 10.2.1 Experimental Measurements of Strain Energy

The normal force between two elastic objects is a function of the material properties of the interacting objects (see Eq. 5.16). We cannot, therefore, directly compare the forces between pebble-test stand with pebble-pebble in an ensemble. An approach used by some solid

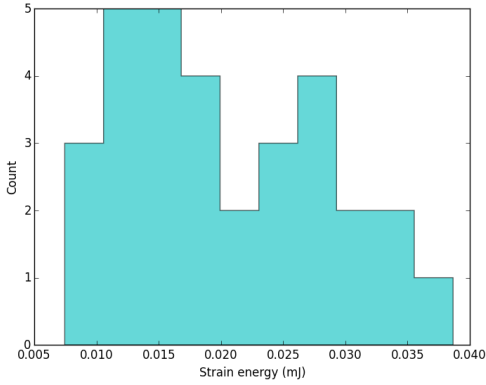


Figure 10.12: Histogram of the absorbed strain energy at the moment of crushing for  $\text{Li}_4\text{SiO}_4$  pebbles as measured in single pebble crush experiments.

breeder researchers is to relate the absorbed strain energy of the pebble.<sup>6,107</sup> We integrate the Hertzian force along the overlap to find the strain energy,  $W_\epsilon$ , of that contact.

$$W_\epsilon = \int_0^{\delta_c} F_n(\delta') d\delta' \quad (10.4)$$

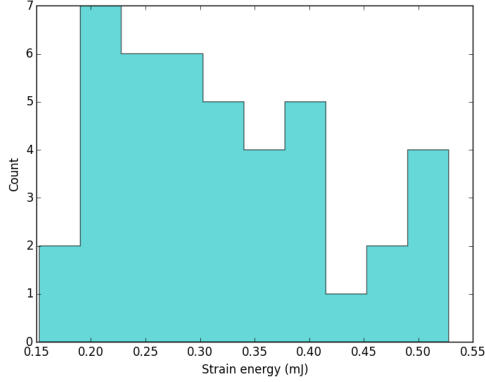
where the upper limit of the integration is the critical overlap  $\delta_c$ . Inserting Eq. 5.16 into Eq. 10.4,

$$W_\epsilon = \int_0^{\delta_c} \frac{4}{3} E^* \sqrt{R^*} \delta'^{3/2} d\delta' \quad (10.5)$$

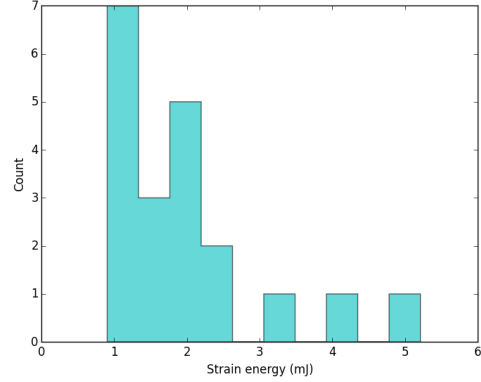
$$W_\epsilon = \frac{8}{15} E^* \sqrt{R^*} \delta_c^{5/2} \quad (10.6)$$

We will call the strain energy of the pebble compressed between platens as the lab strain energy,  $W_{\epsilon,L}$ . In pebble crushing experiments, we record the strain energy absorbed up to the point of crushing, the data for  $\text{Li}_4\text{SiO}_4$  and  $\text{Li}_2\text{TiO}_3$  pebbles are given in Figs. 10.12 and 10.13, respectively. Then the strain energy of two particles in contact will be  $W_{\epsilon,B}$ . The assumption we make is that, if each contact interaction is integrated to the proper critical overlap, the strain energies will be equal at that contact.

$$W_{\epsilon,L} = W_{\epsilon,B} = \frac{8}{15} E_B^* \sqrt{R_B^*} \delta_{c,B}^{5/2} \quad (10.7)$$



(a)  $\bar{d}_p = 1 \text{ mm}$



(b)  $\bar{d}_p = 1.5 \text{ mm}$

Figure 10.13: Histogram of the absorbed strain energy at the moment of crushing for  $\text{Li}_2\text{TiO}_3$  pebbles as measured in single pebble crush experiments.

We solve for the interacting pebble bed overlap as a function of the lab strain energy as

$$\delta_{c,B} = \left[ \frac{15W_{\epsilon,L}}{8E_B^* \sqrt{R_B^*}} \right]^{2/5} \quad (10.8)$$

This overlap can be reinserted to the Hertz force of Eq. 5.16 to find the critical force (crush force) of the interacting particles as a function of the critical strain energy of the lab. Doing this, we find,

$$F_{c,B} = CE_B^{*2/5} R_B^{*1/5} W_{\epsilon,L}^{3/5} \quad (10.9)$$

where  $C = \frac{4}{3} \left( \frac{15}{8} \right)^{3/5}$ .

Equation 10.9 is a generic translation between lab materials and packed bed materials. We will use the equation as the basis for our pebble crushing prediction in DEM simulations.

### 10.2.2 Calculating Critical Strain Energy

With the rise of micro-mechanical tools and computing power, attempting to predict when ceramic pebbles will crush in an ensemble, based on inter-particle contact forces, has received considerable attention. In this section we will review literature studying granular crushing.

Probability and statistics were applied to the study of packed beds of brittle grains by Marketos and Bolton.<sup>66</sup> The fundamental assumption in their predictive method was the independence of crushing events. They used their model to predict the initiation of crushing as well as the evolution of the packing after crushing. They created somewhat arbitrary probability distributions of the strength of their granular particles,

$$h(\Phi) = \frac{0.0395}{\sqrt{\Phi}} \quad (10.10)$$

where  $\Phi$  is a characteristic strength parameter falling between 160 and 640 N. The form of their distribution was based on single crushing tests on quartz particles from Nakata *et al.*.

A common alternative distribution is to use a form first proposed by Weibull for a material under uniform stress.<sup>56,67,70,107,108</sup> The form, as written by Zhao *et al.* is,

$$P_s = 1 - \exp \left[ - \left( \frac{W_c}{W_{\text{mat}}} \right)^m \right] \quad (10.11)$$

where  $W_c$  is the energy absorbed by the pebble and  $W_{\text{mat}}$  and  $m$  characterize the material. An important note is how to calculate the critical strain energy for the pebble. Refs.<sup>66</sup> and<sup>108</sup> note the necessity to consider the coordination number dependence on total strain energy. In other words, the total strain energy is the cumulative total of strain energy at every contact. Zhao *et al.* give strain as

$$W_c = \sum_{i=1}^{Z_i} \left( \frac{9}{80R_{ij}^*} \right)^{1/3} \left( \frac{1}{E_{ij}^*} \right)^{2/3} F_{n,ij}^{5/3} \quad (10.12)$$

where  $Z$  is the coordination number of pebble  $i$ .

However, Russell *et al.*, analyzed ideal granular assemblies for which they could find analytical solutions to stress distributions inside of pebbles.<sup>80</sup> In their work, failure of a granular particle initiates at the location of maximum of the stress invariant ratios. In the contact of elastic spheres, the stress fields near the contact areas are highly localized. Because of the highly localized effects, Russell *et al.* find that in granular assemblies the contributions to failure initiation are not additive. They discovered that the initiation of failure is always located adjacent to the largest force irrespective of the material properties or geometric size

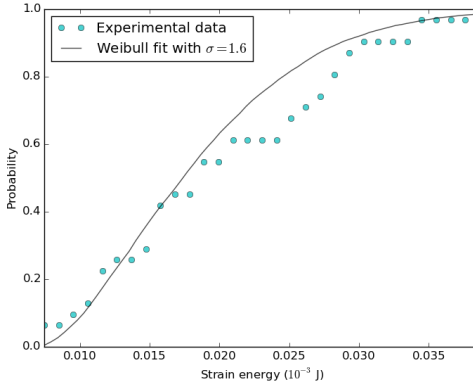


Figure 10.14: Fitting the strain energy with a Weibull distribution with shape parameter specific for the  $\text{Li}_4\text{SiO}_4$  pebbles.

of the pebbles in an ensemble. Russell *et al.*<sup>80</sup> conclude: the largest contact force acting upon a particle is the primary agent driving the damage of the individual. Based upon the failure criterion developed for brittle materials, crushing of an individual does not directly depend upon the presence or magnitude of any lesser contact forces acting on the particle or the material properties of the particle. Although their results were obtained for idealized assemblies, the results are generally true for any situation where multiple contact forces are present.

Based on the compelling arguments of Russell *et al.*, we will define our critical force as the maximum contact force on the pebble in our assembly,

$$F_c = \max F_{n,ij} \quad (10.13)$$

Then we can say a pebble is crushed when the force on the pebble in the bed is greater than the critical bed force defined from Eq. 10.9,

$$F_c > F_{c,B} = \frac{4}{3} \left( \frac{15}{8} \right)^{3/5} E_B^{*2/5} R_B^{*1/5} W_{\epsilon,L}^{3/5} \quad (10.14)$$

In the implementation into DEM, the probabilistic features appear naturally in this formulation from the measured probability distribution of  $W_{\epsilon,L}$ . In the experiments on

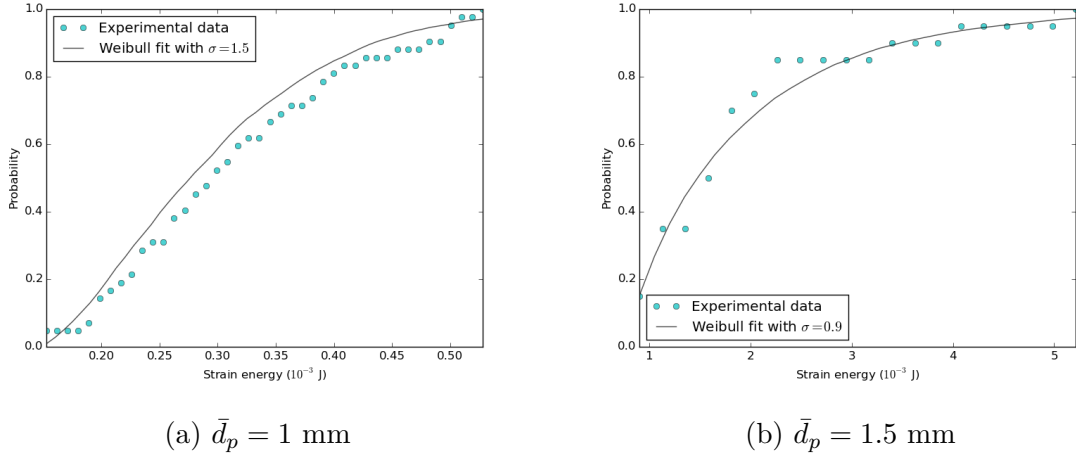


Figure 10.15: Fitting the strain energy with a Weibull distribution with shape parameter specific for the two batches of  $\text{Li}_2\text{TiO}_3$  pebbles.

crushing individual pebbles, the critical strain energy is measured strain energy at the point of crushing. This value follows a probability distribution and therefore imparts a distribution shape to the  $F_{c,B}$  prediction. Cumulative distribution functions are generated for the strain energy data (see Figs. 10.13 and 10.13). From that data, we fit Weibull distribution curves, of the form

$$\Xi = \lambda [-\ln(W_\epsilon)]^{1/\sigma} \quad (10.15)$$

where the shape parameter,  $\sigma$ , is fit to the specific curve of each set of experimental data and the second parameter,  $\lambda$  is

$$\lambda = \bar{W}_\epsilon - \min W_\epsilon$$

In Figs. 10.14 and 10.15 we show the experimental data and the Weibull fits specific to the ceramic material and batch. The Weibull distribution functions will be used again when we generate strength parameters to assign to pebbles in the discrete element simulations of pebble crushing, addressed in § 11.3.

# CHAPTER 11

## Background Numerical Studies

### 11.1 Proper Selection of Young's Modulus for DEM Simulations

The discrete element method is used by many ceramic breeder researchers to model the interaction of individual pebbles in an ensemble in an effort to obtain a more detailed understanding of pebble beds than is possible with experimental measurements of effective properties. For example see Refs.<sup>4,6,40,59,93,105</sup> The fundamental assumption in the DEM formulation is that each pebble acts perfectly elastically and adheres to Hertz theory for contacting spheres. With Hertz theory, one finds contact forces as a simple function of: the virtual overlap between two objects, the Young's modulus of the contacting material (and Poisson ratio), and radii of the two. In past studies, the Young's modulus of the ceramic materials used in DEM simulations was taken from historical data, for instance lithium metatitanate from Ref.<sup>43</sup>

However, based on observations of the experimental data from single pebble crush data (see § 10.1), we propose a modification of the Young's modulus to be used in DEM simulations for a batch of ceramic pebbles. The force-displacement curves of Figs 10.4 and 10.5 demonstrate how far from the ideal Hertzian curves the majority of ceramic pebbles behave.

The Hertzian force is linearly proportional to the pair Young's modulus of contacting spheres. Based on the  $\kappa$  values found in § 10.1, the apparent Young's moduli of  $\text{Li}_4\text{SiO}_4$  and  $\text{Li}_2\text{TiO}_3$  are, on average, less than half the values given for sintered materials in literature.

For the case of  $\text{Li}_2\text{TiO}_3$ , the average value was closer to only 10% of the value from literature. Thus the actual contact forces in pebble beds may be 10% of the values we have found from DEM simulations! The contact force is a critical value for determining the conduction heat transport between pebbles as well as damage prediction. It is crucial that we are using proper material properties in our simulations. In this study, we will compare pebble beds in uni-axial compression tests. One bed will be composed of pebbles with the Young's modulus from literature and the other will be composed of pebbles with a distribution of Young's modulus that fits the distributions from experiments.

### 11.1.1 Numerical Setup

We model our pebble beds undergoing a standard stress-controlled uni-axial compression up to 6 MPa. We will measure the macroscopic stress-strain for some parametrically varied pebble beds and compare the curves. At the moment of maximum stress, we can investigate the differences in contact forces of those pebble beds.

Our pebble ensemble is composed of 0.5mm diameter  $\text{Li}_4\text{SiO}_4$  pebbles. The pebble beds are initiated and packed in the same manner as § 12.1. There are two main bed groups. Set A: the first set of three beds (A.1-3) contain a single type of pebble with  $E = 90\text{GPa}$ . Set B: the second set of four beds (B.1-4) contain ten types of pebbles with their Young's modulus assigned in a discrete, random way to satisfy the distribution seen from experimental data. For the DEM study, we fit to  $\text{Li}_4\text{SiO}_4$  pebbles with a Weibull distribution of shape parameter  $\sigma = 1.6$  where the average stiffness was  $\bar{E} = 49 \text{ GPa}$ . The description of the two sets of pebble beds is visually represented in Fig. 11.1. The pebble bed geometry was also the same used in the study of Ref.;<sup>93</sup> two virtual walls in the x-direction located at  $x_{\lim} = \pm 20R_p$ , periodic boundaries at the limits of  $y_{\lim} = \pm 15R_p$ , and a total of 8000 pebbles packed into the volume to an approximate height of  $z_{\lim} = 20R_p$ .

Among both sets, a parametric study was done on pebble radius and coefficient of friction. The radii of pebbles in beds A.1, A.2, B.1, and B.2 were constant at  $R_p = .25 \text{ mm}$ . The radii

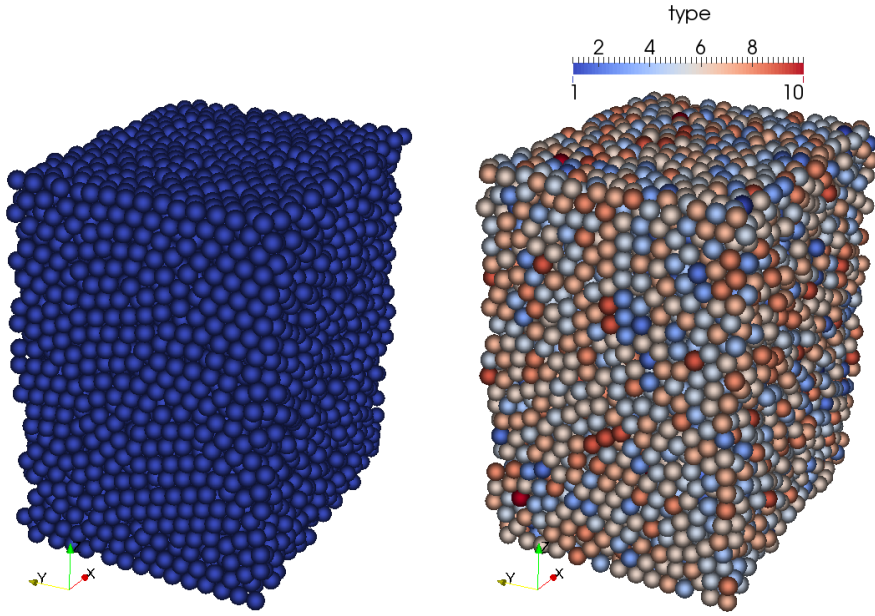


Figure 11.1: On the left, set A, a pebble bed with a single type, of  $E = 120$  GPa. On the right, set B, is a pebble bed with 10, randomly distributed types; each type corresponds to a reduced, apparent Young's modulus as derived from experimental data.

of pebbles in beds A.3, B.3, and B.4 followed a Gaussian distribution about  $\bar{R}_p = 0.25$  mm:  $\mu_d = R_p$  and  $sigma_d = R_p$ . The coefficient of friction was set at  $\mu = 0.2$  for beds A.1, A.3, B.1, and B.3; the coefficient of friction was  $\mu = 0.3$  for beds A.2, B.2, and B.4.

### 11.1.2 Results from Uni-axial Compression

A constant-velocity, uniaxial compression was applied to the pebble beds. A single cycle up to 6 MPa was used on all the beds. The macroscopic measurements of stress-strain are shown for all the pebble beds in Fig. 11.2.

Naturally, the pebble beds with smaller Young's modulus (with circle markers) are more compliant to external loads. The result is true regardless of the coefficient of friction or distribution of pebble radius studied here. Group B moved to an average strain of about 2.6% at 6 MPa, by comparison the beds of Group A only had strained 1.9 % on average

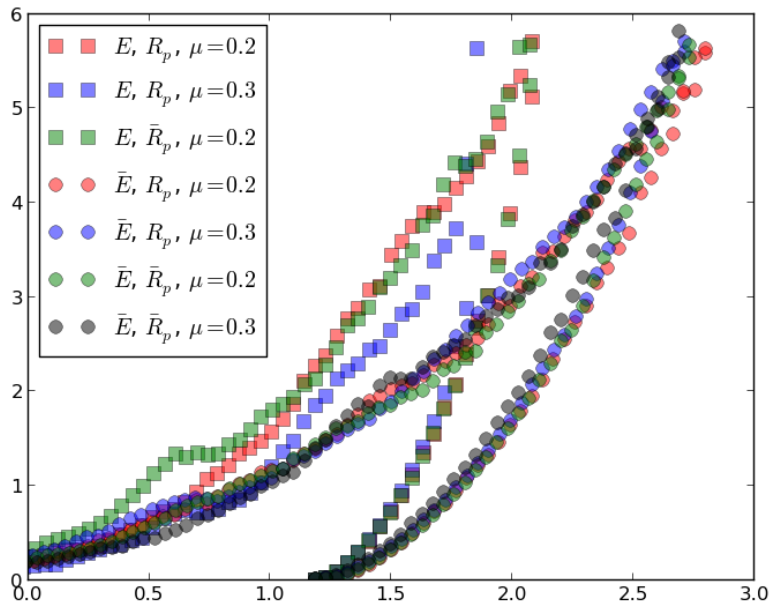


Figure 11.2: Stress-strain responses of pebble beds with: squares, constant Young’s modulus; and circles, Gaussian distribution of Young’s modulus. The constant Young’s modulus beds all had much firmer responses for all parametric cases studied here.

to reach the same stress. Among the beds of each group, pebble beds with constant radius pebbles behaved virtually the same as similar pebble beds with a Gaussian distribution on radius. An increase in the coefficient of friction had a moderate impact on the overall stress-strain response.

The parametric study here shows that the largest contributor to stress-strain response is the Young’s modulus. The coefficient of friction and radius distribution had comparatively insignificant influence. A pebble bed geometry more directly comparable to oedometric compression experiments should be used to allow direct comparison and validation of the numerical models.

At the point of peak stress for each bed, we use DEM results to visualize the distribution of contact forces among all pebbles in the ensemble. A plot of the probability distributions of all the beds together, Fig. 11.3, shows that the majority of the contacts in all the beds are

equally small. There are a few overall trends we observe from the results however. The pebble beds with the constant Young's modulus are always higher for their comparable version with distributed Young's modulus. For pebble beds with comparable Young's moduli and radii, higher coefficients of friction generally have higher peak contact forces. Pebble beds' radius distributions have much less impact on peak contact forces than either coefficient of friction or Young's modulus. Another method of comparing overall contact force distributions is to consider predictions on pebble cracking which assigns a strength value at random to pebbles in the bed, according to Eq. 10.14. At the point of maximum stress, this is done and the results are shown in Tab. 11.1.

While overall the predicted number of broken pebbles is small, we compare similar parameteric pebble beds and in each case pebble beds with modified Young's modulus overall predict smaller percentages of broken pebbles. Pebble crushing is a major topic for the overall evaluation of the feasibility of ceramic pebble beds in fusion reactors. This study reveals that past DEM work on pebble crushing was likely over-predicting the extent of crushing if the Young's modulus used in the study was much larger than the realistic response of individual pebbles.

### 11.1.3 Conclusions for Modified Young's Modulus

Models based on the discrete element method have received considerable attention by ceramic breeder researchers. The method is attractive as it is based on material properties and forgoes many of the assumptions necessary in empirical equations of effective properties for continuum models. Variation in production techniques for ceramic pebbles lead to changes in ceramic microstructure, as evident in the wide distribution of crush loads reported in past studies, *e.g.* Refs.<sup>65,106</sup> By the same token, the different microstructures should naturally lead to variation in Young's modulus. However up to now values of Young's modulus used in numerical models are taken from values measured for large sintered pellets of ceramic materials. Based on single pebble experiments and the application of Hertz theory, a technique for introducing a modified Young's modulus into DEM models has been proposed

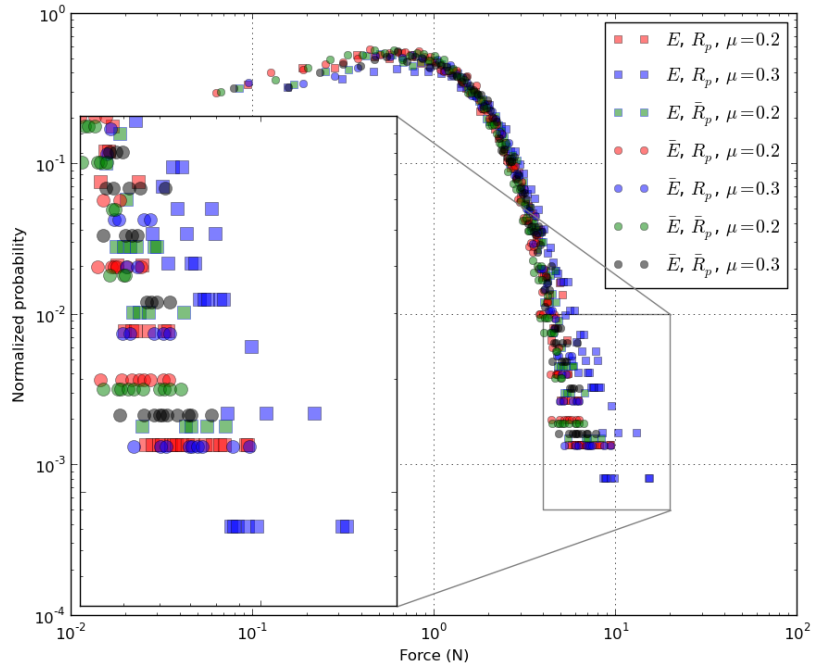


Figure 11.3: Probability distribution of contact forces in all the pebble beds studied here. Elastic moduli value is the largest contributor to higher peak contact forces among pebbles.

here. DEM simulations show the impact of modified pebble elasticity on both macroscopic measurements of stress-strain curves as well as mesoscopic measures of inter-pebble contact force – with major implications for prediction of pebble crushing in ceramic pebble beds. The models applying the elasticity reduction factor,  $k$ , predict more compliant pebble beds and smaller peak contact forces in beds and thus fewer crushed pebbles.

## 11.2 Jeffreson Correction to Lumped Capacitance Method

In § 6.2.2, we discuss correlations for heat transfer coefficients of spheres in a packed bed. Then those correlations are utilized with CFD-DEM computational routines in eq. (8.2). When implemented in the DEM-based modeling, we make the lumped capacitance assumption,

Table 11.1: Comparisons for the two styles of Young's modulii used in the study.

Bed label	Parameters	Predicted crushed %
A.1	$E, R_p, \mu = 0.2$	0.3
A.2	$E, R_p, \mu = 0.3$	1.0
A.3	$\bar{E}, \bar{R}_p, \mu = 0.2$	0.9
B.1	$\bar{E}, R_p, \mu = 0.2$	0.6
B.2	$\bar{E}, R_p, \mu = 0.3$	0.8
B.3	$\bar{E}, \bar{R}_p, \mu = 0.2$	0.4
B.4	$\bar{E}, \bar{R}_p, \mu = 0.3$	0.7

tion for each particle in the ensemble. The assumption eases the computational efforts of solving for the temperature distribution inside each particle; each particle is treated as isothermal. The accuracy of the lumped capacitance method is described by the Biot number,

$$\text{Bi} = \frac{hd_p}{k_r} \quad (11.1)$$

and for  $\text{Bi} \ll 1$  the lumped capacitance method accurately models the behavior of a solid interacting with a fluid. For  $\text{Bi} \approx 0.1$ , the error from the lumped capacitance method is only about 5%. In solid breeder volumes, the particles are generally small, solid conductivity low, and heat transfer coefficient generally also low. This leads to small-to-moderate Biot numbers expected in the packed bed. In this section we will analyze the accuracy of the lumped capacitance and introduce a correction method to account for inaccuracies of the method at moderate Biot numbers.

We simplify the case of a packed bed and only consider a single sphere with volumetric

heat generation submerged in and thermally interacting with a fluid. The sphere will be of radius  $R = d_p/2$ , as shown in Fig. 11.4. The sphere will initially be at a uniform temperature of  $T_i$ . The fluid temperature will remain constant at  $T_f$

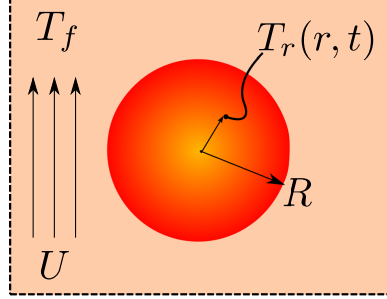


Figure 11.4: CONTROL VOLUME OF A SINGLE SPHERICAL PARTICLE IN A PACKED BED

### 11.2.1 Lumped Capacitance Solution for Sphere

We will solve for a single sphere interacting with a passing fluid, as shown in Fig. 11.4. We make the lumped capacitance assumption for this sphere. The solid is initially at temperature  $T_0$ , with constant volumetric heat generation, cooling in a fluid with constant heat transfer coefficient. The fluid will remain constant at  $T_f$ .

The time response of the sphere's temperature is dictated by the balance of energy to/away from the solid,

$$\rho_r C_r V \frac{dT}{dt} = -hA(T - T_f) + gV \quad (11.2)$$

Eq. 11.2 is solved in dimensionless form with the following nondimensional parameters of temperature and time,

$$\theta = \frac{T(t) - T_f}{T_0 - T_f} \quad (11.3a)$$

$$\tau = \frac{t}{R^2/\alpha} \quad (11.3b)$$

where  $\alpha$  is the thermal diffusivity of the sphere,  $T_0$  is the initial isothermal temperature of the sphere, and  $T_f$  is the constant fluid temperature. The resulting temperature distribution is,

$$\theta_{LC} = \left(1 - \frac{G}{3\text{Bi}}\right) \exp(-3\text{Bi}\tau) + \frac{G}{3\text{Bi}} \quad (11.4)$$

where we define a dimensionless heat generation,

$$G = \frac{gR^2}{k(T_0 - T_f)} \quad (11.5)$$

The energy of the sphere, relative to the fluid, in nondimensional terms is

$$E^*(\tau) = \frac{E(\tau)}{E_0} \quad (11.6)$$

where  $E_0$  is the initial energy of the sphere,

$$E_0 = \rho_r C_r V (T_0 - T_f) \quad (11.7)$$

Thus for a sphere with the lumped capacitance model, in nondimensional form, is simply

$$E_{LC}^*(\tau) = \theta_{LC}(\tau) \quad (11.8)$$

The nondimensional energy profile of Eq. 11.8 is plotted over the nondimensional time of  $\tau \in [0, 1/\text{Bi}]$  in Fig. 11.5.

Reviewing Eq. 11.4 we see that the speed of decay is dictated by the term in the exponential,  $3\text{Bi}$ . Meanwhile, the steady-state value being approached is given by  $\frac{G}{3\text{Bi}} = \frac{gR}{h(T_0 - T_f)}$ . It is important for this discussion to point out that because both the nondimensional heat generation and Biot number terms contain the solid conductivity, the steady-state value of the lumped capacitance model will not change for varying solid conductivity even if it leads to different Biot numbers. We will return to this point in the next section when we compare

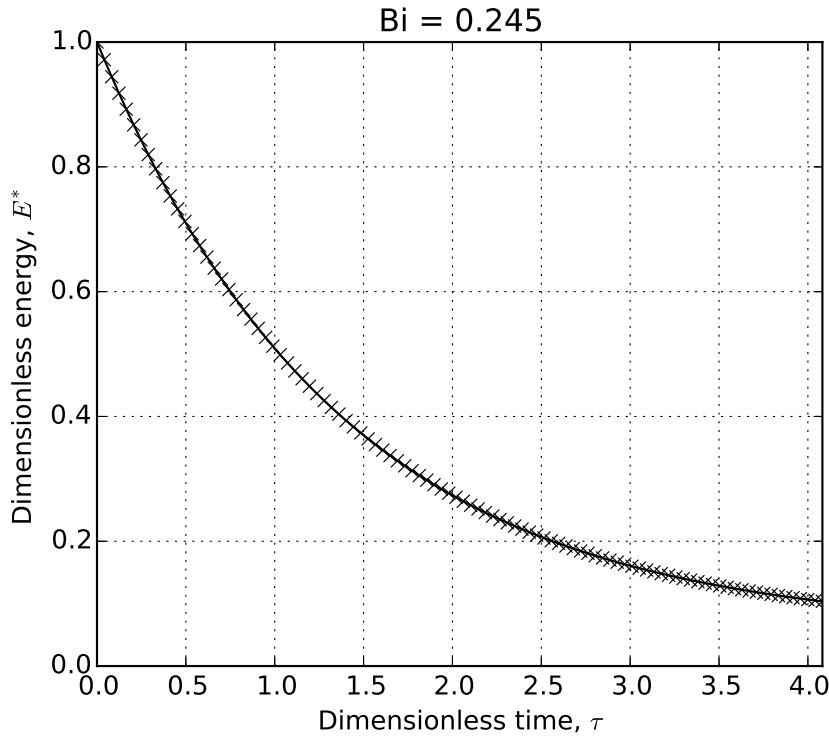


Figure 11.5: Lumped capacitance model: Sphere energy profile decaying from an initial value to a time of  $1/\text{Bi}$

the lumped capacitance model to the exact solution when internal conduction of the solid is considered.

### 11.2.2 Exact Solution for Sphere

We again analyze the sphere of Fig. 11.4 but now will account for internal temperature gradients inside the sphere. The details of the analytic solution for a sphere with heat generation interacting with a fluid is given in Appendix A. We again solve in terms of the nondimensional temperature and time introduced in § 11.2.1 as well as a nondimensional radius,

$$\begin{aligned}\theta &= \frac{\mathbb{T}}{\mathbb{T}_0} \\ \rho &= \frac{r}{R} \\ \tau &= \frac{t}{R^2/\alpha}\end{aligned}$$

The energy conservation equation for the sphere with internal temperature gradient, in nondimensional form  $\theta_{TG}$ , is

$$\frac{1}{\rho} \frac{\partial^2}{\partial \rho^2} (\rho \theta_{TG}) + G = \frac{\partial \theta_{TG}}{\partial \tau} \quad (11.9)$$

With the initial condition and boundary conditions outlined in Appendix A, the nondimensional temperature distribution inside the sphere is

$$\theta_{TG}(\rho, \tau) = \left( \frac{G}{6} + \frac{G}{3\text{Bi}} - \rho^2 \right) + \sum_{n=1}^{\infty} \exp(-\zeta_n^2 \tau) \frac{\sin(\zeta_n \rho)}{\rho} \frac{Z(\zeta_n)}{N(\zeta_n)} \quad (11.10)$$

where  $\zeta_n$  are the eigenvalues of the equation and the functions of  $\zeta_n$  ( $Z, N, C$ ) are given in Appendix 11.2.2.

The accompanying nondimensional energy of the sphere is integrated to,

$$E_{TG}^*(\tau) = \left( \frac{G}{15} + \frac{G}{3\text{Bi}} \right) + 3 \sum_{n=1}^{\infty} \exp(-\zeta_n^2 \tau) \frac{Z(\zeta_n)}{N(\zeta_n)} C_n(\zeta_n) \quad (11.11)$$

We now compare the exact solution from Eq. 11.11 to the solution of energy given by the lumped capacitance model of Eq. 11.8. The two profiles are given in Fig. 11.6.

For the value of Biot number here,  $\text{Bi} < 0.5$ , the profile of the analytic solution of the sphere is well-captured by the lumped capacitance model. The maximum relative error over the time span, as defined by

$$\text{error} = \frac{|E_{TG}^*(\tau) - E_{LC}^*(\tau)|}{E_{TG}^*(\tau)} \quad (11.12)$$

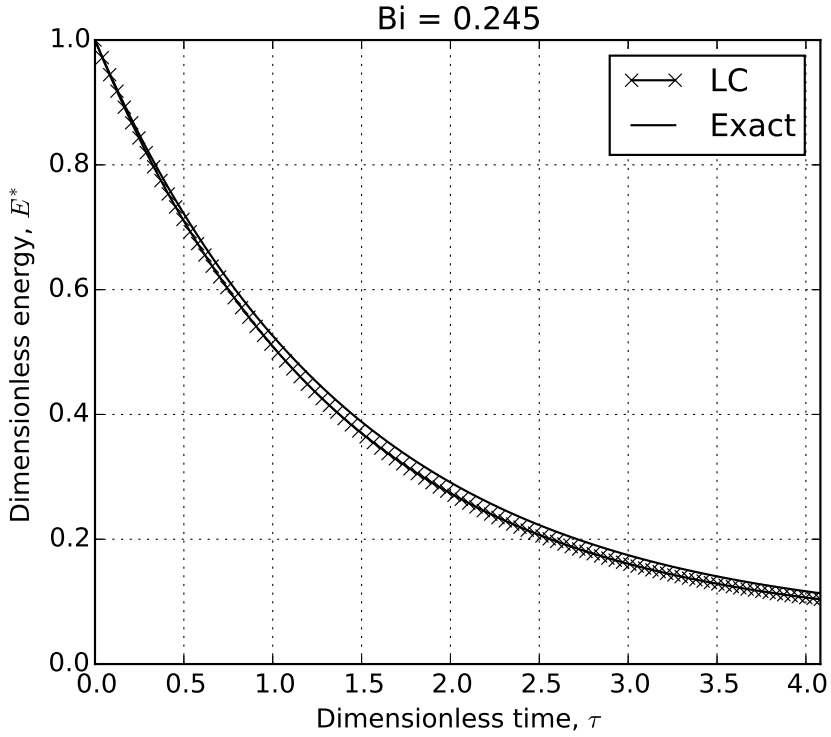


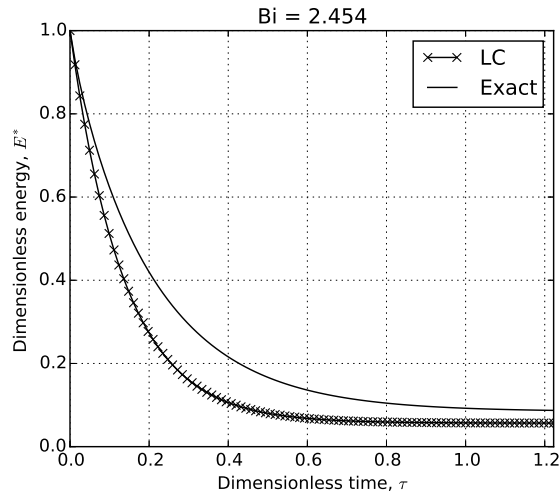
Figure 11.6: Analytic and lumped capacitance models: Sphere energy profile decaying from an initial value to a time of  $1/\text{Bi}$

is always less than 10%.

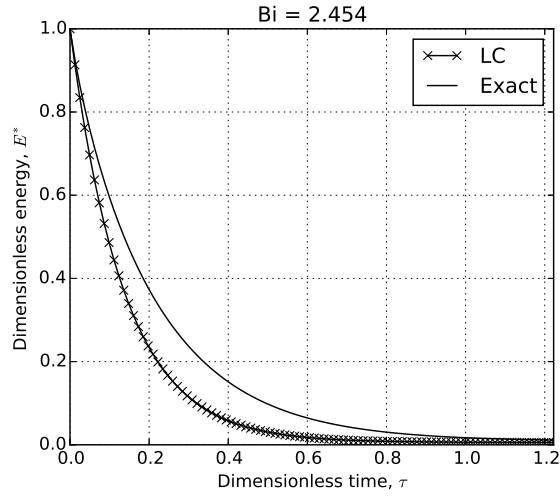
We consider now the same size sphere but with the Biot number increased by an order by: a) a conductivity of  $k = k_r/10$  and b) a heat transfer coefficient of  $h = 10h_f$ . The two physical changes to the system result in the same Biot number but as we can see in Fig. 11.7, there are drastic changes in the results.

Seen in Fig. 11.7a, the lumped capacitance solution both over-predicts the speed at which the sphere reaches a thermal steady-state as well as the value of the steady-state. Comparatively, in Fig. 11.7b, for the same Biot number the lumped capacitance solution again over-predicts the speed to thermal steady-state by the same rate but is relatively accurate for the steady-state value itself.

To first address the source of error on the steady-state value, we view the steady-state



(a) The Biot number increased from a decrease in the solid conductivity.



(b) The Biot number increased from an increase in the heat transfer coefficient.

Figure 11.7: Analytic and lumped capacitance models: Sphere energy profile decaying from an initial value to a time of  $3/\text{Bi}$ . The same Biot number produces different results for the exact solution of a sphere with heat generation.

terms of the two solutions. From Eq. 11.11, we write the steady-state term of the exact solution as

$$E_{TG,ss}^* = \frac{G}{15} + \frac{G}{3\text{Bi}} \quad (11.13)$$

Comparatively, we write the steady-state term of the lumped capacitance solution from § 11.2.1 as,

$$E_{LG,ss}^* = \frac{G}{3\text{Bi}} \quad (11.14)$$

We clearly see that the two steady-state values differ by the contribution of  $\frac{G}{15}$  on the exact solution. This term does not appear in the lumped capacitance solution because it does not account for the temperature difference through the sphere. The nondimensional heat generation term is given in Eq. 11.5; it is importantly a function of thermal conductivity but not the heat transfer coefficient. This explains the difference between steady-state values in Fig. 11.7 when we modified the two parameters.

To address the inaccuracies in the time-dependent response of the lumped capacitance method with large Biot number, we will make use of the so-called Jeffreson Correction described by Van Lew<sup>94</sup> and Xu *et al.*<sup>100</sup> In their work, they considered a heated heat transfer fluid interacting with a low conductivity thermal storage material. The solar thermal storage systems they analyzed often had moderate-to-large Biot numbers but they could continue to apply the lumped capacitance model by applying the Jeffreson Correction.<sup>50</sup> The details of the Jeffreson correction as applied to a system with volumetric heat generation will be discussed next.

### 11.2.3 Jeffreson Correction for Sphere

In Fig. 11.7, the lumped capacitance model predicted a much faster decay to steady-state than the exact solution. Jeffreson summarized a correction to the lumped capacitance model via a reduction in the heat transfer coefficient as a function of the Biot number. The smaller

heat transfer coefficient effectively slowed the decay to steady-state as predicted by the lumped capacitance method. The correlation to correct the heat transfer coefficient due to solids with large Biot number is given by Jeffreson.<sup>50</sup> The Jeffreson correction for a sphere is,

$$h_p = \frac{h}{1 + Bi/5} \quad (11.15)$$

where  $h_p$  is the modified heat transfer coefficient of the particle with an internal temperature gradient. An increase in the Biot Number (or increase of thermal gradient inside the solid) results in a decrease in the heat transfer coefficient  $h_p$ . A modified Biot number can then also be written as

$$Bi_p = \frac{h_p d}{k_r} = \frac{Bi}{1 + Bi/5} \quad (11.16)$$

Applying the Jeffreson Correction to Eq. 11.4,

$$\theta_{JC} = \left(1 - \frac{G}{3Bi_p}\right) \exp(-3Bi_p\tau) + \frac{G}{3Bi_p} \quad (11.17)$$

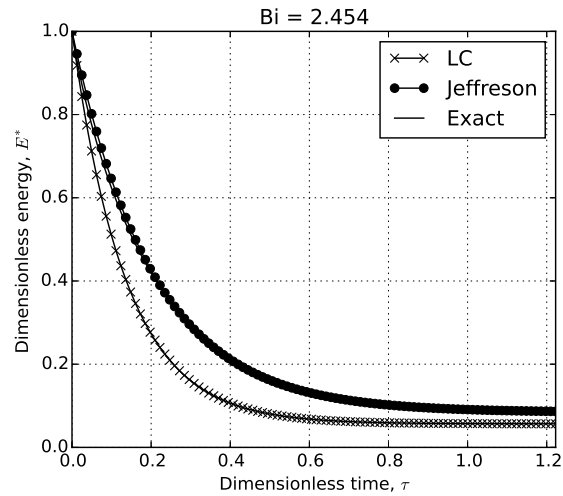
and thereby Eq. 11.8 gives

$$E_{JC}^*(\tau) = \theta_{JC}(\tau) \quad (11.18)$$

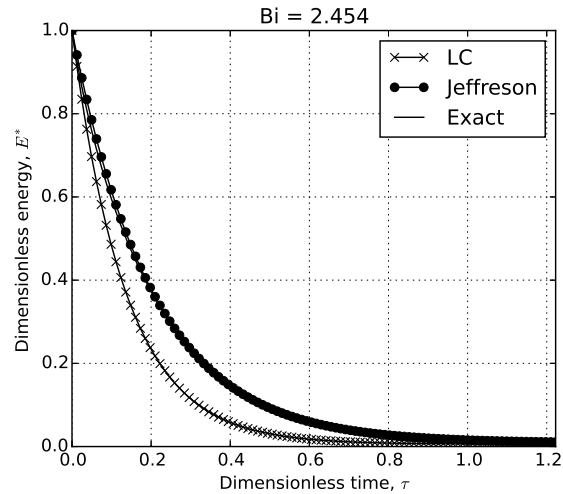
We then plot the energy profiles from the lumped capacitance model (LC), the Jeffreson correction (JC), and the exact solution together in Fig. 11.8

The Jeffreson correction to the lumped capacitance method allows the simple model to capture the proper transient as well as steady-state values for this sphere with a moderately sized Biot number. To look more closely, we view the instantaneous error (see Eq. 11.12) in Fig. 11.9.

For the value of  $Bi > 1$  due to either low conductivity (Fig. 11.9a) or high heat transfer coefficient (Fig. 11.9b), the error in the Jeffreson correction is always under 10%; often closer

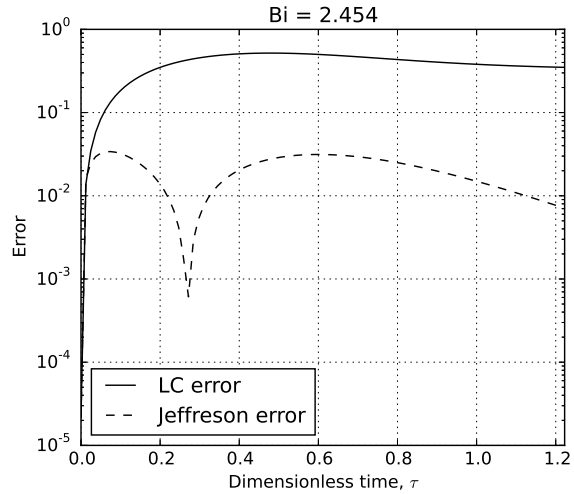


(a) The Biot number increased from a decrease in the solid conductivity.

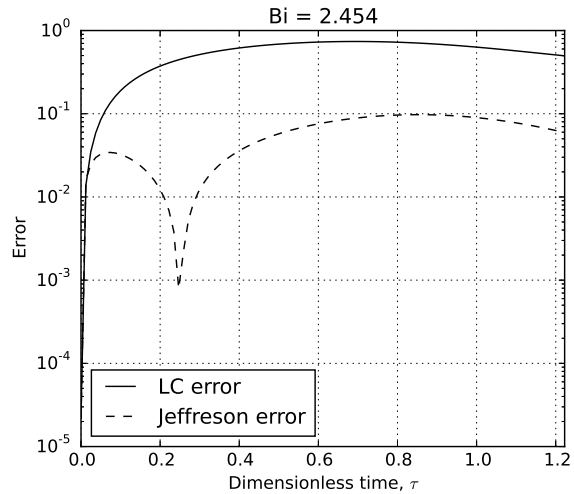


(b) The Biot number increased from an increase in the heat transfer coefficient.

Figure 11.8: Analytic, lumped capacitance model, and LC model with Jeffreson correction: Jeffreson correction corrects for transient and steady-state errors of lumped capacitance.



(a) The Biot number increased from a decrease in the solid conductivity.



(b) The Biot number increased from an increase in the heat transfer coefficient.

Figure 11.9: Error of lumped capacitance and reduced error of the model with Jeffreson correction for moderate Biot number.

to only 1%. This is in opposition to the standard lumped capacitance method which has 50-80% error for both transient and steady-state values.

The lumped capacitance method allows researchers to simplify transient, conjugate heat transfer problems with an isothermal solid. In the discrete element method, the assumption of isothermal solid is innate in the framework of the method. With the implementation of the Jeffreson correction in the discrete element method, we have confidence in the fidelity of the heat transfer in for moderately sized Biot numbers. The Jeffreson correction will be implemented into the DEM computations via Eq. 11.16.

### 11.3 Pebble Damage Modeling

Research on pebble damage has been taken up by others in the fusion community to predict the onset of pebble crushing as a function of an external pressure and the resulting changes to mechanical properties such as the stress-strain of the pebble bed.<sup>6, 106, 107</sup> Other fields of engineering have also employed DEM in studies of granular crushing with generally similar modeling approaches.<sup>66, 70</sup>

In modeling pebble damage, there are two main tasks: predicting when the grain crushes and what happens when it does. For the former, the task is to develop a model for predicting a pebble crushing event; *i.e.* what load (mechanical or thermal) will cause a pebble to crack, shatter, fracture, etc. To tackle the latter is to develop a model which simulates the damage of that pebble; *i.e.* a scheme to treat a cracked, shattered, or crushed pebble in the assembly as small particles, removed particles, or particles with modified material properties.

This numerical study will focus on the ‘what happens’ question. In work by Marketos and Bolton, they treated a crushed pebble very similar to Van Lew *et al.*; when a pebble was damaged it was removed completely from the assembly.<sup>66, 93</sup> Marketos and Bolton study the stress-strain response of a pebble bed with a predictive crushing routine while we studied the effective thermal conductivity of a damaged pebble bed.

However, the technique of removing a pebble is limited by the fact that energy input into

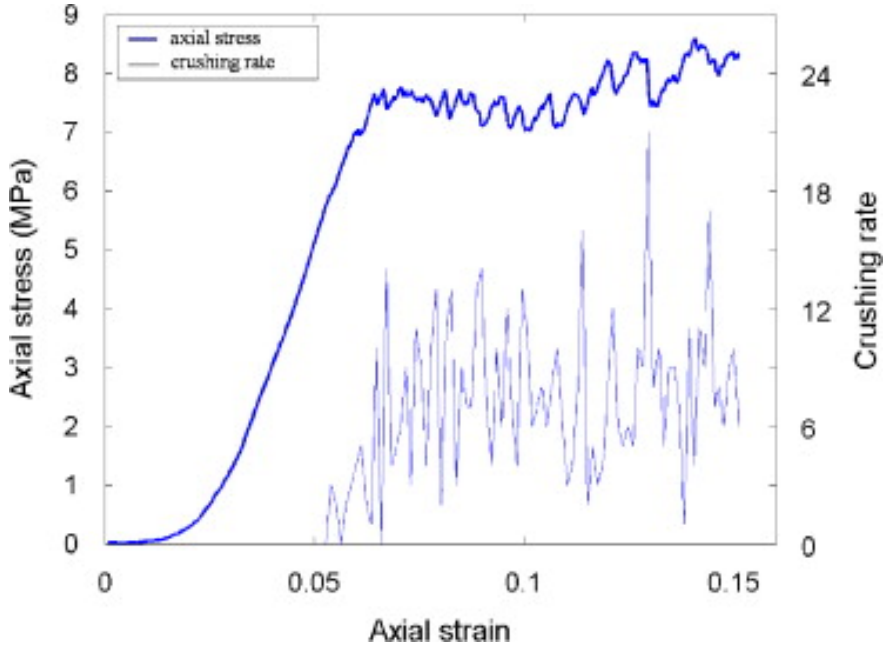


Figure 11.10: Stress-strain response of a pebble bed with crushed pebbles. Reproduced from Ref.<sup>66</sup>

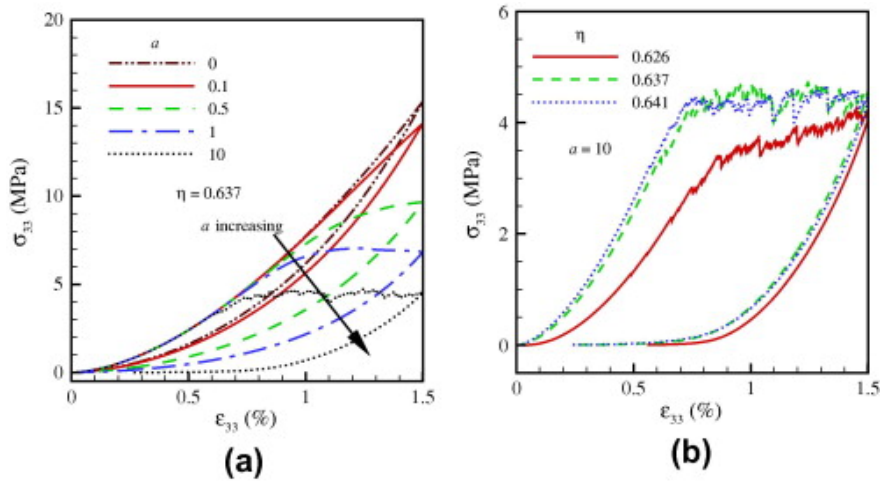


Figure 11.11: Stress-strain response of a pebble bed with crushed pebbles. Reproduced from Ref.<sup>6</sup>

two systems being studied is not comparable. Because we have volumetric energy deposition in our simulations, the total energy pouring into the non-damaged system would be

$$E_h = \frac{q'''' V_{\text{peb}} N}{V_{\text{bed}}} \quad (11.19)$$

where  $N$  is the total number of pebbles of volume  $V_{\text{peb}}$  that exist in the pebble bed of volume  $V_{\text{bed}}$ . After a crushing event, when we remove pebbles, the total amount of energy is

$$E'_h = \frac{q''_{\text{nuc}} V_{\text{peb}} \eta N}{V_{\text{bed}}} \quad (11.20)$$

where  $\eta$  is the percent of crushed pebbles. Obviously then, the ratio of the two heating rates is

$$\frac{E'_h}{E_h} = 1 - \eta \quad (11.21)$$

and the energy deposited is not balanced between a virgin bed and one with crushed pebbles. We will attempt to address this issue.

### 11.3.1 Modeling a Crushed Pebble

In the DEM framework, we are limited to modeling elastic spheres. If we strictly wish to conserve mass between a solid pebble of radius  $R_p$  and the crushed fragments of radius  $R_c$ , then the number of crushed fragments (spheres) per crushed pebble is

$$N_c = \left( \frac{R_c}{R_p} \right)^{-3} \quad (11.22)$$

Thus the number of fragments goes like the inverse of radius ratio to the third power and the number of crushed fragments to represent a single crushed pebble increases rapidly as the fragments shrink.

The relationship between radius ratio and number of fragment particles is given in Fig. 11.12. Note that in the DEM simulation, it is impossible to insert fractions of a particle so the number of fragment pebbles is rounded to the nearest integer in the figure.

In typical DEM simulations that can run within reasonable amounts of time on the machines available to me in this dissertation, a reasonable number of particles is around 10 000. Many more and the run times become impractical for study. To show how quickly the number of particles can quickly get out of hand in a simulation, if we begin with 6 000 pebbles and only 2% break, with a radius ratio of  $R_c/R_p = 0.2$ , the number of pebbles to

Table 11.2: The particle crush fragments,  $N_c$ , necessary to replace a single crushed particle and obey conservation of mass (fragment number is rounded to nearest integer).

$R_c/R_p$	$N_c$
0.2	125
0.25	64
0.3	37
0.35	23
0.4	16
0.45	11
0.5	8
0.75	2

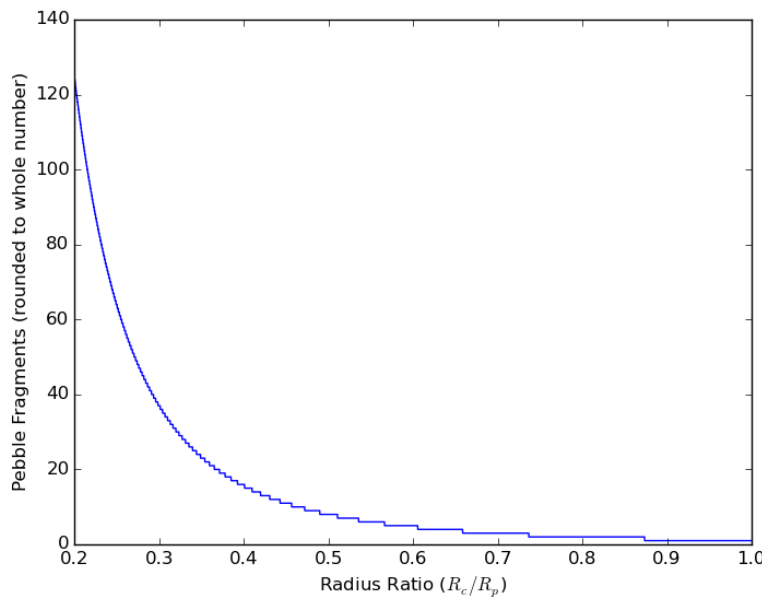


Figure 11.12: Number of fragment pebbles necessary to conserve mass increases rapidly as the size of the radius ratio ( $\frac{R_c}{R_p}$ ) decreases.

be added would be 15 000. The new particle fragments (less the crushed particles) plus the original would require 21 000 particles in the system. In our simulations, we often test the effects on effective thermal conductivity at particle crush amounts of to 10%. For the pebble bed mentioned here, that would mean 81 000 particles in the system and it would be computationally forbidding. The result is that, for computational times, the larger crush fragment radii are desired, *i.e.*  $R_c/R_p > 0.3$ .

However, aside from satisfying conservation of mass, we must physically insert the particle fragments into void space in the simulation domain. During the course of the simulation, when we choose to replace the pebble with the fragments, the only available room is the spherical void left over by the damaged pebble. Other constraint is the smallest sized sphere that will allow the given spheres at most dense packing.

Dense packing of spheres inside a larger sphere is an interesting mathematical problem. [Hugh Pfoertner](#) keeps a compiled list of many solutions for a number of particles; many solutions are his are from Gensane.?

If we consider, for instance, that a radius ratio of  $R_c/R_p = 0.3$  requires 37 particle fragments, then we can also find from Ref.<sup>7</sup> that 37 particles would have to be of radius 0.2406866 to fit into a single sphere of radius of unity. If we define the particle fragment radius as  $R_c$ , the original particle as  $R_p$ , and then radius of sphere necessary to hold the  $N$  fragments as  $R_N$ , we can find a relationship between the volume of sphere  $V_p$  and necessary volume  $V_N$ ,

$$r_1^* = \frac{R_c}{R_p} \quad (11.23)$$

and

$$r_2^* = \frac{R_c}{R_N} \quad (11.24)$$

then

$$R_N = R_p \frac{r_1^*}{r_2^*} \quad (11.25)$$

thus

$$\frac{V_N}{V_p} = \left( \frac{r_1^*}{r_2^*} \right)^3 \quad (11.26)$$

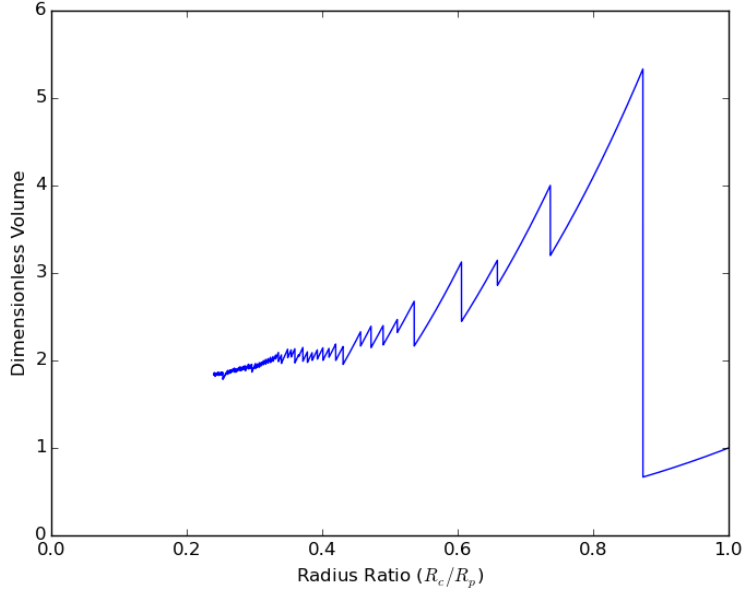


Figure 11.13: The volume necessary to house the particles of different radius ratios decreases toward unity as the radius ratio decreases. It is greater than 5 times the volume for large  $r_1^*$ .

If we choose a linearly spaced distribution of  $r_1^*$  between 0 and 1, we can then find how many  $N_c$  particles are necessary to conserve mass, then from the  $N_c$  particles we can find from the database of sphere packing solutions the size of sphere that would be necessary to fit the  $N_c$  particles. The calculations are carried out and shown in Fig.11.13. The data in Ref.<sup>?</sup> does not go above 72 spheres so we are limited to radius ratios above about  $r_1^* > 0.24$ .

The plot shows that for particle fragments of reasonable numbers ( $N_c \approx 20$ ), the volume necessary to fit the number of volume-conserving particles is greater than double the volume of the original sphere!

Therefore from the point of view of having the physical space to insert the fragments, smaller sized fragments is ideal. To insert the few number of large particles would require disrupting the packing in the region of the damaged particle.

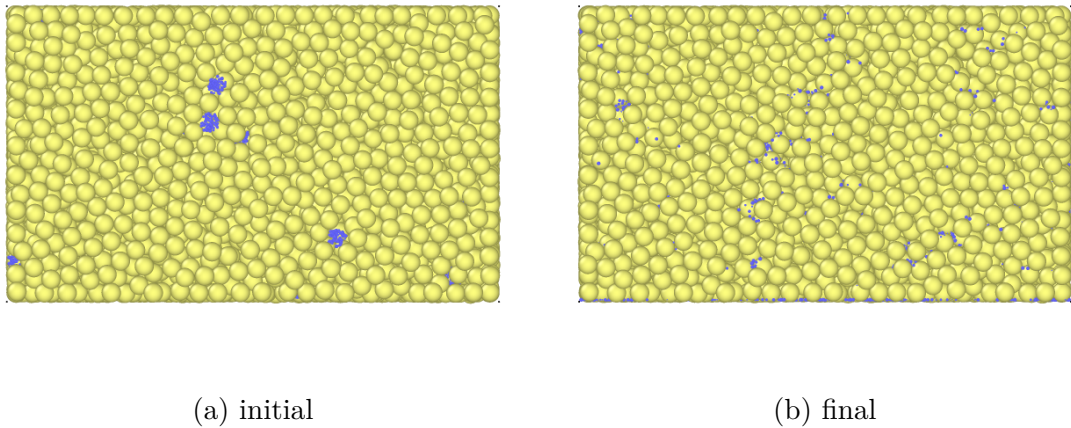


Figure 11.14:  $N_c = 8594$ ,  $N_{\text{tot}} = 15430$ ,  $R^* = 0.20$ . Side view of the packing arrangement and settling for different crush fragment sizes. The small crush fragments migrate far through the height of the bed. The yellow particles are the original pebbles and the blue are fragments inserted into the system after pebble crushing.

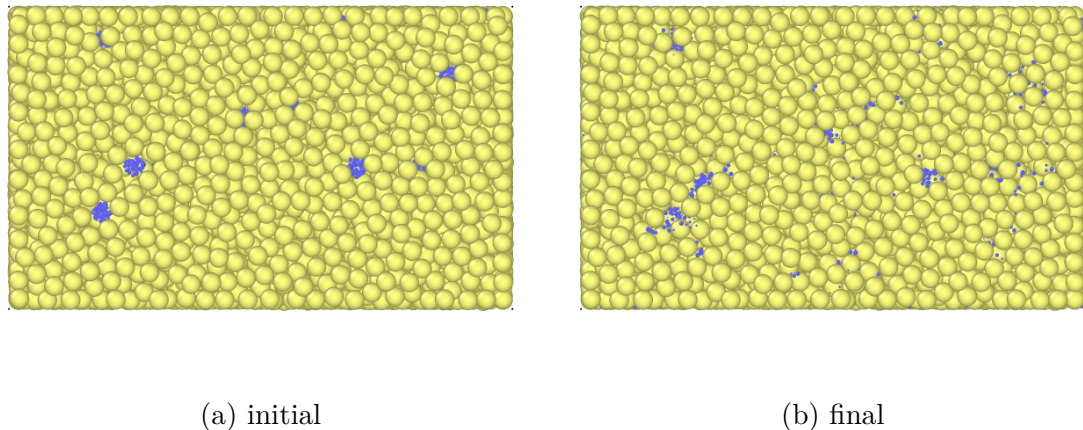


Figure 11.15:  $N_c = 4400$ ,  $N_{\text{tot}} = 11222$ ,  $R^* = 0.25$ . Side view of the packing arrangement and settling for different crush fragment sizes. The small crush fragments migrate far through the height of the bed. The yellow particles are the original pebbles and the blue are fragments inserted into the system after pebble crushing.

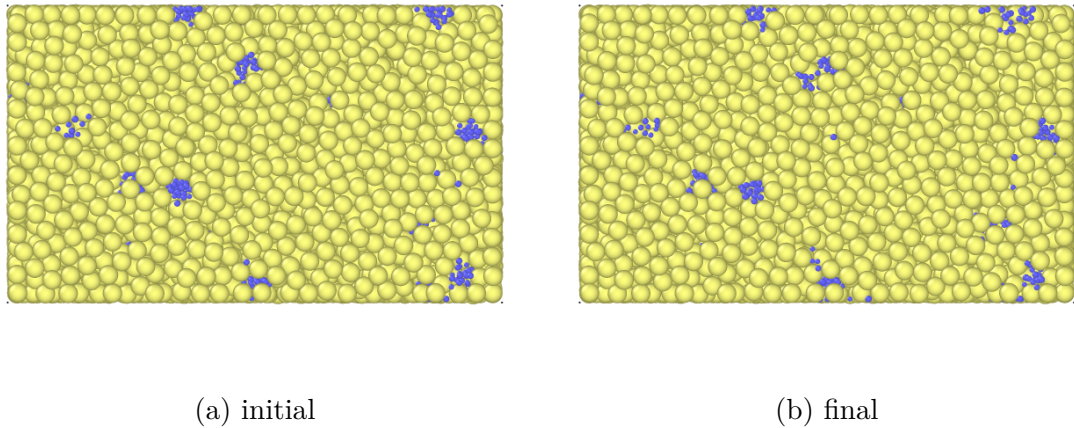


Figure 11.16:  $N_c = 1603$ ,  $N_{\text{tot}} = 8393$ ,  $R^* = 0.35$ . Side view of the packing arrangement and settling for different crush fragment sizes. The bigger fragments remain largely in place. The yellow particles are the original pebbles and the blue are fragments inserted into the system after pebble crushing.

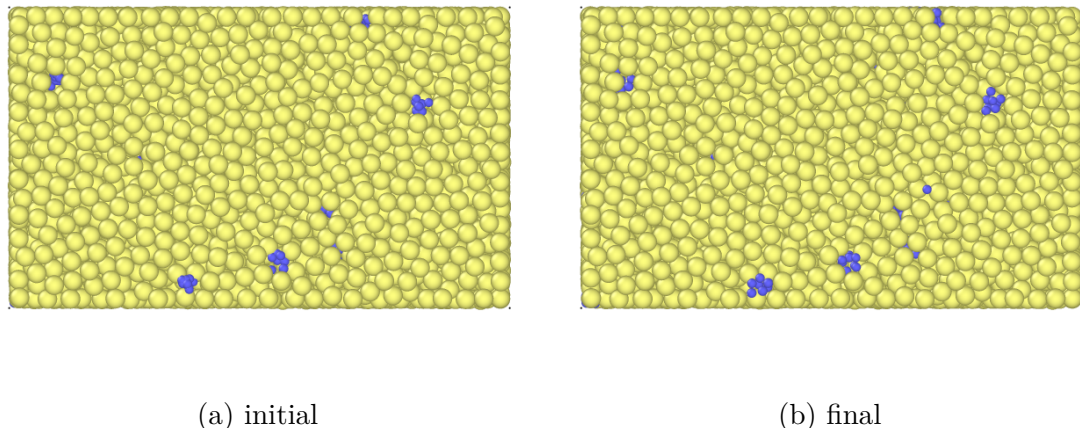


Figure 11.17:  $N_c = 550$ ,  $N_{\text{tot}} = 7358$ ,  $R^* = 0.50$ . Side view of the packing arrangement and settling for different crush fragment sizes. The bigger fragments remain largely in place. The yellow particles are the original pebbles and the blue are fragments inserted into the system after pebble crushing.

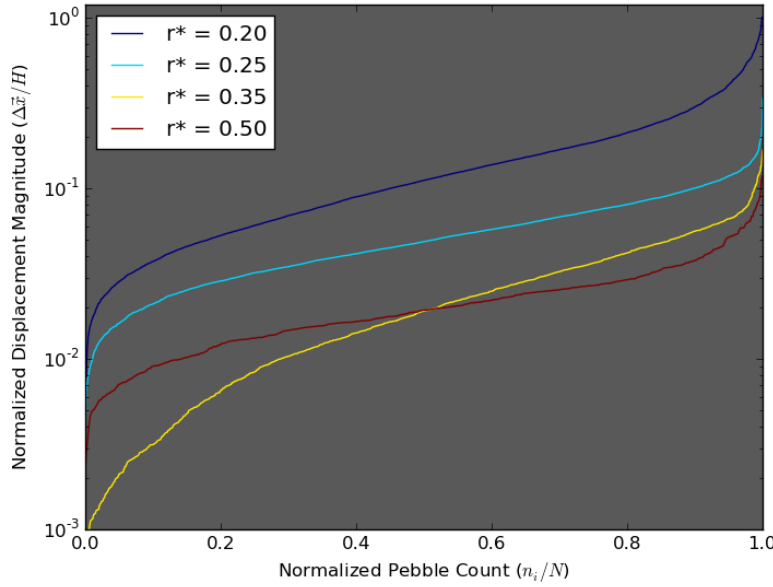


Figure 11.18: After the particle fragments are inserted into the system they re-settle due to gravity and inter-particle forces. The small fragments travel much further throughout the bed than the large fragments.

Lastly, in this packing study we look at the displacement of the particle fragments after insertion into the system and as they come to rest in a steady state. In the images of Figs. 11.14, 11.15, 11.16, and 11.17, we see the initial packing of new particle fragments (in blue) settle into the interstitial gaps of the packing structure of original pebbles (yellow).

The settling of crushing fragments is also visualized in Fig. 11.18. In this figure, the magnitude of displacement for all the crushed fragments is recorded based on the change between initial insertion location and final resting place. The displacement of the fragments is normalized against the height of the pebble bed,  $H$ . The fragments with  $r_1^* = 0.2$  are seen to travel, on average, 10% of the height of the pebble bed before coming to rest; some of them travel more than the entire height of the bed! In contrast, the particle fragments of size  $r_1^* = 0.35$  and  $r_1^* = 0.5$  travel only about 1% of the height of the bed before coming to rest.

The impression arises that the large displacement magnitudes of the small crush frag-

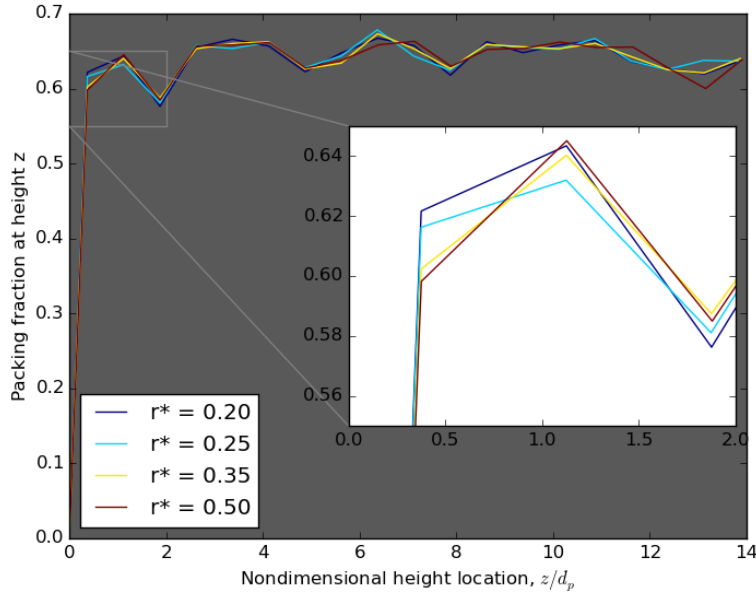


Figure 11.19: For only 1% of crushed pebbles, the re-settling of small pebble fragments has a small effect on the overall packing fraction of the pebble bed. In the inset, the main influence is seen in the slight increase of packing fraction within the first pebble radius of the floor.

ments would result in an overall less-dense bed with large increase in packing fraction near the floor where pebbles settle. In Fig. 11.19, the packing fraction of the four different pebble beds is given.

## 11.4 Stability study

As mentioned when the integration algorithm was introduced in § 7.2, the velocity-Verlet algorithm is a computationally efficient, second-order accurate means of updating the kinematics of all the particles in the ensemble.<sup>55</sup> The timestep of the integration, however, must often be very small to ensure that it is less than the time taken for a pressure wave to propagate through the particle. The timestep is further constrained by the quasistatic assumption used to derive the Hertzian contact force such that inertial and relaxation effects may be neglected.<sup>10</sup> We will also show that, in order to avoid heat energy to propagate further than a single pebble during a single timestep, the thermal timestep requirement is orders of

magnitude larger than the mechanical timestep equivalent. And that the overall minimum timestep is thus driven by the mechanical stability.

In tandem with the requirement on very small timestep, the thermal time-constants in the ceramic breeder zones can be many hundreds of seconds. These two conditions seem to conspire to force an unacceptably large requirement on the number of timesteps for a thermal DEM simulation and thus make numerical experiments impractical.

In this section we will analyze the calculation of a critical timestep based on the speed of a Rayleigh wave propagating along the surface of a particle. Then, with that knowledge in hand, we will argue for scaling certain physical properties to allow for faster simulations without sacrificing fidelity to the real physics of the problem.

#### 11.4.1 Critical Dynamic Timestep

If we wish to choose a timestep sufficiently small such that a pressure wave originating from the contact of one particle does not propagate to other neighboring particles during the timestep, we must choose a timestep smaller than the critical timestep defined by Rayleigh wave traveling through the solid.

When a force is applied to the surface of an elastic body, the force propagates along the surface at the wave speed first solved by John William Strutt, 3rd Baron Rayleigh<sup>73</sup> (when he wasn't discovering the scattering phenomenon explaining why the sky is blue or winning the Nobel prize for discovering Argon),

$$u_{\text{Ra}} = K \sqrt{\frac{G}{\rho}} \quad (11.27)$$

where, again,  $G$  is the shear modulus and  $\rho$  is the density of the elastic material. The  $K$  coefficient is a complicated function coming from Rayleigh's solution but can be approximated as<sup>82</sup>

$$K = 0.1631\nu + 0.876605 \quad (11.28)$$

which is valid for realistic values of Poisson's ratio,  $\nu$ , of elastic materials. From the inverse of the Rayleigh wave frequency, we can directly find a timestep for Rayleigh waves on a sphere of radius,  $R$ ,

$$\delta t_{\text{Ra}} = \frac{\pi R}{u_{\text{Ra}}} \quad (11.29)$$

When we write this for any particle,  $i$  in the ensemble (exchanging the shear for elastic modulus),

$$(\delta t_{\text{Ra}})_i = \frac{\pi R_i}{0.1631\nu_i + 0.876605} \sqrt{\frac{2(1 + \nu_i)\rho_i}{E_i}} \quad (11.30)$$

We allow for the particles in the system to have varying density, elastic modulus, and size. Therefore the critical timestep for the entire system is governed by the minimum value of any particle's Rayleigh timestep.

$$\delta t_c = \min_{\forall i} [(\delta t_{\text{Ra}})_i] \quad (11.31)$$

The ceramic materials identified for breeders have relatively high Young's moduli, on the order of  $10^{10}$ Pa. The smallest radius will be on the order of  $10^{-4}$ m. The ceramic density is approximately on the scale of  $10^4$ kg/m<sup>3</sup>. These values lead to a necessary timestep of

$$\delta t_c \propto 10^{-7}\text{s} \quad (11.32)$$

For a simulation that may last several hundreds of seconds of real time, this then requires more than  $10^9$  timesteps. If we have  $10^4$  particles in the simulation, each having their position integrated over a billion times, it becomes obvious that computational time is a major issue for our simulations of nuclear heating of ceramic breeder pebbles. If we are able to reduce

the critical timestep (while perhaps decreasing the simulation time), the simulations will be much more practical for research use.

### 11.4.2 Critical Thermal Timestep

In § 6.2.1, we introduced the dynamics of heat transfer between contacting particles in an ensemble. As we integrate the energy of an individual particle in time, we must also ensure that energy would not propagate through a particle faster than a single timestep can capture. In analogy to the critical timestep for mechanical stability (e.g. Eq.11.29), we write for particle  $i$ ,

$$\delta t_{\text{Bi}} = \frac{\rho_i C_i V_i}{H_c} \quad (11.33)$$

where  $\rho_i C_i V_i$  represents the inertial resistance to changing the temperature of  $T_i$  and the conductance,  $H_c$  represents the speed at which energy is delivered to  $T_i$  from contact conduction. Then from the definition of  $H_c$  we have given for smooth elastic spheres, this is also written as

$$\delta t_{\text{Bi}} = \frac{(4/3)\pi R_i^2 \rho_i C_i}{2k^*} \frac{R_i}{a} \quad (11.34)$$

For the material properties of lithium ceramics, as discussed for mechanical stability, we can expect

$$\frac{(4/3)\pi R_i^2 \rho_i C_i}{2k^*} \approx \frac{(10^{-4})^2 10^4 10^3}{10^0} = 10^{-1}$$

But from the requirements on Hertz theory in § 5, we have required that  $\frac{a}{R_i} \ll 1$ . Thus the timestep for stability in the energy calculation is utterly negligible compared to the mechanical stability.

Vargas and McCarthy<sup>95</sup> make similar arguments, giving the criteria as,

$$\frac{dT_i}{T_i - T_j} \ll 1 \quad (11.35)$$

and too note that the timestep requirement for thermal calculations are orders of magnitude less restrictive than the analogous restriction of the particle dynamics.

Thus we can be confident that any timestep chosen for dynamic stability in the DEM simulation will automatically satisfy the timestep for thermal stability.

#### 11.4.3 Simulation Acceleration with Scaled Material Properties

We rewrite Eq. 11.30 to facilitate a discussion on the parameters. Isolating each material term (neglecting the Poisson ratio) gives,

$$\delta t_c \propto R_i \times \rho_i^{1/2} \times E_i^{-1/2} \quad (11.36)$$

Part IV

# **Studies of Pebble Bed Thermophysics, Mechanics, & Morphological Changes**

## CHAPTER 12

# DEM Study on the Evolution of Effective Thermal Conductivity of a Pebble Bed Experiencing Pebble Crushing

The discrete element method (DEM) is used by many ceramic breeder researchers to model the interaction of individual pebbles in an ensemble in an effort to obtain a more detailed understanding of pebble beds than is possible with experimental measurements of effective properties. For example see Refs.<sup>4,6,40,59,93,105</sup>

## 12.1 DEM Study: Effective Conductivity with Pebble Damage

The discrete element method has been used for studies in a variety of fields for studying inter-particle forces and the homogeneously distributed force networks that arise in packed beds (for example, see Ref.<sup>64</sup>). The discrete element method was also used in the fusion community to attempt to model crushing initiation and propagation.<sup>6,106,107</sup> They too observed that a relatively few number of high-force networks, distributed throughout the bed supported the external mechanical loads. The even distribution of the force networks was used to defend the development of a probability-based predictor for crushing. We make use of the probability argument of Zhao *et al.* for the current study.<sup>107</sup> Their basic premise is that probability distributions of strength curves for pebble crushing have been observed (see, for example crush loads of Ref.<sup>87</sup>). Then in DEM models, a probability distribution of inter-particle forces are also observed. Overlaying the two probabilities resulted in seemingly random

locations of pebbles satisfying the damage criteria – not strictly along the high-force chains running through packed beds.

We apply the theory of Zhao *et al.* in the following manner. If pebbles are crushed in random locations, we may de-couple the task of predicting pebble damage (*i.e.* finding the mechanical or thermal load that causes a pebble to fail) from the task of modeling the ramifications of pebble crushing. Experiments on crushing single, brittle pebbles reveal that there are a number of failure modes.<sup>99</sup> At one end, the pebble may simply crack and continue to hold a load for some time. At the other extreme, a pebble may crush practically into a dust. We concern ourselves with the latter for this study. When a pebble in our simulation has been flagged for damage, we remove the pebble completely from the ensemble and then allow the remaining pebbles to rearrange to compensate for the lack of equilibrium on their contact forces.

In our model, we begin with a starting point of a packed bed and then simply flag pebbles at random for crushing. The removal disrupts the meta-static state of the ensemble and the remaining pebbles re-settle due to gravity and the imbalance of contact forces. In reality, the ceramic pebbles generally break into just a few large pieces that remain in the system, a simulation attempting to model such a crush event is covered in § 15.

### 12.1.1 Model Setup & Methodology

We analyze a three-dimensional pebble bed consisting of mono-dispersed particles of diameter  $d_p$ . The particles are constrained by rigid  $y - z$ -planes at locations of  $\frac{x}{d_p} = \pm 10$  (the walls of our container). There are periodic boundary conditions in the  $y$ -direction located at  $\frac{y}{d_p} = \pm 7.5$ . Gravity acts in the negative  $z$ -direction and the particles are resting on a rigid  $x - y$ -plane at  $z = 0$  (the floor of the container) and held from the top by an  $x - y$ -plane at  $\frac{z}{d_p} = 30$  (the roof of the container). We pack to  $\phi = 64\%$  and, given the volume, have 11000 particles. The volume was chosen to represent the long, tall, narrow channels seen in many solid breeder module designs.<sup>21,31,72</sup>

Table 12.1: Maximum load and nominal tension.

E (GPa)	$\nu$	k (W/m-K)	C (J/kg-K)	$\alpha$ (1/K)
126	0.24	2.5	1156	$15 \times 10^{-6}$

For this study, the material properties were chosen to represent lithium metatinatate pebbles. All the properties come from Ref.<sup>43</sup> They are summarized in Table 12.1

In the first attempt at packing pebbles into the system, we begin with a common starting point of a filled, lightly packed volume of 10 550 pebbles. We simulate pouring the pebbles into the volume by initializing them into the system from a height of  $\frac{z}{d_p} \approx 50$  and allow them to fall under the influence of gravity (see Fig. 12.1). We pack the pebbles into a higher packing fraction by means of oscillating the walls as if the pebble bed were sitting on a vibrating plate. This was to imitate the vibration packing technique done in our experimental lab when testing pebble beds in the uniaxial compression test stand. The vibration scheme was able to slowly densify the packed bed but, owing to the very small timestep of the simulation, the simulation times were impractically large to approach a packing fraction greater than  $\phi = 60\%$ .

In the end, a simpler pack-relax method was used instead. In this method  $N$  particles are inserted into the volume such that we have precisely the packing fraction we desire (in this case,  $\phi = 64\%$  so  $N = 11000$ ). The pebbles are placed at random into the volume and are allowed to artificially overlap – often by a great deal ( $\delta \sim R_p$ ). The overlap they experience would normally cause such an enormous force (integrating into an enormous velocity) that the pebbles would all explode out of the bed at the first step in time integration. We avoid such a catastrophic scenario with a relaxation scheme where we truncate the displacement of any pebble per timestep that is integrated from the force. The truncated displacement is very small and allows the pebbles to slowly move away from each other and into a static equilibrium as the artificial overlap is reduced. Once the pebble bed comes to rest, we remove

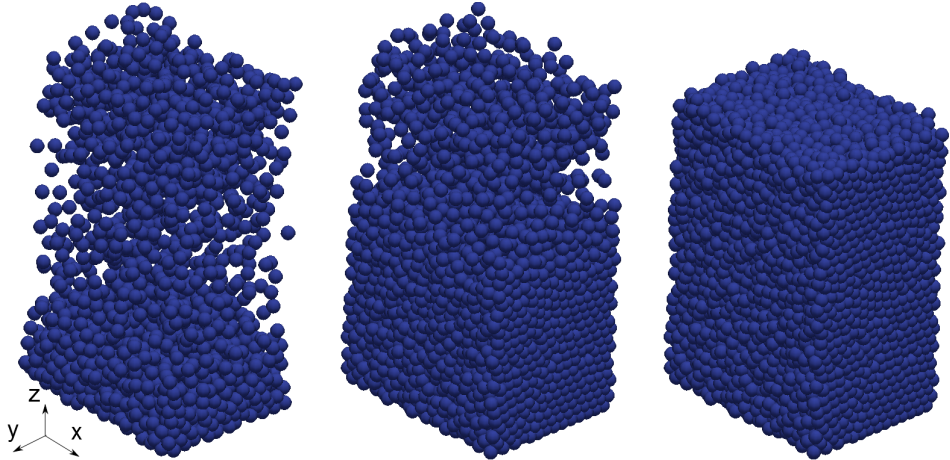


Figure 12.1: Demonstrating the pouring process of  $N = 10550$  pebbles into the control volume with at an early time (left), when it is nearly filled (middle) and after the pebbles have settled to negligible kinetic energy (right).

the relaxation (limiting displacement command) and allow standard integration of contact forces with the velocity-Verlet algorithm (see § 7.2.4). The pack-relax scheme allowed for obtaining desireable, highly repeatable packing fractions for all pebble beds. Once the pebble bed was packed into an initial condition, the simulation state was saved and used as a starting point for the numerous ‘crushed’ cases to be described later.

In this first study, we model pebble crushing without considering why the particular pebble should be cracking. In the model we randomly select pebbles from the ensemble, regardless of forces acting upon the pebble, and delete them entirely from the system. When a pebble is removed, the neighboring pebbles react due to the imbalance of forces, and the bed settles into a new configuration. We differentiated the failed beds by their percentage of failed pebbles:  $\eta = \text{number of failed pebbles per original ensemble size}$ . For the baseline case and for beds after failing, we apply the heating routine described next.

To simulate the conditions of a solid breeder in a fusion reactor, where the heat is removed from the pebble bed via contact to the containing structure, we assigned a constant temperature of  $T_c$  to the vertical walls. Nuclear heating of the pebbles is simulated through a constant source term on each pebble. A representative heating rate of  $Q_s = q_p''' V_p$ , where

$q''_p = 8 \text{ MW/m}^3$ . The heating cycle runs until a thermal steady state is reached. Based on a measurement of the total thermal energy of the bed,  $E_T = \sum_i^N m_i C_i T_i$ , steady-state is determined as  $\frac{dE_T}{dt} = 0$  within a specified tolerance. Once at steady state, we analyzed thermal and mechanical characteristics of the pebble bed: effective thermal conductivity, average coordination number, temperature profiles in the bed, and inter-particle contact forces.

Based on the boundary conditions to our system, we establish heat transfer that is symmetric and one-dimensional in the  $x$ -direction from  $x = 0$  to the walls at  $\frac{x}{d_p} = \pm 10$ . As we will show, the pebble bed has very little variation of forces and temperatures in the  $y$ -direction due to the periodic boundary condition at the edges of the domain. Gravity effects are minor in the overall heat transfer and induce only a slight  $z$ -dependency to the results. We take advantage of this nature of our pebble bed to find the effective conductivity from an analytic, one-dimensional test case.

### 12.1.2 Effective Thermal Conductivity from Analytic Analogy

Assuming a one-dimensional pebble bed, to find an effective conductivity, we step back into a continuum mechanics formulation where the pebble bed can be represented as a slab of solid material. We can analytically solve for the temperature equation in a slab with heat generation, symmetry about the centerline, and a constant boundary temperature condition.

At steady-state, the temperature of a material with constant temperature boundary conditions ( $T(L) = T_s$ ), constant thermal conductivity ( $k_{\text{eff}}$ ), and nuclear heating ( $q''$ ) obeys the following equation

$$0 = \frac{d^2T}{dx^2} + \frac{q''}{k_{\text{eff}}} \quad (12.1)$$

We introduce a non-dimensional temperature

$$\theta = \frac{T(x) - T_s}{T_0 - T_s} \quad (12.2)$$

where  $T_0$  is the temperature at the centerline of this slab (a value we will find momentarily).

The length is non-dimensionalized as

$$x^* = \frac{x}{L} \quad (12.3)$$

Thus we can re-write Eq. 12.1 as

$$0 = \frac{d^2\theta}{dx^{*2}} + G \quad (12.4)$$

where

$$G = \frac{q'''L^2}{k_{\text{eff}}(T_0 - T_s)} \quad (12.5)$$

In the non-dimensionalized form, the solution is revealed to be purely geometric,

$$\theta = 1 - x^{*2} \quad (12.6)$$

. as  $T_0 - T_s = \frac{q'''L^2}{2k_{\text{eff}}}$ . We will use the non-dimensional temperature solution of Eq. 12.6 to prove our one-dimensional assumption of heat transfer is justified for the pebble beds.

We note that in this continuum mechanics formulation, we are assuming that the nuclear source,  $q'''$  term is applied evenly over the entire volume. In our DEM formulation, our source term applies to a single pebble. To find the effective thermal conductivity of our ‘slab’ of pebble bed, we must reconcile this discrepancy. This is accomplished with the exchange of

$$q''' = \frac{Q_{\text{tot}}}{V_{\text{tot}}} = \frac{Q_s N}{H \cdot L \cdot W \cdot d_p^2} \quad (12.7)$$

where the pebble bed volume is given by the height,  $H$ , width,  $W$ , and length,  $L$ , and  $Q_s$  is the source term on each pebble in the DEM ensemble.

From the solution of Eq. 12.4, we find the effective conductivity to be

$$k_{\text{eff}} = \frac{q'''L^2}{2(T_0 - T_s)} \quad (12.8)$$

and when we replace the heat generation term with Eq. 12.7, and use the bed dimensions as given in § 12.1.1, this is written as

$$k_{\text{eff}} = \frac{Q_s N}{180(T_0 - T_s)d_p} \quad (12.9)$$

We will use this formulation of Eq. 12.9 to analyze and compare the pebble beds of this study.

### 12.1.3 Results

The aim of this study was both to discover the impact of pebble failure on thermo-mechanical properties as well as determine the impact as a function of the number of failed pebbles. To satisfy the latter, we created beds with  $\eta = 1\%, 3\%, 5\%, 10\%$ , and  $15\%$  of pebbles failed.

We plot Eq. 12.6 against the non-dimensionalized temperature profiles coming from the steady-state DEM simulation in Fig. 12.2. We find that all our models had a nearly perfect match to a one-dimensional prediction, validating the calculation of effective thermal conductivity in this study. Furthermore, the profiles adhering to the one-dimensional curve also allows us to find the effective conductivity of each bed from applying Eq. 12.9, which was derived from the one-dimensional assumption.

One concern we had for pebble crushing, was the phenomenon of ‘jamming’ during re-settling that would possibly leave pebbles isolated from their neighbors (apart from those they are resting upon). Jamming can happen when a bridge of pebbles have a balance of forces without strong or any contact to a pebble below them. The pebble under the bridge then only has light contact with the pebbles upon which it is resting. Such an isolated pebble would have no strong pathway for heat transfer and heat up much higher than that of its neighbors. Evidence of pebble isolation is apparent in hot individual pebbles above the grouped curve in Fig. 12.2.

Because the 10% and 15% cases have such high temperatures, we show only the 0-5% crushed together in Fig. 12.3

The individual hot pebbles in Fig. 12.2 are also indicative of the shortcomings of the discrete element method for modeling solid breeders in fusion reactors. The flowing purge gas in actual solid breeders would likely not permit such thermal isolation of pebbles. Even if a pebble had no physical contact with neighboring ones, it would still transport energy via conduction and advection of the helium gas. This will be addressed again and in more detail in § 13.2.

In order to calculate an effective conductivity of the pebble bed, we must find an average

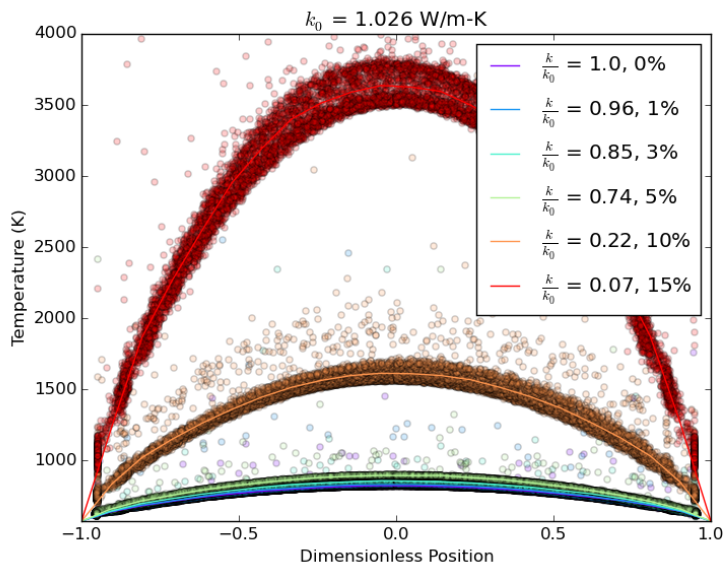


Figure 12.2: The nondimensional temperature profiles for each test case follow the theoretical shape of a one-dimensional, constant  $k$ , continuum solution.

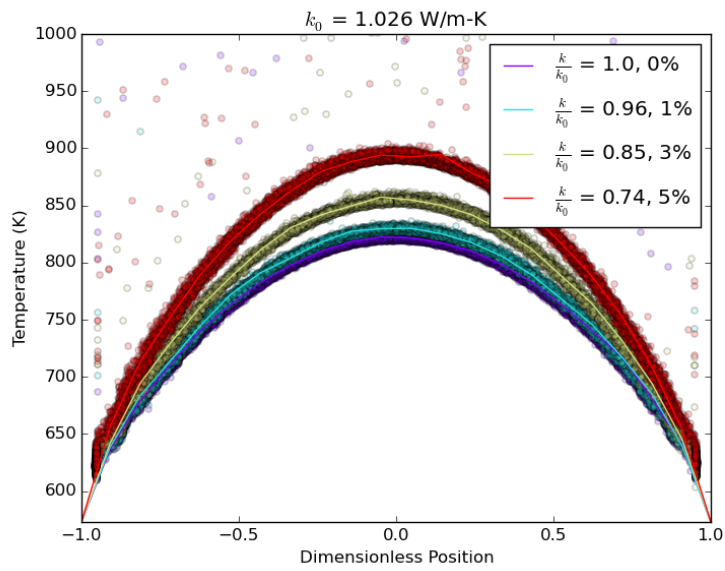


Figure 12.3: The nondimensional temperature profiles for the test cases up to 5% crushed pebbles.

temperature profile through the bed to compare with Eq. 12.6 and thus employ Eq. 12.9. We compare steady-state temperature profiles in the test beds against the one-dimensional, non-dimensional temperature profile. Average values of the bed, along the  $x$  direction, are generated via averaging temperatures in bins. We create bins that are volumes slices of width  $\Delta x$  that extend through the limits of the  $y$ - and  $z$ -directions. We then find the  $n$  pebbles residing in the slices and take the mean value of their temperatures. The average, given by Eq. 12.10, is also given in Fig. 12.2. The binned average temperature is

$$\langle T \rangle = \frac{1}{n} \sum_i^n T_i \quad (12.10)$$

Using the volume slices, we also find the average coordination number,

$$\langle Z \rangle = \frac{1}{n} \sum_i^n Z_i \quad (12.11)$$

and average contact force,

$$\langle F^{1/3} \rangle = \frac{1}{n} \sum_i^n F_{n,ij}^{1/3} \quad (12.12)$$

In Eq. 7.14 of § 7.3, we see that at steady-state, the energy input by nuclear heating must be balanced by the transport of heat out of a pebble into its neighbors. Inter-particle heat transfer is dictated by the number of neighboring contacts, temperature difference between pebbles, and the thermal conductance,  $H_c$ , through the contact area. The thermal conductance (see Eq. 7.16) is itself a function purely of material properties (which are essentially constant here) and the force at the contact, going as  $H_c \propto F_{n,ij}^{1/3}$ . Thus, we write the net heat out of a pebble at steady state as a function of the three variables,

$$Q_{\text{net}} = f(Z, F_n^{1/3}, \Delta T) \quad (12.13)$$

The coordination number and contact forces are features of the packing structure in the packed bed that we can analyze to discover what happens to the heat flux between pebbles when the bed experiences crushed particles. Conversely, the  $\Delta T$  between two pebbles is the effect of the thermal transport (i.e. leading to higher bed temperatures such as those of

Fig. 12.2). We will first analyze the changes to the coordination numbers of pebbles in the ensemble as pebbles crush.

In Fig. 12.4 we plot the data for all pebbles in the ensemble as well as the binned average (Eq. 12.11). Clearly, there are fewer average contacts per pebble in the ensemble after failure; At 15% crushed the coordination number drops by roughly 30%. But this alone can not account for the reduction in  $k_{\text{eff}}$  by 93% for the same amount of crushed pebbles. Next we look to the normal contact forces between pebbles in the bed.

The normal contact forces between pebbles are plotted in Fig. 12.5. A dramatic reduction in the normal forces is seen after many of their neighbors are crushed and are removed from the system. From the baseline down to the 15% failed case, the contact forces are reduced by about a factor of 10 - similar to the reduction in effective conductivity.

The effective thermal conductivity was found for all of our pebble beds, via Eq. 12.9, then normalized against the conductivity of the baseline ensemble ( $k^* = k/k_0$ ). The average coordination number of the beds and average normal contact forces were also found. Another way of describing a pebble bed is with the packing fraction,  $\phi$ . In Fig. 12.6, we collect all these values (and normalize them against the baseline case) to provide a direct comparison to their changes as a function of crushed pebbles. When 15% of the pebbles are crushed in a pebble bed, the effective conductivity has fallen all the way to only  $k^* = 0.07$ . This large reduction is especially important in light of the already poor thermal management of virgin pebble beds that, even in helium environments, have been experimentally measured at only approximately 1 W/m-K (see, e.g., Refs.<sup>69,78</sup>). The only parameter to have similar reductions in value is the average normal contact force, a value which is seen to follow closely to the curve of effective conductivity. Thus we conclude that the single most important factor for determining the effective thermal conductivity in these pebble beds is the normal contact forces between pebbles; a force which decreases sharply as pebbles are crushed in the system.

The large reduction in normal contact force (which leads to a large reduction in effective conductivity) is explainable based on the experimental setup of our numeric model. In our system, we had rigid walls in the  $x$  and  $z$  directions. These walls did not change after the

substantial number of pebbles were crushed and removed. After the 15% crushing event, the pebble bed appeared as Fig. 12.7a. A massive re-arrangement proceeds from the crushing event. As the pebble bed heats up, the thermal expansion of the pebbles is unconstrained as there exists an average of two pebble diameter gap above the pebbles to the top of the container. Numerically there is no limit to the pebble temperatures (phase change and sintering is not incorporated into the DEM calculations) so the pebbles heat and swell until coming into contact with the top wall, at which time they begin to press into one another (though lightly) to allow thermal conduction. The pebble bed after swelling is shown in Fig. 12.7b.

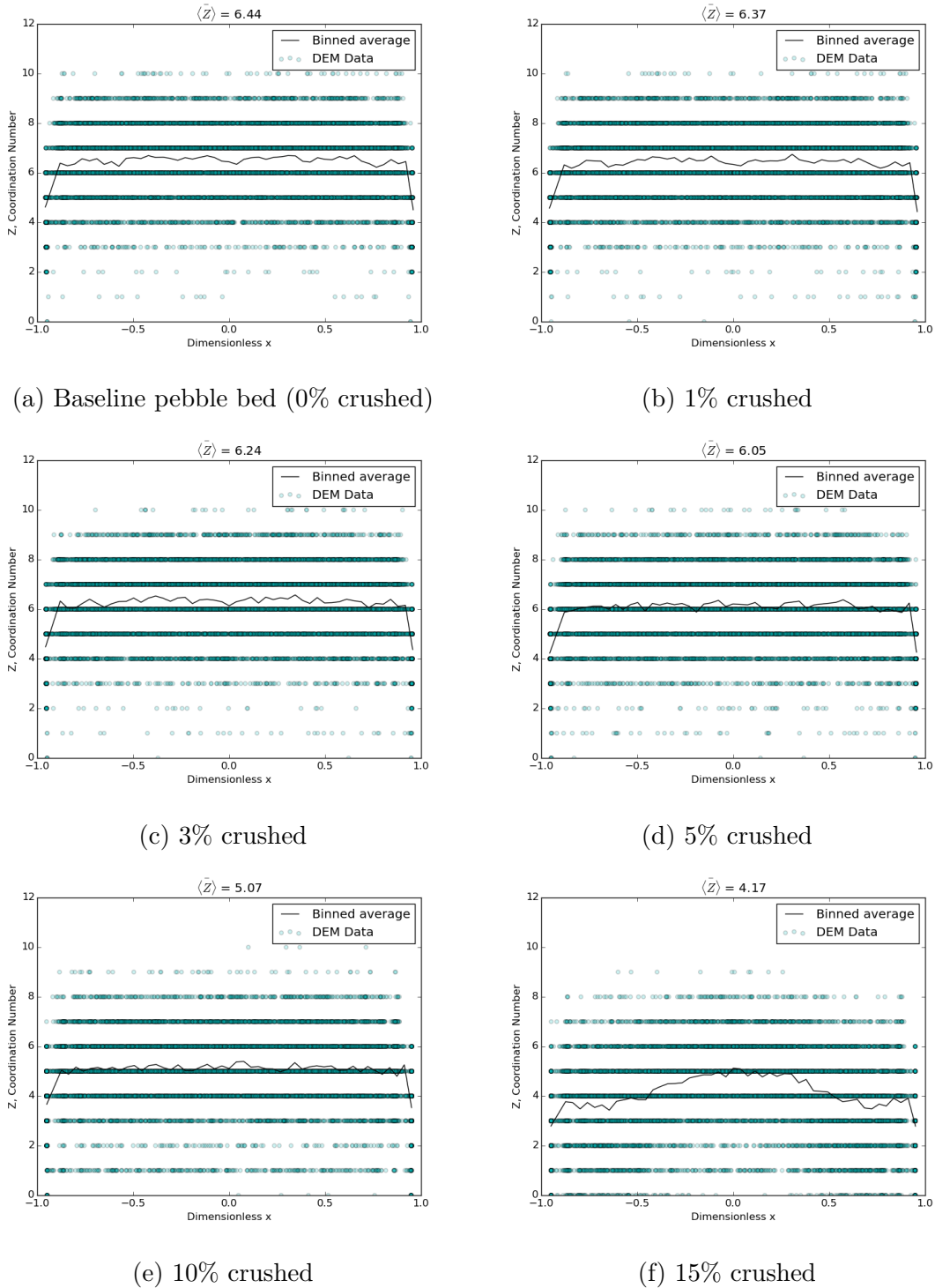
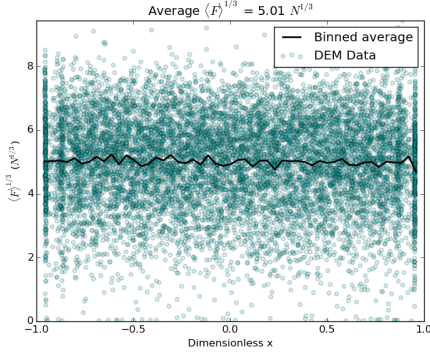
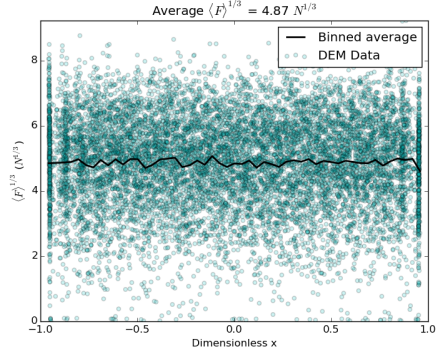


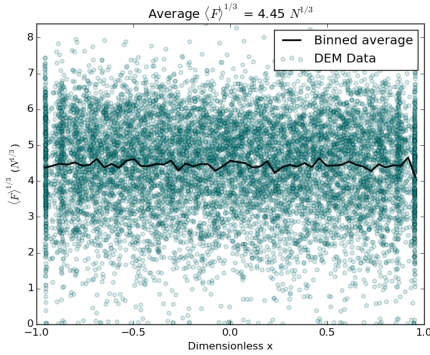
Figure 12.4: The average coordination number decreases slowly as the number of broken pebbles in the ensemble increases.



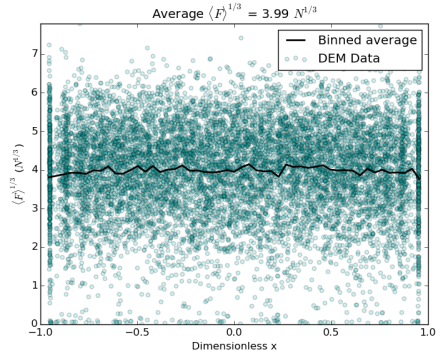
(a) Baseline pebble bed (0% crushed)



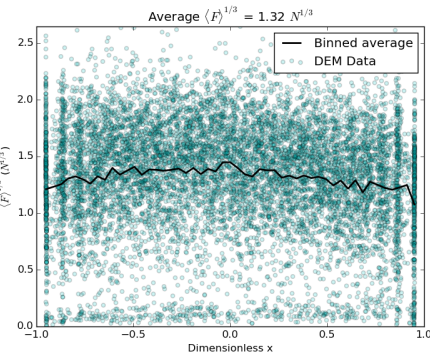
(b) 1% crushed



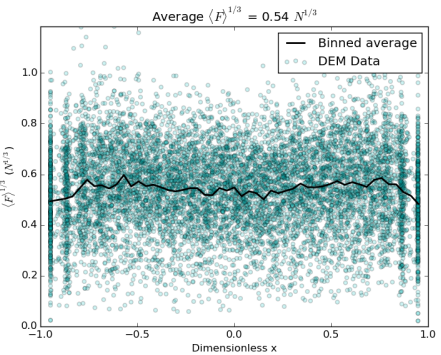
(c) 3% crushed



(d) 5% crushed



(e) 10% crushed



(f) 15% crushed

Figure 12.5: As pebble beds experience massive amounts of crushed pebbles (>5%), the contact forces in the ensemble (after heating to steady-state) show dramatic reductions in value. Note the change of scale on the figures from the baseline case to the 15% crushed case.

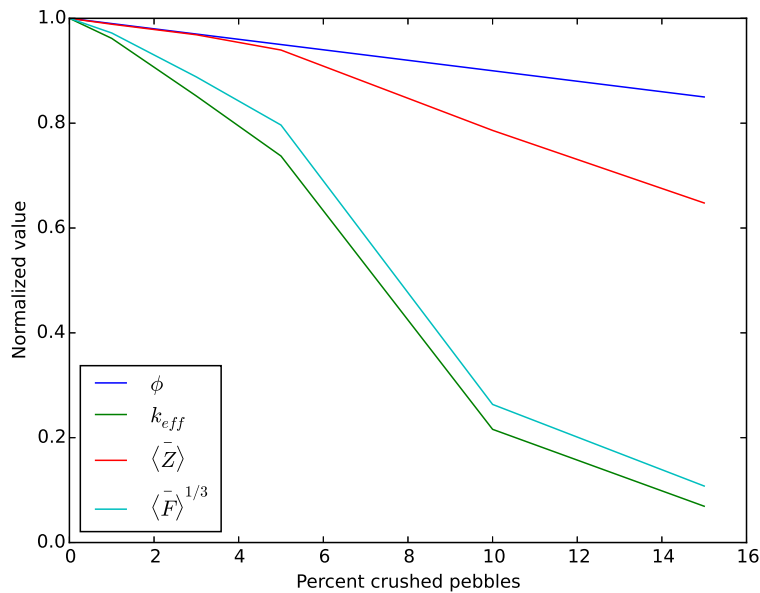


Figure 12.6: The normalized effective conductivity drops much more rapidly than the normalized packing fraction,  $\phi$ , while pebbles are crushed. The effective conductivity follows with reduced normal contact forces.



(a) Side-view of the pebble bed after reset- (b) Side-view of the pebble bed after heating  
tling from the crushing event, before heating.

Figure 12.7: In (a) we see the pebble bed after 15% of the pebbles have been crushed (removed) and then after the heating cycle in (b). The gap formed after crushing is completely filled by swelling pebbles.

## 12.2 Conclusions

The results shown in Figs. 12.5 and 12.4 demonstrate that the heat transfer through a pebble bed is simultaneously a function of both the coordination number and inter-particle contact forces. The average values of both of these parameters reduced as pebbles in the bed were crushed. Interestingly, when a pebble bed has lower overall inter-particle contact forces such as what we see when pebbles are crushed, we would predict fewer pebbles are likely to break. This result implies that pebble breakage is self-dampening; as pebbles begin to break the ensemble quickly relaxes and avoids future pebble failure. So while in this study we induced failure up to  $\eta = 15\%$  without a concern for predicting if such a large amount would break, such large values may not occur in real beds during operation of a fusion reactor.

The first study of this dissertation established the groundwork of the DEM modeling to be carried out in the other studies. We simulated a pebble bed with a specified fraction of the pebbles crushing during operation; then determining the repercussions of the missing pebbles as they affect the macroscopic property of effective thermal conductivity. We used the assumption of homogeneous, random locations of pebble failure to induce a failure routine without requiring external loads on the bed to actually induce the pebble crushing. After heating to a steady-state, an effective thermal conductivity was calculated for the pebble bed. The results show that large amounts of pebble failure correspond to large decreases in the conductive transport of energy through the pebble bed. The increase was due primarily to a drop in the inter-particle forces which lead to a large increase in temperature differences between neighboring pebbles.

As the first step in the modeling effort, there were many simplifications that had to be made in this study. We must note here the shortcomings of the assumptions and simplifications of this study before drawing any major conclusions from the results.

First, the ‘container walls’ surrounding the pebble bed in this model are completely rigid and do not react as the swelling pebble bed presses into them while heating. The confined thermal expansion leads to very high contact forces in the pebble bed that may not be

realistic. The abnormally high contact forces are most likely to be the source of the abnormally high baseline effective thermal conductivity,  $k_0 = 1.03 \text{ W/m-K}$ . In experiments on the effective thermal conductivity of lithium ceramics in vacuum, the beds are often allowed to expand freely while heating (in at least one direction) and in vacuum were measured to be closer to  $k_0 = 0.5 \text{ W/m-K}$  [FIND THE REAL VALUES TO PUT HERE!]. We note, however, that this value has been calculated in the absence of interstitial gas so the results apply only to the reduction in energy transferred via inter-particle conduction.

Second, we saw from Fig.12.2 that the majority of the pebbles in the ensemble have their temperatures close fitting to an average curve but a number of the pebbles had less thermal contact with neighboring particles and consequently had much larger temperatures. This was true even in the baseline case of a tightly packed ( $\phi = 64\%$ ) pebble bed. This phenomena is only possible because the contribution to heat transfer of the interstitial gas was not considered in this model. The flowing helium gas is expected to prevent any runaway temperatures of individual pebbles as it provides another route of energy transfer in the bed. This will be addressed in § 13.

Lastly, the pebble crushing did not conserve mass and did not have predictive whatever.

# CHAPTER 13

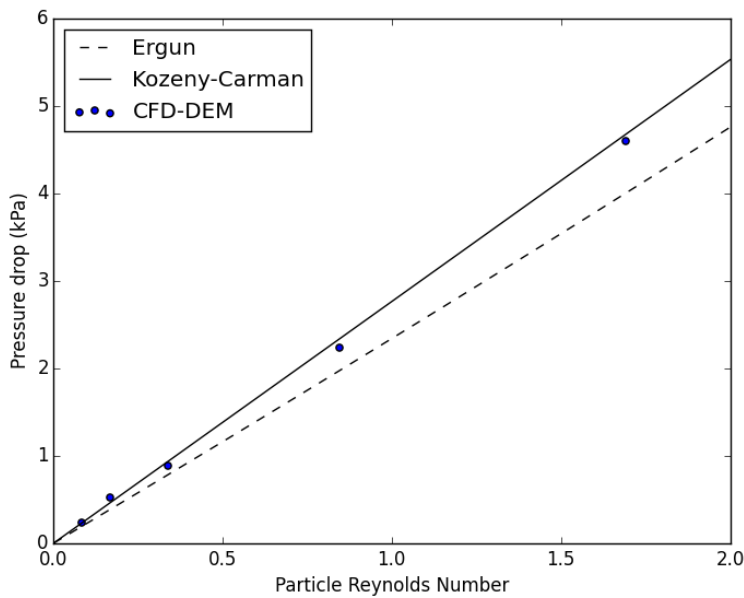
## Coupled CFD-DEM Models Revealing the Influence of Helium Purge Gas on Effective Thermal Conductivity of a Pebble Bed Experiencing Pebble Crushing

The numerical implementation of fluid-solid interaction was outlined in § 8. Although we are most interested in the thermal response of the packed beds to the interstitial gas, we will begin by comparing the results of momentum interaction.

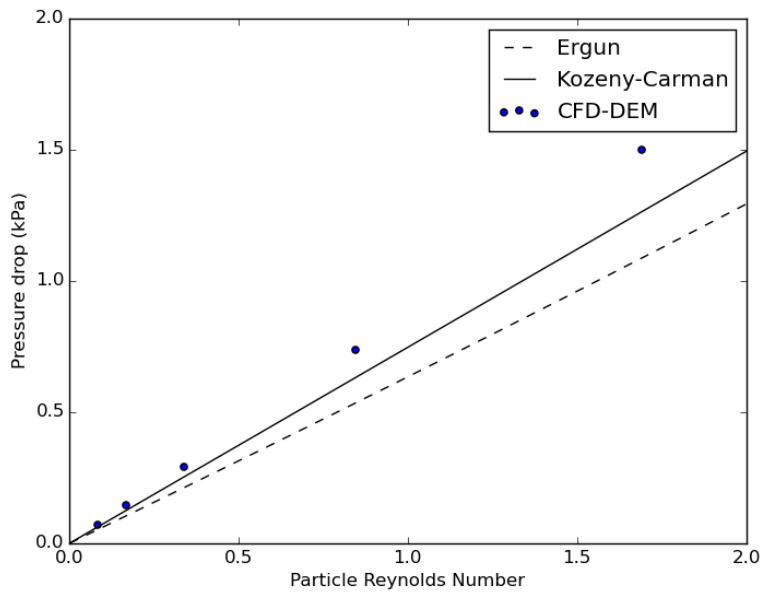
### 13.1 Pressure Drop

Before analyzing thermal results from the CFD-DEM coupling, the system was run at various particle Reynolds numbers and the overall pressure drop of the packed bed was measured. This value was compared against the well-known Kozeny-Carman and Ergun equations. The Kozeny-Carman is known to fit better with experimental data at very small Reynolds numbers. In Fig. 13.1 we see the CFD-DEM coupling model is providing bed-scale pressure drops that match very well with Kozeny-Carman over the Reynold's numbers applicable to helium purge flow in fusion reactors.

The flow is visualized in Fig. 13.2. The pebble bed is clipped at the centerline to allow viewing of the helium streamlines. Apparent in the figure is temperature profiles in the helium from centerline to wall that qualitatively mirror temperature profiles in the pebble bed.



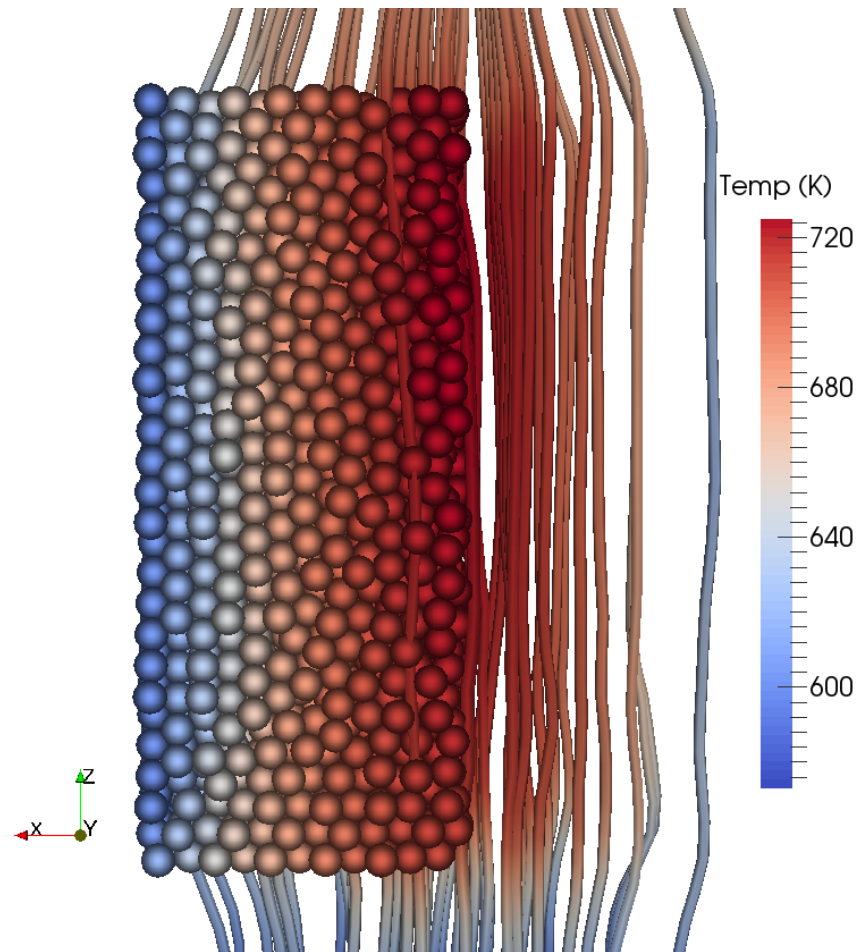
(a) Well-packed bed



(b) Re-settled bed

Figure 13.1: Pressure drop calculations across packed beds, solved by CFD-DEM, fit well to the Kozeny-Carman empirical relation.

Figure 13.2: Cut-away view of the pebble bed with streamlines of helium moving in generally straight paths from inlet to exit.



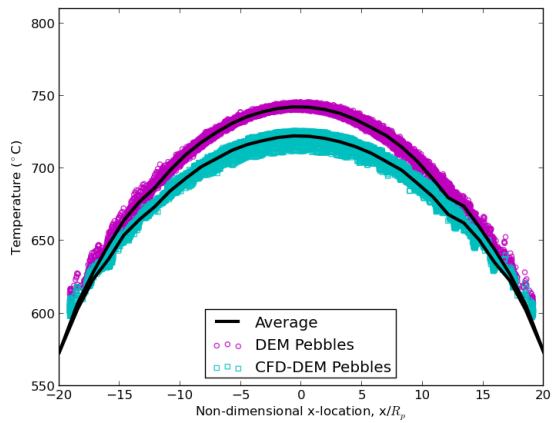
## 13.2 Effective Thermal Conductivity from CFD-DEM

### 13.2.1 Stagnant interstitial fluid

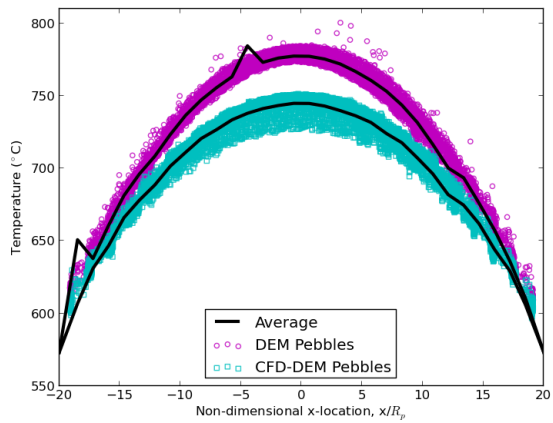
can use correlations for stagnant gas in packed bed.

### 13.2.2 Purge Gas

The well-packed and resettled pebble beds were run to thermal steady-state with nuclear heating and wall cooling in both pure DEM and coupled CFD-DEM simulations for comparison. From steady-state temperature distributions, seen in the pebble scatter plots in



(a) Well-packed bed



(b) Re-settled bed

Figure 13.3: Scatter temperature profiles of pebbles in a bed that is: well-packed (left) and resettled after 10% of pebbles were removed from crushing (right). The introduction of helium into the simulation contributes to both lower overall temperatures (higher effective conductivity) and the smoothing out of high temperatures of isolated pebbles.

Fig. 3, an average profile is calculated and an effective thermal conductivity computed. The values are tabulated in Table I. In the case of pure DEM, energy is transported solely along conduction routes in the ensemble. When the packing of the bed is disturbed, this results in a substantial drop in effective conductivity (a drop of 31%). The details of the conductivity reduction were studied extensively in Ref. 23. Perhaps more important than the reduction in effective conductivity, is the appearance of isolated pebbles. Because heat deposition is volumetrically applied, pebbles with poor conduction routes become much hotter than their neighbors. This is evident in the high temperatures seen in many of the pebbles in the right figure of Fig. 3. Over-heating of isolated pebbles could induce sintering and impact their tritium release even when the average temperatures measured in the bed are well below sintering values. When CFD-DEM beds are analyzed, there is still a large reduction in effective conductivity (22% drop), but interesting to note is the lack of isolated pebbles with high temperatures. In the CFD-DEM scatter plot of the right image in Fig. 3, there is evidence of the reduced heat transfer in the same region as the isolated pebbles from the DEM bed, but the temperatures are much closer to the average values of neighboring pebbles. The helium purge gas has effectively smoothed out the temperatures and provided heat transport paths for any pebbles that have loose physical contact with neighbors. In spite of the 22% decrease in effective conductivity, the maximum temperature of the pebble bed only increased 6.2% (from 725 to 751 K) when helium is included in the model. This result is significant for solid breeder designers. They may choose a solid breeder volume such that in the event of extensive pebble cracking, the maximum temperature of the bed would remain within the ideal windows dictate for the lithium ceramics.

An accompanying result is the increased amount of energy carried out of the system by the helium purge gas. In Table I, the last column provides the ratio of energy carried out of the system to the nuclear energy deposited into the bed. The amount of energy carried out by the helium increased from 1.15% to 1.52% from ‘well-packed’ to ‘resettled’. evap-x-T-color The CFD-DEM formulation maintains calculations of pebble-pebble interactions while dynamically coupling to the helium flow. The model demonstrates the ability of helium gas

Table 13.1: Pebble bed values from the test matrix of the beds analyzed in this study.

	$k_{\text{eff}}$ (W/mK)	$T_{\text{max}}$ (K)	$\frac{Q_h}{Q_{\text{nuc}}}$		
	DEM	CFD-DEM	DEM	CFD-DEM	CFD-DEM
Well-packed	0.96	1.09	745	725	1.15
Resettled	0.66	0.85	800	751	1.52

to smooth out any hot spots predicted by pure-conduction DEM formulations. Further, the lattice-Boltzmann simulation, while not fully coupled to DEM, revealed important features of helium flow in volumetrically heated pebble beds – mainly the smearing of temperature profiles along the paths of cooling.

## **CHAPTER 14**

# **3D Lattice-Boltzmann Models of the Complete Conjugate Heat Transfer of Helium Purge Gas and Ceramic Pebble Beds**

## CHAPTER 15

### Applications to Real Solid Breeder Blanket Designs

In this study we apply coupled computational fluid dynamics and discrete element method (CFD-DEM) modeling tools to study the combined effects of pebble crushing, packing restructuring due to both gravity and the unbalanced force network in the pebble bed, and convection from helium purge gas on subsequent temperature profiles in solid breeders for different breeding configurations. In typical solid breeder modules, coolant fluid runs through the containing structure surrounding the pebble bed. Heat is removed from the pebble bed predominately through inter-particle conduction and contact conductance of many pebbles pressed against the containing surface. As such, heat transfer out of the pebble bed relies on maintaining good pebble-pebble and pebble-wall contact. However, physical contact is interrupted to different degrees when a pebble bed responds to various amounts of individual crushed pebbles. Furthermore, the restructuring of the pebble bed after a pebble crushing event is, in part, dependent on gravity forces acting upon each pebble in the ensemble. We investigate two representative pebble bed configurations where heat is removed from the bed via inter-particle conduction, convection of purge gas, and contact between the pebble bed and its container. In the first, the coolant containing structural walls (heat transfer walls) are oriented parallel to the gravity force. In the second configuration, the heat transfer walls are perpendicular to the direction of gravity. To simulate a crushed pebble, we replace the pebble with many smaller, non-cohesive elements while maintaining mass-conservation between the original solid pebble and crushed fragments. The fragments are then free to resettle into interstitial gaps and the rest of the bed resettles as determined by forces from gravity, contact of neighboring particles, and even the small influence of the moving purge

gas. The thermofluid interaction with the helium purge gas will be included with volume-averaged Navier-Stokes and energy equations. The representative solid breeder volumes will be compared with respect to their temperature peaks and profiles and how those temperatures vary as a function of the percentage of crushed pebbles in the ensemble. The results can be used to optimize solid breeder pebble bed designs through the choice of breeding zone orientation relative to the gravity vector.

**Part V**

## **Future Work**

**Part VI**

# **Appendices**

## APPENDIX A

### Sphere with heat generation

We solve for the temperature distribution inside a single sphere of constant thermal conductivity with constant heat generation with a convective heat transfer boundary condition. To simplify to homogeneous boundary conditions, the temperature we solve for will be in reference to the fluid temperature,  $\mathbb{T} = T - T_f$ .

The energy equation in spherical coordinates with axial symmetry is,

$$\frac{1}{r} \frac{\partial^2}{\partial r^2} (r \mathbb{T}) + \frac{g}{k} = \frac{1}{\alpha} \frac{\partial \mathbb{T}}{\partial t} \quad (\text{A.1})$$

which is subject to the boundary conditions of a constant heat transfer coefficient at the surface,  $h$ ,

$$\left[ \frac{\partial \mathbb{T}}{\partial r} + \frac{h}{k} \mathbb{T} \right]_{r=b} = 0 \quad (\text{A.2})$$

and an axisymmetry at the center,

$$\left[ \frac{\partial \mathbb{T}}{\partial r} \right]_{r=0} = 0 \quad (\text{A.3})$$

The sphere will be at an isothermal initial temperature,

$$\mathbb{T}(r, 0) = \mathbb{T}_0 \quad (\text{A.4})$$

## A.1 Transformations

We first transform the system into the nondimensional forms as defined in § 11.2,

$$\begin{aligned}\theta &= \frac{T}{T_0} \\ \rho &= \frac{r}{b} \\ \tau &= \frac{t}{b^2/\alpha}\end{aligned}$$

The energy equation is then,

$$\frac{1}{\rho} \frac{\partial^2}{\partial \rho^2} (\rho \theta) + G = \frac{\partial \theta}{\partial \tau} \quad (\text{A.5})$$

$$\text{where } G = \frac{gb^2}{kT_0}$$

The next transformation will be to introduce  $U(\rho, \tau) = \rho \theta(\rho, \tau)$  as a transformation variable to simplify the differential equation of energy conservation. In the new variable formulation, the energy equation is,

$$\frac{\partial^2 U}{\partial \rho^2} + G\rho = \frac{\partial U}{\partial \tau} \quad (\text{A.6})$$

The boundary conditions are likewise transformed into,

$$\left[ \frac{\partial U}{\partial \rho} + (\text{Bi} - 1) U \right]_{\rho=1} = 0 \quad (\text{A.7})$$

and

$$U|_{\rho=0} = 0 \quad (\text{A.8})$$

with initial condition

$$U(\rho, 0) = U_0 = \theta_0 r^* = r^* \quad (\text{A.9})$$

## A.2 Solution

Because of the non-homogeneous form of the energy equation (due to the heat generation term), we will solve Eq. A.6 by breaking it up into two simpler problems,

1. A non-homogeneous, steady-state problem defined by  $U_{ss}(r)$
2. A homogeneous, time-dependent problem defined by  $U_h(r, t)$

The steady-state distribution  $U_{ss}$  is found from the solution of

$$\frac{\partial^2 U_{ss}}{\partial \rho^2} + G\rho = 0 \quad (\text{A.10})$$

subject to the same boundary condition given by Eqs. A.7,A.8. Separation and integration gives.

$$U_{ss} = -\frac{G}{6}\rho^3 + C_1\rho + C_2 \quad (\text{A.11})$$

Applying Eq. A.8 directly gives  $C_2 = 0$  and, with some algebra Eq. A.7 gives,

$$C_1 = \left( \frac{G}{6} + \frac{G}{3\text{Bi}} \right)$$

valid for  $\text{Bi} > 0$ . Thus the steady-state distribution of our transformed variable is

$$U_{ss} = \left( \frac{G}{6} + \frac{G}{3\text{Bi}} - \rho^2 \right) \rho \quad (\text{A.12})$$

The next step is to find the homogeneous solution of

$$\frac{\partial^2 U_h}{\partial \rho^2} = \frac{\partial U_h}{\partial \tau} \quad (\text{A.13})$$

Again, subject to Eqs. A.7,A.8, but now with a modified initial condition of

$$\begin{aligned} U_{h,0} &= U_0 - U_{ss} \\ &= \left[ 1 - \left( \frac{G}{6} + \frac{G}{3\text{Bi}} - \rho^2 \right) \right] \rho \end{aligned} \quad (\text{A.14})$$

This is a standard homogeneous partial differential equation. The solution is of the form

$$U_h = R(\rho)\Gamma(\tau) \quad (\text{A.15})$$

The solution for  $\Gamma$  is given as

$$\Gamma = \exp(-\zeta^2\tau) \quad (\text{A.16})$$

The space-variable function  $R(\zeta, \rho)$  satisfies the following eigenvalue problem:

$$\frac{d^2R}{d\rho^2} + \zeta^2 R = 0 \quad (\text{A.17})$$

subject to

$$R_{\rho=0} = 0 \quad (\text{A.18})$$

and

$$\left[ \frac{dR}{d\rho} + (\text{Bi} - 1)R \right]_{\rho=1} = 0 \quad (\text{A.19})$$

This eigenvalue problem is a special case of the Sturm-Liouville problem. The solution for  $U_h$  can be constructed from known eigenvalue solutions,

$$U_h(\rho, \tau) = \sum_{n=1}^{\infty} c_n R(\zeta_n, \rho) \exp(-\zeta_n^2 \tau) \quad (\text{A.20})$$

Application of the initial condition gives,

$$F(\rho) = \sum_{n=1}^{\infty} c_n R(\zeta_n, \rho) \quad (\text{A.21})$$

where  $F(\rho)$  is the initial condition defined from Eq A.9,

$$F(\rho) = \left[ 1 - \frac{G}{6} \left( 1 + \frac{2}{\text{Bi}} - \rho^2 \right) \right] \rho \quad (\text{A.22})$$

The coefficients of  $c_n$  can be determined by applying the operator  $\int_0^1 R(\zeta_n, \rho) d\rho$  and utilizing the orthogonality property of eigenfunctions. The coefficients are found in the form

$$c_n = \frac{1}{N(\zeta_n)} \int_0^1 R(\zeta_n, \rho') F(\rho') d\rho' \quad (\text{A.23})$$

The norm,  $N$  is a function of the eigenvalues,

$$N(\zeta_n) = \int_0^1 [R(\zeta_n, \rho)]^2 d\rho \quad (\text{A.24})$$

The eigenfunctions for Eq. A.17 are

$$R(\zeta_n, \rho) = \sin(\zeta_n \rho) \quad (\text{A.25})$$

where the eigenvalues are the root of the following transcendental equation,

$$\zeta_n \cot(\zeta_n) = -H \quad (\text{A.26})$$

the roots of which will be found numerically. The normalization integral is then solved as

$$\frac{1}{N(\zeta_n)} = 2 \frac{\zeta_n^2 + H^2}{\zeta_n^2 + H^2 + H} \quad (\text{A.27})$$

where  $H = (\text{Bi} - 1)$ .

We substitute the coefficients of Eq. A.23, they can be substituted back into Eq. A.20 and we have a solution for the homogeneous, transient distribution,

$$U_h(\rho, \tau) = \sum_{n=1}^{\infty} \exp(-\zeta_n^2 \tau) \frac{R(\zeta_n, \rho)}{N(\zeta_n)} \int_0^1 R(\zeta_n, \rho') F(\rho') d\rho' \quad (\text{A.28})$$

In order to explicitly express the solution, we will first set the integral equal to a function  $Z(\zeta_n)$  and evaluate as,

$$\begin{aligned} Z(\zeta_n) &= \int_0^1 R(\zeta_n, \rho') F(\rho') d\rho' \\ &= \int_0^1 \sin(\zeta_n \rho') \left[ 1 - \left( \frac{G}{6} + \frac{G}{3\text{Bi}} - \rho'^2 \right) \right] \rho' d\rho' \\ &= \left[ 1 - \left( \frac{G}{6} + \frac{G}{3\text{Bi}} \right) \right] \int_0^1 \sin(\zeta_n \rho') \rho' d\rho' + \frac{G}{6} \int_0^1 \sin(\zeta_n \rho') \rho'^3 d\rho' \end{aligned} \quad (\text{A.29})$$

The two unique integrals are evaluated as

$$\begin{aligned} C_n &= \int_0^1 \sin(\zeta_n \rho') \rho' d\rho' = \frac{\sin \zeta_n - \zeta_n \cos \zeta_n}{\zeta_n^2} \\ K_n &= \int_0^1 \sin(\zeta_n \rho') \rho'^3 d\rho' = \frac{3(\zeta_n^2 - 2) \sin \zeta_n - \zeta_n(\zeta_n^2 - 6) \cos \zeta_n}{\zeta_n^4} \end{aligned}$$

Thus our  $Z$  function is

$$Z(\zeta_n) = \left[ 1 - \left( \frac{G}{6} + \frac{G}{3\text{Bi}} \right) \right] C_n + \frac{G}{6} K_n \quad (\text{A.30})$$

The homogeneous solution is then written in a compact form as,

$$U_h(\rho, \tau) = \sum_{n=1}^{\infty} \exp(-\zeta_n^2 \tau) \sin(\zeta_n \rho) \frac{Z(\zeta_n)}{N(\zeta_n)} \quad (\text{A.31})$$

The complete solution is then a superposition of Eq. A.12 and Eq. A.31,

$$U(\rho, \tau) = \left( \frac{G}{6} + \frac{G}{3\text{Bi}} - \rho^2 \right) \rho + \sum_{n=1}^{\infty} \exp(-\zeta_n^2 \tau) \sin(\zeta_n \rho) \frac{Z(\zeta_n)}{N(\zeta_n)} \quad (\text{A.32})$$

We now transform back to our dimensionless temperature,

$$\theta(\rho, \tau) = \left( \frac{G}{6} + \frac{G}{3\text{Bi}} - \rho^2 \right) + \sum_{n=1}^{\infty} \exp(-\zeta_n^2 \tau) \frac{\sin(\zeta_n \rho)}{\rho} \frac{Z(\zeta_n)}{N(\zeta_n)} \quad (\text{A.33})$$

### A.3 Energy

We will want to compare the solution of Eq. A.33 to that of a sphere with the lumped capacitance assumption. To facilitate comparison, we look to a measure of the energy of the sphere (with radial dependence removed via integration of Eq. A.33). The energy will be nondimensionalized as,

$$E^*(\tau) = \frac{E(\tau)}{E_0} \quad (\text{A.34})$$

where  $E_0$  is the initial energy of the sphere,

$$E_0 = \rho_r C_r V \mathbb{T}_0 \quad (\text{A.35})$$

Thus the nondimensional energy of the sphere at a given time,  $\tau$  is

$$\begin{aligned} E^*(\tau) &= \int \frac{\rho_r C_r \mathbb{T}(\rho, \tau) dV}{\rho_r C_r V \mathbb{T}_0} \\ E^*(\tau) &= \frac{1}{V} \int \theta(\rho, \tau) dV \end{aligned} \quad (\text{A.36})$$

For a circle in spherical coordinates:

$$dV = r^2 \sin(\phi) dr d\phi d\theta \quad (\text{A.37})$$

For our sphere, this becomes:

$$dV = 4\pi b^3 \rho^2 d\rho = 3V \rho^2 d\rho \quad (\text{A.38})$$

The integral for dimensionless energy of our sphere is then,

$$E = 3 \int_0^1 \left[ \frac{G}{6} \left( 1 + \frac{2}{\text{Bi}} - \rho^2 \right) + \sum_{n=1}^{\infty} \exp(-\zeta_n^2 \tau) \frac{\sin(\zeta_n \rho)}{\rho} \frac{Z(\zeta_n)}{N(\zeta_n)} \right] \rho^2 d\rho \quad (\text{A.39})$$

This ultimately reduces to,

$$E^* = \left( \frac{G}{15} + \frac{G}{3\text{Bi}} \right) + 3 \sum_{n=1}^{\infty} \exp(-\zeta_n^2 \tau) \frac{Z(\zeta_n)}{N(\zeta_n)} C_n(\zeta_n) \quad (\text{A.40})$$

## APPENDIX B

### History of solid breeder design

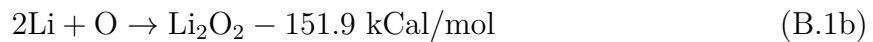
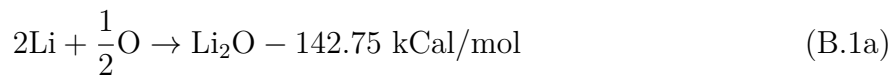
A design was proposed by Abdou *et al.*<sup>2</sup> in 1975 wherein the plasma would be surrounded by a blanket of nonmobile, solid lithium. To exist in solid form at high temperatures, pure lithium, which has a melting temperature of only about 180 °C, must be combined with refractory materials (melting temperatures >1000 °C). To date, most parties researching solid breeder blankets have settled on lithium orthosilicate ( $\text{Li}_4\text{SiO}_4$ ) or lithium metatitanate ( $\text{Li}_2\text{TiO}_3$ ) as candidate ceramics.

As nuclear energy is deposited into the solid breeder, large thermal gradients in the solid lithiated ceramics will induce thermal stresses across large characteristic lengths. Avoiding thermal stress has led to most solid breeder designs implementing packed beds of small, spherical (or near-spherical) pebbles.<sup>22,61,65,87</sup> Moreover, tritium diffusion and release considerations for solid lithium ceramic support the choice of short characteristic lengths of individual pebbles. From an engineering design standpoint, the choice of packed bed has other desirable characteristics. For instance, the ensemble of small spherical pebbles can be filled into many complex shapes with relatively uniform porosity. The uniform packing of spheres permits a well-distributed flow of purge gas for tritium extraction.

The advantages of the pebble bed design include ease of uniformly assembling the solid into complex geometries, ease of tritium extraction from the porous bed via an interstitial purge of helium, and with the small size of pebbles being more resilient to thermal stresses than a solid brick of lithiated ceramic.<sup>16</sup>

Lithium oxide had been considered because of its favorable lithium density, among other attractive features, though the reaction of lithium with elemental oxygen is a concern. Pure

lithium reacts with oxygen exothermically in reactions such as



Of primary concern in lithium fires is the peak flame temperature. This will determine, to a large extent, whether many radioactive species become air-borne by vaporization. The flame temperature depends on many variables. Some investigations found it to be about 2500 K which would cause some materials to melt but not vaporize. [cite Abdou's class notes?]

## REFERENCES

- [1] Mohamed A Abdou. IFE chamber technology testing program in NIF and chamber development test plan. In *16th IEEE/NPSS Symposium on Fusion Engineering*, volume 1, pages 7–11. IEEE, 1995.
- [2] Mohamed A Abdou and CW Maynard. Calculational methods for nuclear heating – part II: Applications to fusion-reactor blankets and shields. *Nuclear Science and Engineering*, 56:381–398, 1975.
- [3] Ali Abou-Sena, Alice Y. Ying, and Mohamed A Abdou. Effective Thermal Conductivity of Lithium Ceramic Pebble Beds for Fusion Blankets: A Review. *Fusion Science and Technology*, 47(4):1094–1100, 2005.
- [4] Zhiyong An, Alice Ying, and Mohamed A Abdou. Numerical characterization of thermo-mechanical performance of breeder pebble beds. *Journal of Nuclear Materials*, 367-370:1393–1397, 2007.
- [5] Ratna Kumar Annabattula, Yixiang Gan, and Marc Kamlah. Mechanics of binary and polydisperse spherical pebble assembly. *Fusion Engineering and Design*, pages 2–7, March 2012.
- [6] Ratna Kumar Annabattula, Yixiang Gan, Shuo Zhao, and Marc Kamlah. Mechanics of a crushable pebble assembly using discrete element method. *Journal of Nuclear Materials*, 430(1-3):90–95, November 2012.
- [7] J Bandrowski and G Kaczmarzyk. Gas-to-particle heat transfer in vertical pneumatic conveying of granular materials. *Chemical Engineering Science*, 33:1303–1310, 1977.
- [8] G.K. Batchelor and R.W. O'Brien. Thermal or Electrical Conduction Through a Granular Material. *Proceedings of the Royal Society of London. Series A, Mathematical and Physical Sciences*, 355(1682):313–333, 1977.
- [9] Sofiane Benyahia, Madhava Syamlal, and Thomas J. O'Brien. Extension of Hill–Koch–Ladd drag correlation over all ranges of Reynolds number and solids volume fraction. *Powder Technology*, 162(2):166–174, March 2006.
- [10] Nv Brilliantov, F Spahn, Jm Hertzsch, and T Pöschel. Model for collisions in granular gases. *Physical review. E, Statistical physics, plasmas, fluids, and related interdisciplinary topics*, 53(5):5382–5392, May 1996.
- [11] Chang-sheng Bu, Dao-yin Liu, Xiao-ping Chen, Cai Liang, Yu-feng Duan, and Lun-bo Duan. Modeling and Coupling Particle Scale Heat Transfer with DEM through Heat Transfer Mechanisms. *Numerical Heat Transfer, Part A: Applications*, 64(1):56–71, July 2013.

- [12] L. Bühler and Jörg Reimann. Thermal creep of granular breeder materials in fusion blankets. *Journal of Nuclear Materials*, 307-311:807–810, December 2002.
- [13] P. Calderoni, Alice Ying, Tomas Sketchley, and Mohamed A Abdou. Experimental study of the interaction of ceramic breeder pebble beds with structural materials under thermo-mechanical loads. *Fusion Engineering and Design*, 81(1-7):607–612, 2006.
- [14] P.C. Carman. Fluid flow through granular beds, 1937.
- [15] P.C. Carman. *Flow of Gas Through Porous Media*. London Butterworths Scientific Publications, 1956.
- [16] S. Casadio. Ceramic Breeder Technology. *International School of Fusion Tokamak Reactors*, 2004.
- [17] Bodhisattwa Chaudhuri, Fernando J. Muzzio, and M. Silvina Tomassone. Modeling of heat transfer in granular flow in rotating vessels. *Chemical Engineering Science*, 61(19):6348–6360, October 2006.
- [18] Francis Chen. *An Indispensable Truth How Fusion Power Can Save the Planet*. Springer, 2011.
- [19] K Chen, A. Harris, J. Draskovic, and P. Schiffer. Granular fragility under thermal cycles. *Granular Matter*, 11(4):237–242, May 2009.
- [20] G.J. Cheng, A.B. Yu, and P. Zulli. Evaluation of effective thermal conductivity from the structure of a packed bed. *Chemical Engineering Science*, 54(4199):4209, 1999.
- [21] Seungyon Cho, Mu-Young Ahn, Duck Hoi Kim, Eun Seok Lee, Sunghwan Yun, Nam Zin Cho, and Ki Jung Jung. Current status of design and analysis of Korean Helium-Cooled Solid Breeder Test Blanket Module. *Fusion Engineering and Design*, 83(7-9):1163–1168, December 2008.
- [22] Seungyon Cho, Mu-Young Ahn, In-Keun Yu, Yi-Hyun Park, Duck Young Ku, Sang-Jin Lee, Han-Ki Yoon, and Tae-Gyu Kim. R&D progress of Korean HCSB TBM. *Fusion Engineering and Design*, 87(5-6):386–391, August 2012.
- [23] Peter A Cundall and Otto D L Strack. A discrete numerical model for granular assemblies. *Geotechnique*, 29(1):47–65, 1979.
- [24] G. Dell’Orco, Francesco Paolo Di Maio, R. Giannusso, A. Malavasi, L. Sansone, A. Tincani, and G. Vella. Progress in the benchmark exercise for analyzing the lithium-breeder pebble bed thermo-mechanical behaviour. *Fusion Engineering and Design*, 81(1-7):169–174, February 2006.
- [25] G. Dell’Orco, Francesco Paolo Di Maio, R. Giannusso, A. Tincani, and G. Vella. On the theoretical-numerical study of the HEXCALIBER mock-up thermo-mechanical behaviour. *Fusion Engineering and Design*, 85(5):694–706, August 2010.

- [26] G. Dell'Orco, P Dimaio, R. Giammusso, A. Tincani, G. Vella, and Francesco Paolo Di Maio. A constitutive model for the thermo-mechanical behaviour of fusion-relevant pebble beds and its application to the simulation of HELICA mock-up experimental results. *Fusion Engineering and Design*, 82(15-24):2366–2374, October 2007.
- [27] Francesco Paolo Di Maio, G. Dell'Orco, R. Giammusso, A Malavasi, I. Ricapito, A. Tin-canai, and G. Vella. Experimental tests and thermo-mechanical analyses on the HEX-CALIBER mock-up. *Fusion Engineering and Design*, 83(7-9):1287–1293, December 2008.
- [28] Francesco Paolo Di Maio, R. Giammusso, and G. Vella. On the hyperporous non-linear elasticity model for fusion-relevant pebble beds. *Fusion Engineering and Design*, 85(7-9):1234–1244, 2010.
- [29] Alberto Di Renzo and Francesco Paolo Di Maio. Comparison of contact-force models for the simulation of collisions in DEM-based granular flow codes. *Chemical Engineering Science*, 59(3):525–541, February 2004.
- [30] Thibaut Divoux, Hervé Gayvallet, and Jean-Christophe Géminard. Creep Motion of a Granular Pile Induced by Thermal Cycling. *Physical Review Letters*, 101(14):148303, October 2008.
- [31] Mikio Enoeda, Y. Kosaku, Toshihisa Hatano, T. Kuroda, N. Miki, T. Honma, Masato Akiba, S. Konishi, H. Nakamura, Y. Kawamura, S. Sato, K. Furuya, Y. Asaoka, and Kunihiko Okano. Design and technology development of solid breeder blanket cooled by supercritical water in Japan. *Nuclear Fusion*, 43:1837–1844, 2003.
- [32] Sabri Ergun. Fluid flow through packed columns. *Chemical engineering progress*, 48, 1952.
- [33] G. Federici, A René Raffray, and Mohamed A Abdou. MISTRAL: A comprehensive model for tritium transport in lithium-based ceramics. Part II: Comparison of model predictions with experimental results. *Journal of Nuclear Materials*, 173:185–213, 1990.
- [34] Y.T. Feng and K. Han. An accurate evaluation of geometric view factors for modelling radiative heat transfer in randomly packed beds of equally sized spheres. *International Journal of Heat and Mass Transfer*, 55(23-24):6374–6383, November 2012.
- [35] J H Fokkens. Thermo-mechanical Finite Element Analyses for the HCPB In-pile Test Element, 2003.
- [36] Yixiang Gan. Thermal Discrete Element Analysis of EU Solid Breeder Blanket Subjected to Neutron Irradiation. *Fusion Science & Technology*, 66, 2014.
- [37] Yixiang Gan and Marc Kamlah. Identification of material parameters of a thermo-mechanical model for pebble beds in fusion blankets. *Fusion Engineering and Design*, 82(2):189–206, February 2007.

- [38] Yixiang Gan and Marc Kamlah. Thermo-mechanical analysis of pebble beds in HELICA mock-up experiments. *Fusion Engineering and Design*, 83(7-9):1313–1316, December 2008.
- [39] Yixiang Gan and Marc Kamlah. Thermo-mechanical analyses of HELICA and HEX-CALIBER mock-ups. *Journal of Nuclear Materials*, 386-388:1060–1064, April 2009.
- [40] Yixiang Gan and Marc Kamlah. Discrete element modelling of pebble beds: With application to uniaxial compression tests of ceramic breeder pebble beds. *Journal of the Mechanics and Physics of Solids*, 58(2):129–144, February 2010.
- [41] Yixiang Gan and Marc Kamlah. Thermo-mechanical modelling of pebble bed-wall interfaces. *Fusion Engineering and Design*, 85(1):24–32, January 2010.
- [42] Yixiang Gan, Marc Kamlah, Heinz Riesch-Oppermann, Rolf Rolli, and Ping Liu. Crush probability analysis of ceramic breeder pebble beds under mechanical stresses. *Journal of Nuclear Materials*, pages 10–13, December 2010.
- [43] Paul J Gierszewski. Review of properties of lithium metatitanate. *Fusion Engineering and Design*, 39-40:739–743, September 1998.
- [44] F. a. Gilabert, J. N. Roux, and a. Castellanos. Computer simulation of model cohesive powders: Influence of assembling procedure and contact laws on low consolidation states. *Physical Review E - Statistical, Nonlinear, and Soft Matter Physics*, 75:1–26, 2007.
- [45] Klemens Gruber. *Sediment transport in open channel flows - Experimental investigation and numerical simulation of local scour development downstream of a weir*. PhD thesis, 2012.
- [46] H. Grubmuller, H. Heller, A Windemuth, and K. Schulten. Generalized verlet algorithm for efficient molecular dynamics simulations with long-range interaction. *Molecular Simulation*, 6:121–142, 1991.
- [47] F. Hernández, M. Kolb, Ratna Kumar Annabattula, and a. V.d. Weth. Construction of PREMUX and preliminary experimental results, as preparation for the HCPB breeder unit mock-up testing. *Fusion Engineering and Design*, 89(7-8):1257–1262, 2014.
- [48] Reghan J. Hill, Donald L. Koch, and Anthony J. C. Ladd. Moderate-Reynolds-number flows in ordered and random arrays of spheres. *Journal of Fluid Mechanics*, 448:243–278, November 2001.
- [49] Reghan J. Hill, Donald L. Koch, and Anthony J. C. Ladd. The first effects of fluid inertia on flows in ordered and random arrays of spheres. *Journal of Fluid Mechanics*, 448:213–241, November 2001.

- [50] C.P. Jeffreson. Prediction of Breakthrough Curves in Packed Beds: 1. Applicability of Single Parameter Models. *American Institute of Chemical Engineers*, 18(2):409–416, March 1972.
- [51] KL Johnson. *Contact Mechanics*. 1985.
- [52] Christoph Kloss and Christoph Goniva. LIGGGHTS - Open Source Discrete Element Simulations of Granular Materials Based on LAMMPS. *Supplemental Proceedings: Materials Fabrication, Properties, Characterization, and Modeling*, 2:781–788, 2011.
- [53] Christoph Kloss, Christoph Goniva, Alice Hager, Stefan Amberger, and Stefan Pirker. Models, algorithms and validation for opensource DEM and CFD-DEM. *Progress in Computational Fluid Dynamics*, 12(2/3):140–152, 2012.
- [54] Donald L Koch and Reghan J. Hill. Inertial Effects in Suspension and Porous-Media Flows. *Annual Review of Fluid Mechanics*, 33(1):619–647, January 2001.
- [55] H. Kruggel-Emden, M. Sturm, S. Wirtz, and V. Scherer. Selection of an appropriate time integration scheme for the discrete element method (DEM). *Computers & Chemical Engineering*, 32(10):2263–2279, October 2008.
- [56] C Y Kwok and M D Bolton. DEM simulations of soil creep due to particle crushing. *Géotechnique*, (16):1–12, 2013.
- [57] P A Langston, U Tlرزون, and D M Heyes. Discrete element simulation of granular flow in 2D and 3D hoppers: dependence of discharge rate and wall stress on particle interactions. *Chemical Engineering Science*, 50(6):967–987, 1995.
- [58] Jintang Li and D.J. Mason. A computational investigation of transient heat transfer in pneumatic transport of granular particles. *Powder Technology*, 112(3):273–282, October 2000.
- [59] Zi Lu. *Numerical Modeling and Experimental Measurement of the Thermal and Mechanical Properties of Packed Beds*. PhD thesis, University of California Los Angeles, 2000.
- [60] Zi Lu, Alice Y Ying, and Mohamed A Abdou. Numerical and experimental prediction of the thermomechanical performance of pebble beds for solid breeder blanket. *Fusion Engineering and Design*, 49-50:605–611, 2000.
- [61] J D Lulewicz and N. Roux. Fabrication of Li<sub>2</sub>TiO<sub>3</sub> pebbles by the extrusion–spherisation–sintering process. 311:803–806, 2002.
- [62] A.J. Magielsen, M M W Peeters, J.B.J. Hegeman, M.P. Stijkel, and Jaap G van der Laan. Analysis of the in-pile operation and preliminary results of the post-irradiation dismantling of the pebble bed assemblies, presented at the 8th ISFNT, 2007.

- [63] Hernán Makse, Nicolas Gland, David Johnson, and Lawrence Schwartz. Granular packings: Nonlinear elasticity, sound propagation, and collective relaxation dynamics. *Physical Review E*, 70(6):061302, December 2004.
- [64] Hernán Makse, David Johnson, and Lm Schwartz. Packing of compressible granular materials. *Physical review letters*, 84(18):4160–3, May 2000.
- [65] D. Mandal, D. Sathiyamoorthy, and V. Govardhana Rao. Preparation and characterization of lithium–titanate pebbles by solid-state reaction extrusion and spherodization techniques for fusion reactor. *Fusion Engineering and Design*, 87(1):7–12, January 2012.
- [66] G Marketos and M Bolton. Quantifying the extent of crushing in granular materials: A probability-based predictive method. *Journal of the Mechanics and Physics of Solids*, 55(10):2142–2156, October 2007.
- [67] A F L Nakata, M Hyde, H Hyodo, Others, and G. R. McDowell. A probabilistic approach to sand particle crushing in the triaxial test. *Geotechnique*, 49(5):567–583, 1999.
- [68] Gregory F. Nellis and Sanford a. Klein. *Heat Transfer*. 2009.
- [69] G Piazza, Jörg Reimann, E Günther, Regina Knitter, N. Roux, and J D Lulewicz. Characterisation of ceramic breeder materials for the helium cooled pebble bed blanket. *Journal of Nuclear Materials*, 307-311(0):811–816, December 2002.
- [70] Ramanan Pitchumani, Olesya Zhupanska, Gabriel M.H Meesters, and Brian Scarlett. Measurement and characterization of particle strength using a new robotic compression tester. *Powder Technology*, 143-144:56–64, June 2004.
- [71] Steve Plimpton. Fast Parallel Algorithms for Short-Range Molecular Dynamics. *Journal of Computational Physics*, 117(1):1–19, March 1995.
- [72] Y Poitevin, Lorenzo Boccaccini, M. Zmitko, I Ricapito, J.F. Salavy, E. Diegele, F. Gabriel, E. Magnani, H. Neuberger, R. Lässer, and L. Guerrini. Tritium breeder blankets design and technologies in Europe: Development status of ITER Test Blanket Modules, test & qualification strategy and roadmap towards DEMO. *Fusion Engineering and Design*, 85(10-12):2340–2347, December 2010.
- [73] J. W. S. Rayleigh. On waves propagated along the plane surface of an elastic solid. *Proceedings of the London Mathematical Society*, 17:4–11, 1885.
- [74] Jörg Reimann, E. Arbogast, M. Behnke, S. Müller, and K. Thomaske. Thermomechanical behaviour of ceramic breeder and beryllium pebble beds. *Fusion Engineering and Design*, 49-50:643–649, 2000.

- [75] Jörg Reimann, Lorenzo Boccaccini, Mikio Enoeda, and Alice Ying. Thermomechanics of solid breeder and Be pebble bed materials. *Fusion Engineering and Design*, 61-62:319–331, November 2002.
- [76] Jörg Reimann, D. Ericher, and G. Wörner. Influence of pebble bed dimensions and filling factor on mechanical pebble bed properties. *Fusion Engineering and Design*, 69(1-4):241–244, 2003.
- [77] Jörg Reimann and H Harsch. Thermal creep of beryllium pebble beds. *Fusion Engineering and Design*, 75-79:1043–1047, November 2005.
- [78] Jörg Reimann and S Hermsmeyer. Thermal conductivity of compressed ceramic breeder pebble beds. *Fusion Engineering and Design*, 61-62:345–351, November 2002.
- [79] Jörg Reimann and G. Wörner. Thermal creep of Li<sub>4</sub>SiO<sub>4</sub> pebble beds. *Fusion Engineering and Design*, 58-59:647–651, November 2001.
- [80] Adrian R. Russell, David Muir Wood, and Mamoru Kikumoto. Crushing of particles in idealised granular assemblies. *Journal of the Mechanics and Physics of Solids*, 57(8):1293–1313, August 2009.
- [81] J. Shafer, S Dippel, and D. E. Wolf. Force Schemes in Simulations of Granular Materials. *Journal de Physique I*, 6(1):5–20, January 1996.
- [82] Y. Sheng, C.J. Lawrence, B.J. Briscoe, and C. Thornton. Numerical studies of uniaxial powder compaction process by 3D DEM. *Engineering Computations*, 21(2/3/4):304–317, 2004.
- [83] Leonardo Silbert, Deniz Ertaş, Gary Grest, Thomas Halsey, and Dov Levine. Geometry of frictionless and frictional sphere packings. *Physical Review E*, 65(3):031304, February 2002.
- [84] Leonardo E. Silbert, Deniz Ertaş, Gary Grest, Thomas Halsey, Dov Levine, and Steven Plimpton. Granular flow down an inclined plane: Bagnold scaling and rheology. *Physical Review E*, 64(5):051302, October 2001.
- [85] Hisashi Tanigawa, Mikio Enoeda, and Masato Akiba. Measurement of thermal expansion of Li<sub>2</sub>TiO<sub>3</sub> pebble beds. *Fusion Engineering and Design*, 82(15-24):2259–2263, October 2007.
- [86] Hisashi Tanigawa, Yuichiro Tanaka, and Mikio Enoeda. Packing behaviour of a Li<sub>2</sub>TiO<sub>3</sub> pebble bed under cyclic loads. *Journal of Nuclear Materials*, 417(1-3):2010–2012, December 2010.
- [87] Kunihiko Tsuchiya, Hiroshi Kawamura, Katsuhiro Fuchinoue, Hiroshi Sawada, and Kazutoshi Watarumi. Fabrication development and preliminary characterization of Li<sub>2</sub>TiO<sub>3</sub> pebbles by wet process. *Journal of Nuclear Materials*, 258-263:1985–1990, October 1998.

- [88] Y. Tsuji, T. Kawaguchi, and T. Tanaka. Discrete particle simulation of two-dimensional fluidized bed. *Powder Technology*, 77(1):79–87, October 1993.
- [89] Y. Tsuji, T. Tanaka, and T. Ishida. Lagrangian numerical simulation of plug flow of cohesionless particles in a horizontal pipe. *Powder Technology*, 71(3):239–250, September 1992.
- [90] M. M. Valmiki, Wafaa Karaki, Peiwen Li, Jon T. Van Lew, Cholik Chan, and Jake Stephens. Experimental Investigation of Thermal Storage Processes in a Thermocline Tank. *Journal of Solar Energy Engineering*, 134(4):041003, 2012.
- [91] Jaap G van der Laan, Alexander Fedorov, Sander van Til, and Jörg Reimann. Ceramic Breeder Materials. Technical report, 2011.
- [92] Jon T. Van Lew, Peiwen Li, Cholik Chan, Wafaa Karaki, and Jake Stephens. Analysis of Heat Storage and Delivery of a Thermocline Tank Having Solid Filler Material. *Journal of Solar Energy Engineering*, 133(2):021003, 2011.
- [93] Jon T. Van Lew, Alice Ying, and Mohamed A Abdou. A discrete element method study on the evolution of thermomechanics of a pebble bed experiencing pebble failure. *Fusion Engineering and Design*, 89(7-8):1151–1157, October 2014.
- [94] Jon Thomas Van Lew. *Transient Heat Delivery, Storage Process, and Optimization of a Packed Bed Thermocline Thermal Energy Storage System*. Master’s thesis, University of Arizona, 2010.
- [95] Watson L Vargas and J J McCarthy. Heat Conduction in Granular Materials. *AICHE Journal*, 47(5), 2001.
- [96] Watson L Vargas and J J McCarthy. Conductivity of granular media with stagnant interstitial fluids via thermal particle dynamics simulation. *International Journal of Heat and Mass Transfer*, 45(24):4847–4856, November 2002.
- [97] Watson L Vargas and J J McCarthy. Thermal expansion effects and heat conduction in granular materials. *Physical Review E*, 76(4):1–8, October 2007.
- [98] Jin Tao Wu, Yu Qiang Dai, Ze Wu Wang, and Feng Xia Liu. Study on the Heat Transfer in Granular Materials by DEM. *Advanced Materials Research*, 233-235:2949–2954, May 2011.
- [99] S.Z Wu, K.T. Chau, and T.X. Yu. Crushing and fragmentation of brittle spheres under double impact test. *Powder Technology*, 143-144:41–55, June 2004.
- [100] Ben Xu, Peiwen Li, and Cho Lik Chan. Extending the validity of lumped capacitance method for large Biot number in thermal storage application. *Solar Energy*, 86(6):1709–1724, June 2012.

- [101] Alice Ying, Jörg Reimann, Lorenzo Boccaccini, Mikio Enoeda, Marc Kamlah, Regina Knitter, Yixiang Gan, Jaap G van der Laan, Lida Magielsen, Francesco Paolo Di Maio, G. Dell'Orco, Ratna Kumar Annabattula, Jon T. Van Lew, Hisashi Tanigawa, and Sander van Til. Status of ceramic breeder pebble bed thermo-mechanics R&D and impact on breeder material mechanical strength. *Fusion Engineering and Design*, 87(7-8):1130–1137, August 2012.
- [102] Alice Y. Ying, Hulin Huang, and Mohamed A Abdou. Numerical simulation of ceramic breeder pebble bed thermal creep behavior. *Journal of Nuclear Materials*, 307-311:827–831, December 2002.
- [103] H. Zhang and Hernán Makse. Jamming transition in emulsions and granular materials. *Physical Review E*, 72(1):011301, July 2005.
- [104] H.W. Zhang, Q. Zhou, H.L. Xing, and H. Muhlhaus. A DEM study on the effective thermal conductivity of granular assemblies. *Powder Technology*, 205(1-3):172–183, January 2011.
- [105] Shuo Zhao. *Multiscale Modeling of Thermomechanical Properties of Ceramic Pebbles*. PhD thesis, Karlsruhe Institute of Technology, 2010.
- [106] Shuo Zhao, Yixiang Gan, and Marc Kamlah. Spherical ceramic pebbles subjected to multiple non-concentrated surface loads. *International Journal of Solids and Structures*, 49(3-4):658–671, February 2012.
- [107] Shuo Zhao, Yixiang Gan, and Marc Kamlah. Failure initiation and propagation of Li<sub>4</sub>SiO<sub>4</sub> pebbles in fusion blankets. *Fusion Engineering and Design*, 88(1):8–16, January 2013.
- [108] Shuo Zhao, Yixiang Gan, Marc Kamlah, Tobias Kennerknecht, and Rolf Rolli. Influence of plate material on the contact strength of Li<sub>4</sub>SiO<sub>4</sub> pebbles in crush tests and evaluation of the contact strength in pebble–pebble contact. *Engineering Fracture Mechanics*, 100:28–37, March 2013.
- [109] Z.Y. Zhou, A.B. Yu, and P. Zulli. Particle scale study of heat transfer in packed and bubbling fluidized beds. *AIChe Journal*, 55(4):868–884, April 2009.
- [110] H.P. Zhu, Z.Y. Zhou, R.Y. Yang, and A.B. Yu. Discrete particle simulation of particulate systems: Theoretical developments. *Chemical Engineering Science*, 62(13):3378–3396, July 2007.
- [111] H.P. Zhu, Z.Y. Zhou, R.Y. Yang, and A.B. Yu. Discrete particle simulation of particulate systems: A review of major applications and findings. *Chemical Engineering Science*, 63(23):5728–5770, December 2008.